Beyond distance measurements

Advancing Pulsed X-Band Electron-Electron Double Resonance Spectroscopy

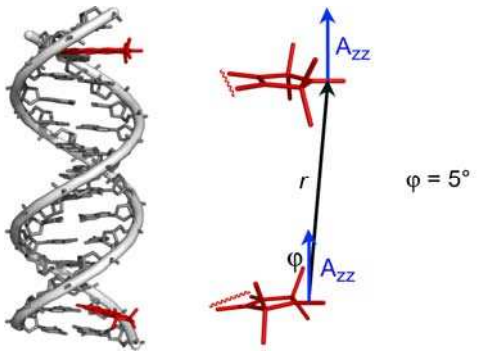

Dissertation

zur Erlangung des Doktorgrades der Naturwissenschaften

vorgelegt dem Fachbereich 14

der Johann Wolfgang Goethe-Universität

in Frankfurt am Main

von

Klaus Dominik Margraf

aus Melle

Frankfurt am Main 2009

D30

In memoriam

Marieta Baumann

Vom Fachbereich Biochemie, Chemie und Pharmazie der Johann Wofgang Goethe-Universität als Dissertation angenommen.

Dekan:	Prof. Dr. Dieter Steinhilber
Gutachter:	Prof. Dr. Thomas F. Prisner
	Prof. Dr. Michael Göbel

Datum der Disputation:

Abstract

Pulsed Electron-Electron Double Resonance (PELDOR) Spectroscopy has been widely applied utilizing stable nitroxide radicals in order to determine distances between unpaired electron spins. Here, the advancement of X-band PELDOR spectroscopy on rigid nitroxide radicals beyond distance measurements towards unraveling an utmost of relevant information encoded in the experimental PELDOR data is described. Therefore, the acquired PELDOR time domain signals are simulated with a home written program (PESIM).

In an interdisciplinary attempt between physical and organic chemistry, suitable polyradicals were synthesized and fully characterized to be employed as PELDOR / PESIM benchmark systems in proof of principle studies leading to the extraction of conformational flexibility of the studied compounds as well as to the relative orientations of spin labels with respect to each other. The latter was applied to short double helical Deoxyribonucleic acids (DNAs). In addition the analysis of PELDOR data in presence of an exchange coupling, which is commonly assumed to be zero, is presented. Furthermore, the method of PELDOR "Spin Counting" allowing to count the number of constituting spin labeled monomers in oligomers was experimentally verified based on novel model systems.

Outline

Firstly, this thesis gives details on the preparation and full characterization of two biradicals, a symmetric and an asymmetric triradical, and a tetraradical via a convergent reaction scheme taking advantage of palladium-catalyzed Sonogashira cross-coupling reactions and an according protection group scheme. Here, 3-ethynyl-1-oxyl-2,2,5,5-tetramethylpyrroline, a spin label for RNA or DNA was employed as the spin bearing group and a protective group strategy for acetylene units and cleavage conditions not interfering with the nitroxyl functionality. All gained nitroxides are chemically stable with well defined distances between the spin centers and mimic different geometries and aggregation states of biomolecules. Also, two new crystal structures were obtained in the course of synthesis.

Secondly, out of this set of polyradicals two biradicals were chosen and X-band PELDOR time traces were acquired with a fixed pump frequency set at the center of the nitroxide spectra, while the detection frequency was systematically varied leading to so called orientation selective measurements. Thereby, the shape of the PELDOR traces of the investigated rigid biradicals changes due to the selection of different orientations of nitroxide radicals with respect to the external magnetic field. Quantitative simulations of the PELDOR data using PESIM could be achieved on the base of a simple geometric model: a free rotation of the nitroxide radical around its acetylene bond and a single bending mode of the interconnecting molecular bridge. The obtained results prove that the distribution functions for the relative orientations of the studied nitroxides differ from a random distribution and thus have to be taken explicitly into account. Otherwise, wrong distance distributions could be deduced from the experiment. Contrariwise, a PESIM simulation of PELDOR time traces with variable offset frequencies allowed determining the conformational freedom of such molecules.

Thirdly, instead of creating a conformational ensemble of biradicals and comparing their calculated PELDOR time traces with the respective experiments this thesis provides an alternative how to disentangle the distance and orientation function directly from the experimental data. The distance distribution function is estimated by means of Tikhonov regularization, using the average over all PELDOR time traces with different frequency offsets and neglecting angular correlations of the spin labels and thereafter Tikhonov regularization is employed again to determine the orientation intensity function. This numerical approach was also benchmarked on the aforementioned nitroxide biradicals. The ansatz works well and is internally consistent. Furthermore, the agreement between independent Molecular Dynamics (MD) simulations, calculated and experimental results are in excellent overall agreement.

Fourthly, after having proven the accuracy of PESIM on model systems, orientation selective PELDOR measurements were performed on two double helical DNAs. The relative orientation of the spin labels with respect to each other described by the angle between the *z*-component of the ^{14}N-hyperfine coupling tensor and the distance vector was gained with high precision.

Fifthly, PELDOR data were analyzed via PESIM assuming isotropic exchange coupling and thus enabling separation of exchange from dipolar coupling and determination of its magnitude, distribution and sign. For two model compounds obtained from collaborators small exchange couplings were extracted. Also, the value of the exchange coupling is in an order which is hard to access with other experimental methods such as Supraconducting Quantum Interference.

Lastly, the entire set of model compounds synthesized by the author was used to calibrate the PELDOR "Spin Counting" methodology for the first time. Not only distances, but also the number of spins in a molecule are accessible by PELDOR spectroscopy due to difference in modulation depth. Hence, the number of constituting monomers in oligomers can be counted.

In conclusion, X-band PELDOR spectroscopy has been successfully advanced beyond its original purpose of determining spatial distances.

Table of Contents

1. Introduction

1.1 Foreword

The central paradigm for the mechanistic understanding of biomolecular function is the idea that the structure and dynamics of a biomolecule determine its function. Of the methods capable to reveal structural data, X-ray crystallography has procured detailed information of large biomacromolecular complexes at atomic resolution.[1,2,3] However, it is not always possible to crystallize such large systems and the non-native structure in the crystal may not represent the functional state in solution.[4] Moreover, flexible structures will decrease the experimentally accessible resolution. Another approach, high-resolution liquid-state Nuclear Magnetic Resonance spectroscopy (NMR) can be applied in solution and yields information about dynamics,[5,6,7] but is currently restricted to systems below ~ 50 kDa. Solid state NMR spectroscopy (ssNMR) has advanced rapidly and is being used to study the structure and dynamics of a variety of solid systems ranging from catalysts and glasses to polymers and proteins. [8]

In order to investigate e.g. folding or conformational changes induced by ligand binding of large biomolecules in solution, other biophysical spectroscopic methods are essential. Especially, fluorescence resonance energy transfer[9] (FRET) and several pulsed Electron Paramagnetic Resonance (EPR) based experiments[10,11,12] e.g. relaxation measurements such as Relaxation Induced Dipolar Modulation Enhancement[13,14], or Double Quantum Coherence (DQC)[15,16,17] give rise to collecting large distances in the nanometer range excluding NMR size limitations.

In general, such long-range distance constraints may be utilized to monitor global structural (re)arrangements. Combined with molecular dynamics (MD) simulations this approach has proven to be extremely valuable.[18]

It is worthwhile to note that in contrast to EPR distance measurements in frozen solution, FRET experiments can be performed in liquids at low sample concentration and even at a single molecule level. Yet, both methods require attachment of either a fluorescent or paramagnetic label, respectively, to the molecule under study. Lately, even a so-called “fluorophore in disguise” has been reported allowing easy conversion of a spin label to a chromophore via a simple chemical reduction of the spin bearing

moiety.[19] The invention of site directed spin labeling[20,21] (SDSL) in EPR spectroscopy further facilitated circumvention of problems arising from incomplete labeling hampering early continuous wave (cw) experiments[22] on biomolecules and the analysis of distance relevant EPR data does not require knowledge regarding fluorescence quenching mechanisms or orientation potentials. Generally, EPR distance measurements were greatly advanced through technical development of spectrometers operating at high fields/high frequencies[23,24] and the methodological development of pulse sequences suitable for biological applications.[25,26] In particular, Pulsed Electron-Electron Double Resonance[27] (PELDOR, sometimes abbreviated as DEER, Double Electron-Electron Resonance) in conjunction with SDSL can access distances of up to 6 nm or, in favorable cases up to 8 nm[28,29] taking advantage of the distance dependent dipolar coupling between the spin centers. Several review articles and books[12,14,30,31,32,33,34] provide examples of numerous applications e.g. between nitroxide spin labels[35,36] or native spin centers in biomolecules[37,38,39,40] and ranging from biological to polymer science. The method is similar to spin-spin distance measurements in ssNMR e.g. Rotational Echo Double Resonance (REDOR)[41], however, due to the higher magnetic moment of electron spins as compared to nuclear spin a larger distance range is accessible. Detailed comparisons to other methods are found in the above cited overview articles.

Only taking into account extraction of distance information, the inventors of the PELDOR methodology promote: "*Undoubtedly, the PELDOR technique is the simplest method of applied research […]"* also regarding *"[…] the analysis of results obtained. Researchers face difficulties only in practical implementation […]. The theory of the phenomenon and experimental design have been elaborated quite well and the necessary equipment is now commercially available*".[31] Yet, the quantitative interpretation of PELDOR data beyond distance measurements such as:

a) angular information,
b) conformational flexibility,
c) determination of the number of spin bearing units or
d) disentangling dipolar and exchange coupling

are much more demanding and will be presented in this thesis in order to gain in depth knowledge of biomolecules.

In case of strong angular correlations between to spin centers[42], such as two tyrosyl radicals in a ribonucleotide reductase dimer, a strong orientation dependence of the experimentally observed dipolar oscillation frequency permits to additionally obtain the relative orientation of the tyrosyl radicals with respect to the distance vector.[43] It should be pointed out that these measurements were performed with a home built spectrometer operating at G-band frequency (180 GHz / 6.5 T). Such orientation selection and angular correlation effects have already been observed in nitroxide biradicals with polyphenyleneethynylene linkers at X-band (9 GHz / 0.3 T), S-band (3 GHz / 0.1 T) and W-band (95 GHz / 3.4 T) frequencies.[28,44,45] However, a quantitative interpretation towards extraction of the conformational flexibility of the studied polyradicals based on a simple geometric model without prior MD studies and utilizing orientation selection was still missing.

Milov, Tsvetkov et al. proposed in 1984 that PELDOR can not only access spin-spin distances, but also count the number of coupled spins from the modulation depth,[46] and used this to postulate the aggregation state of small peptides.[47] In a similar attempt Jeschke and co-workers pointed out the dimeric structure of an antiporter[48] in combination with MD calculations. But a pure experimental validation and calibration of the PELDOR "Spin Counting" method on fully characterized systems for up to four spins was lacking.

Regarding the inclusion of exchange coupling in the PELDOR analysis, three examples have been reported in literature. A theoretical description with examples of molecules exhibiting very small exchange coupling constants were reported already in 1998[33,49] and later on for spin labeled copper(II)-porphyrine systems.[50,51] An early 3-pulse PELDOR experiment disentangled an exchange coupling of 11 MHz.[44]

In a first step, these evaluations regarding a) - d) are based on synthetic organic model compounds obtained from the author (model compounds from collaborators are indicated with roman numbers) and DNA molecules as well as on simulating PELDOR data demonstrating the powerful interplay of dipolar EPR spectroscopy in combination with organic synthesis.

1.1.1 Motivation and Aim

This thesis located at the interface of EPR spectroscopy and organic synthesis in conjunction with according data simulation aims to obtain in depth understanding of PELDOR time domain signals and therefore to advance the method beyond its original purpose of measuring distances. The main goal of this work is to systematically disentangle a maximum amount information from the experimental data using a commercially available pulsed EPR spectrometer operating at X-band frequency. Thus, (poly)nitroxide radical model compounds need to be synthesized and fully characterized in order to be employed as benchmark systems. These systems can be utilized in proof of principle studies extracting the conformational flexibility via PESIM or to validate PELDOR "Spin Counting" allowing to determine the number of monomers in oligomers. These planned methodological advancements are of extreme value regarding conformational (re)arrangements of large biological systems. Hence, an application to biomolecules such as DNA is aspired.

Furthermore, suitable synthetic molecules may probe unraveling dipolar from exchange coupling being important for the design of molecular magnets.

1.1.2 Publications and Conference Contributions

The majority of the results stated in this thesis has been published in scientific journals or either presented as posters or orally. Only first author poster are listed.

1.1.3 Publications

1.) D. Margraf, D. Schuetz, T. F. Prisner, J. W. Bats
Biphenyl-4,4'-diyl-bis(2,2,5,5-tetramethyl-1-oxyl-3-pyrroline-3-carboxylate)
Acta Crystallographica, 2009, E65, o1784.

2.) D. Margraf, P. Cekan, T. F. Prisner, S. Th. Sigurdsson, O. Schiemann
Ferro- and Antiferromagnetic Exchange Coupling Constants in PELDOR Spectra
Physical Chemistry Chemical Physics, 2009, DOI:10.1039/ B905524J.

3.) A. Marko, D. Margraf, H. Yu, Y. Mu, G. Stock, T. F. Prisner
Molecular orientation studies by pulsed electron-electron double resonance experiments
Journal of Chemical Physics, 2009, 130, 064102, DOI:10.1063/1.3073040.

4.) O. Schiemann, P. Cekan, D. Margraf, T. F. Prisner, S. Th. Sigurdsson
Relative orientation of rigid nitroxides by PELDOR: Beyond distance measurements in nucleic acids
Angewandte Chemie, 2009, 121, 3342-3345.

5.) D. Margraf, B. E. Bode, A. Marko, O. Schiemann, T. F. Prisner
Conformational flexibility of nitroxide biradicals determined by X-band PELDOR experiments
Molecular Physics, 2007, 115, 2153-2160.

6.) B. E. Bode, D. Margraf, J. Plackmeyer, G. Dürner, T. F. Prisner, O. Schiemann
Counting the monomers in nanometer-sized oligomers
Journal of the American Chemical Society, 2007, 129, 6736-6745.

7.) T. Müller, D. Margraf, Y. Syha, H. R. Nasiri, C. Kaiser, R. Maier, B. Boltres, M. Juhasz, C. Reed*

Unusually stable vinyl cations in Recent Developments in Carbocation and Onium Chemistry edited by K. K. Laali, Oxford University Press, 2007, ISBN 13: 978-0-8412-7414-3.

8.) D. Margraf, J. W. Bats

1,3,5-Triiodobenzene

Acta Crystallographica, 2006, E62, o502-o504.

9.) T. Müller, D. Margraf, Y. Syha*

σ-stabilization versus π-resonance in α-aryl-substituted vinylcations

Journal of the American Chemical Society, 2005, 127, 10852-10860.

D. Schuetz, D. Margraf, T. F. Prisner, J. W. Bats

Triphenylmethane-4,4',4''-triyl tris(2,2,5,5-tetramethyl-1-oxyl-3-pyrroline-3-carboxylate) tris(benzene) solvate

Acta Crystallographica (submitted)

Observation of DNA" breathing" motions

(in preparation)

Structural Analysis of Spin Labeled DNA Molecules

(in preparation)

* Obtained during the author's diploma thesis in the group of Prof. Dr. Thomas Müller, now Carl von Ossietzki University Oldenburg.

1.1.4 Oral Presentations

1.) "Pulsed Electron-Electron Double Resonance – Beyond Distance Measurements",
Meeting of the Center of Biomolecular Magnetic Resonance
Kronberg, 2009.

2.) "Pulsed Electron-Electron Double Resonance – Beyond Distance Measurements"
Seminar of the Institute of Physical and Theoretical Chemistry,
Frankfurt am Main, 2009

3.) "Pulsed Electron-Electron Double Resonance – Beyond Measuring Distances,
9th Spring Symposium of the German Young Chemical Society
Chemnitz, 2007.

4.) "Synthesis of (poly)radical model system for Pulsed Electron-Electron Double Resonance Spectroscopy",
Retreat DFG Sonderforschungsbereich 579 RNA Ligand Interactions
Weilburg, 2005.

1.1.5 Conference Contributions (Poster)

1.) "Pulsed Electron-Electron Double Resonance: Beyond Measuring Distances"
D. Margraf, P. Cekan, T. F. Prisner, Snorri Th. Sigurdsson, O. Schiemann, *EUROMAR Magnetic Resonance Conference*, Tarragona, Spain, 2007.

2.) "Pulsed Electron-Electron Double Resonance: Beyond Measuring Distances"
D. Margraf, P. Cekan, T. F. Prisner, Snorri Th. Sigurdsson, O. Schiemann, *29th Discussion Meeting of the German Chemical Society's Magnetic Resonance Division,*
Göttingen, 2007.

3.) "Pulsed Electron-Electron Double Resonance: Beyond Measuring Distances"
D. Margraf, P. Cekan, T. F. Prisner, Snorri Th. Sigurdsson, O. Schiemann, *Wissenschaftsforum (General Assembly of the German Chemical Society)*, Ulm, 2007.

4.) “Pulsed Electron-Electron Double Resonance: Beyond Measuring Distances”
D. Margraf, P. Cekan, T. F. Prisner, Snorri Th. Sigurdsson, O. Schiemann, *234th General Assembly of the American Chemical Society*, Boston, MA, USA, 2007 (invited contribution).

5.) “Triradical Model Systems for Pulsed Electron-Electron Double Resonance Spectroscopy”
D. Margraf, B. E. Bode, T. F. Prisner, O. Schiemann, *27th Discussion Meeting of the German Chemical Society’s Magnetic Resonance Division*, Max Planck Institute for Polymer Research, Mainz, 2005.

6.) “Triradical Model Systems for Pulsed Electron-Electron Double Resonance Spectroscopy”
D. Margraf, B. E. Bode, T. F. Prisner, O. Schiemann, *3rd European EPR Summer School and COST Training School*, Wiesbaden, 2005.

7.) “Synthesis of Triradical Model Systems for Nanometer Distance Measurements using Pulsed Electron-Electron Double Resonance Spectroscopy”
D. Margraf, T. F. Prisner, O. Schiemann, *104th General Assembly of the Bunsen Society for Physical Chemistry*, Frankfurt am Main, 2005.

2. Synthesis of (poly)radical model systems

This chapter has been published in the *Journal of the American Chemical Society*, **129**, 6736, 2007. It is entitled "Counting the Monomers in Nanometer-Sized Oligomers by PELDOR".[52] The author contributed the synthesis of polyradical model compounds. Dr. Jörn Plackmeyer, Johann Wolfgang Goethe University Frankfurt, is acknowledged for the last two coupling and purification steps in the synthesis of **4** and optimization of the synthetic pathway to **6**.[53]

2.1. Abstract

Two biradicals, a symmetric and an asymmetric triradical, and a tetraradical were synthesized in a convergent reaction scheme via palladium-catalyzed cross-coupling reactions employing an according protection group scheme. All yielded nitroxide polyradicals are chemically stable and bear well defined distances between the spin centers and lay the experimental base for "Spin Counting" experiments, the determination of conformational flexibility of nitroxides and further molecular orientation studies using PELDOR spectroscopy. The model systems mimic different geometries and aggregation states of biomolecules. Furthermore, two novel crystal structures could be obtained (see Section 3).

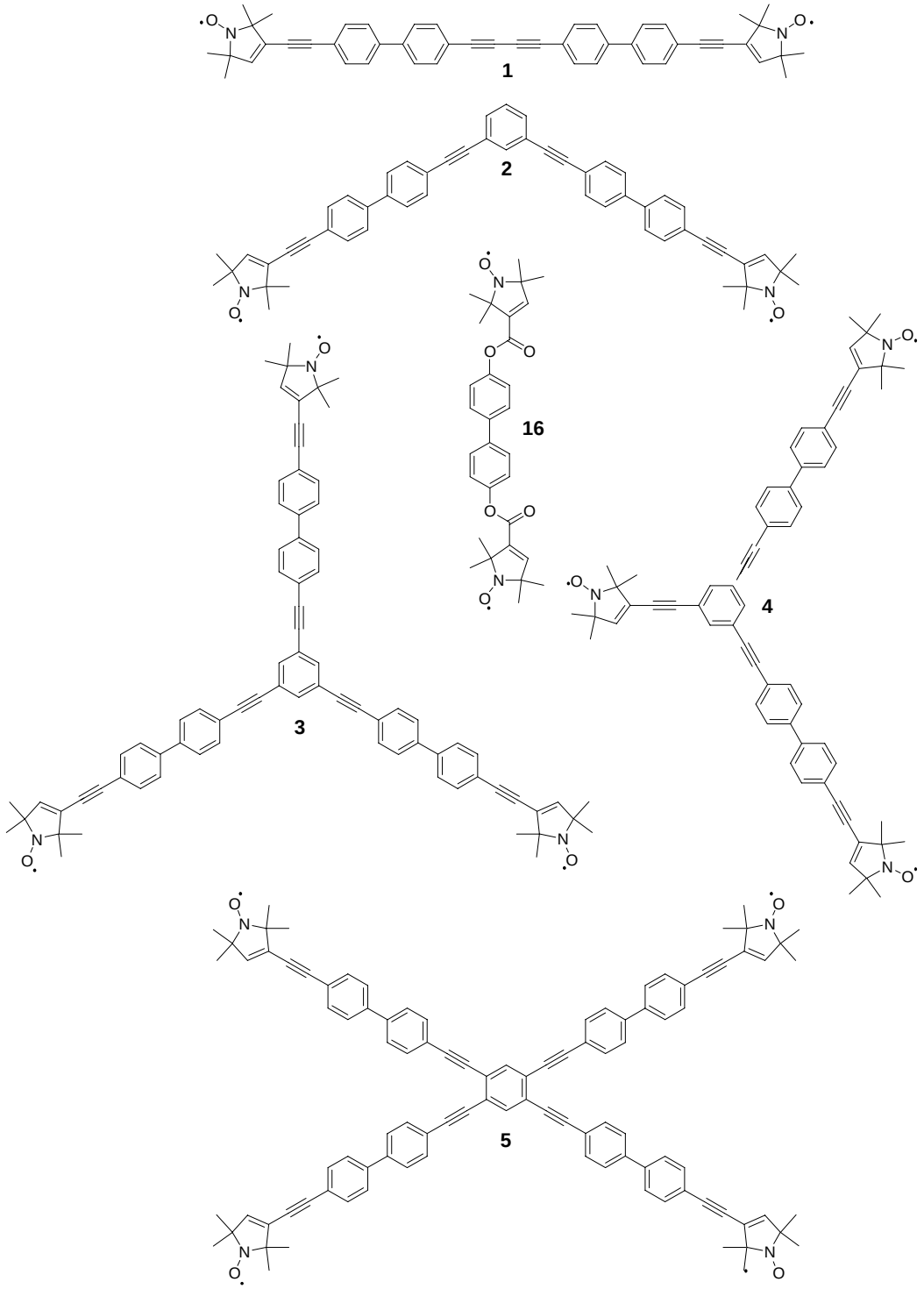

Scheme 1: Overview of synthesized target polyradical PELDOR model systems.

2.2 Introduction

Suitable model systems for PELDOR "Spin Counting" should be chemically stable, rigid and have a spin-spin distance that is well within the limit of the method (15 Å - 80 Å).[32,14] The polynitroxide radicals **1** - **5** (see Scheme 1) containing fairly rigid ethynyl substituted aromatic spacers fulfill these requirements. In addition, the use of these spacers allowed synthesizing molecules **1** - **5** from a small pool of building blocks.

2.3 Results and Discussion

The nitroxide 3-ethynyl-1-oxyl-2,2,5,5-tetramethylpyrroline **6**, which is commonly used as a spin label for RNA or DNA,[54,55,56] was employed as the spin bearing group. It was prepared from 2,2,6,6-tetramethyl-4-oxopiperidine[57,58] in modification to the procedure described by Hideg et al.[59] (see Scheme 2).

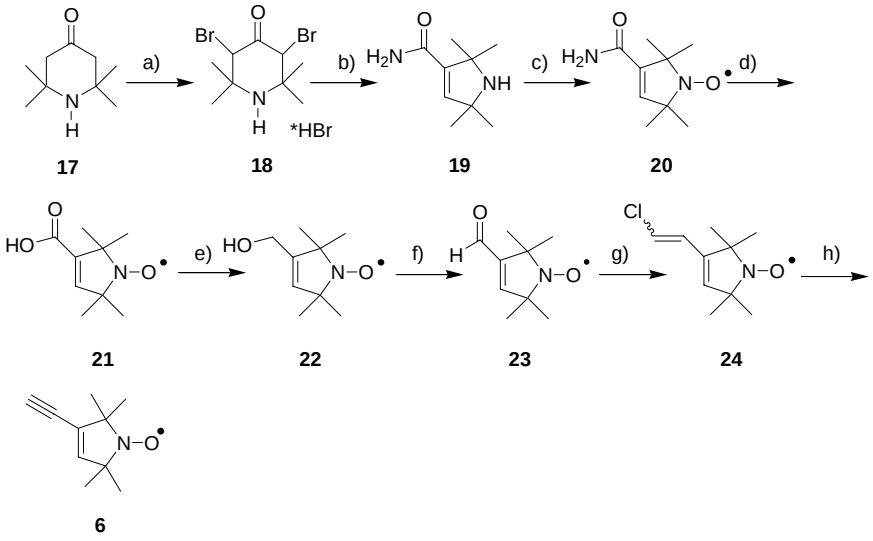

Scheme 2: Synthesis of compound **6**.
a) Br_2, CH_3COOH, b) NH_3, KOH, c) Na_2WO_4*$2H_20$, EDTA, H_2O_2, d) NaOH, e) Red-Al ®, f) DMSO, $C_2O_2Cl_2$, NEt_3, CH_2Cl_2, g) $ClCH_2PPh_3Cl$, n-BuLi, h) KO^tBu

Compound **17** was enolized and brominated under acidic conditions to yield **18** followed by a Favorskii rearrangement leading to the five membered ring species **19**. The nitroxide moiety in molecule **20** was obtained via oxidation using hydrogen peroxide. After saponification of the carboxylic amide to **21** and reduction to the alcohol **22,** a Correy-Fuchs type sequence consisting of a Swern oxidation to **23**, a

Wittig reaction to **24** and an elimination reaction gave **6** in an overall yield of 7%. This reaction scheme[53] proved to be superior in yield and economic terms as compared to a Weinreb amide reduction of **21** to **23** as originally proposed by Hideg et al.[59] An alternative access to biradicals is e.g. the esterification of 4,4'-Dihydroxybiphenyl with **21** to **16** which was prepared as a reference compound.[44] However, molecule **6** was converted to the polyradical precursor **9** via the coupling and protection sequence shown in Scheme 3.

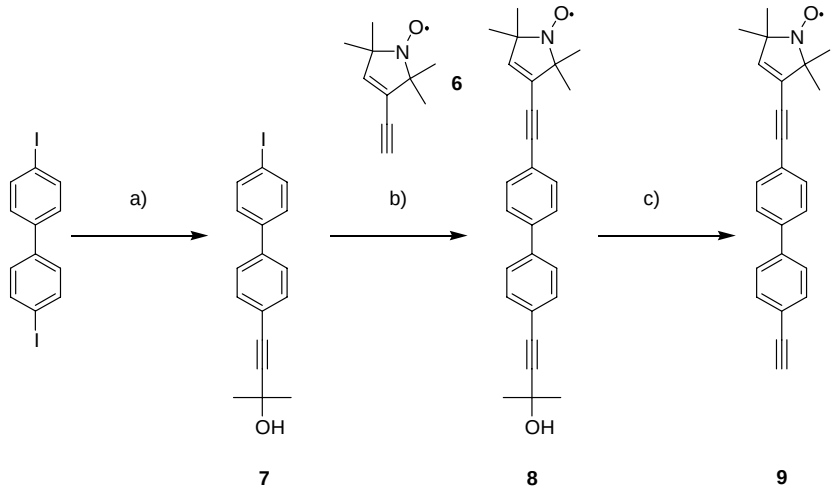

Scheme 3: Synthesis of polyradical precursor **9.**
a) $HNEt_2$, benzene, CuI, $PdCl_2(PPh_3)_2$, 2-methyl-3-butyn-2-ol, 43%; b) NEt_3, piperidine, DMF, CuI, $PdCl_2(C_6H_5CN)_2$, spin label **6**, 74%; c) KOH, toluene, 93%.

Firstly, a protected acetylene was attached to 4,4'-Diiodobiphenyl and the nitroxide spin label **6** was added in a second step for reasons of synthesis economy, as **6** has to be synthesized in eight steps. Due to the fact that the nitroxyl moiety is easily reduced or oxidized,[60,61]a protective group strategy for acetylene units and cleavage conditions not interfering with the nitroxyl functionality had to be applied. Here, the polar protecting group 2-hydroxypropyl was chosen, because it facilitates separation via column chromatography in contrast to non-polar protecting groups as trimethylsilane.[62,63] The 2-hydroxypropyl group was favored over hydroxymethyl due to the lower toxicity of the reagent.[64,65]Purification of **7** is readily performed and obtained 43% yield.

Nitroxide **6** is can be attached to the halogeno-substituted sp^2-carbon atom in **7** by means of transition metal catalyzed cross coupling reactions such as the Sonogashira coupling.[66,67,68,69] Nitroxides can be coupled in high yields (84%)[70] under mild

conditions.[71] However, Sonogashira couplings involving 1,3-enynes such as **6** are usually up to 17% lower in yield than those using non-conjugated terminal acetylenes.[72,73] Here, the protected precursor **8** was obtained in 74% yield. Molecule **8** was converted to the deprotected[74,75,76,77] precursor **9** in 93% yield by reacting **8** and KOH in toluene at 110 °C.[78] Deprotection of **8** can be monitored qualitatively via IR-spectroscopy due to the appearance of the characteristic ethynyl-H stretching mode at 3206 cm^{-1}. Compound **9** was used without further purification. Coupling of **9** to **7** allows in principle elongation of the aromatic spacer. However, the poor solubility of the elongated spacer made further coupling reactions difficult. Only mass spectrometric evidence was found. Nevertheless, the terminal acetylene **9** was reacted with either 1,3,5-triiodobenzene **10**[79,80] or 1,2,4,5-tetraiodobenzene **11**[81] leading to the symmetric polyradical molecules **3** and **5**, respectively.

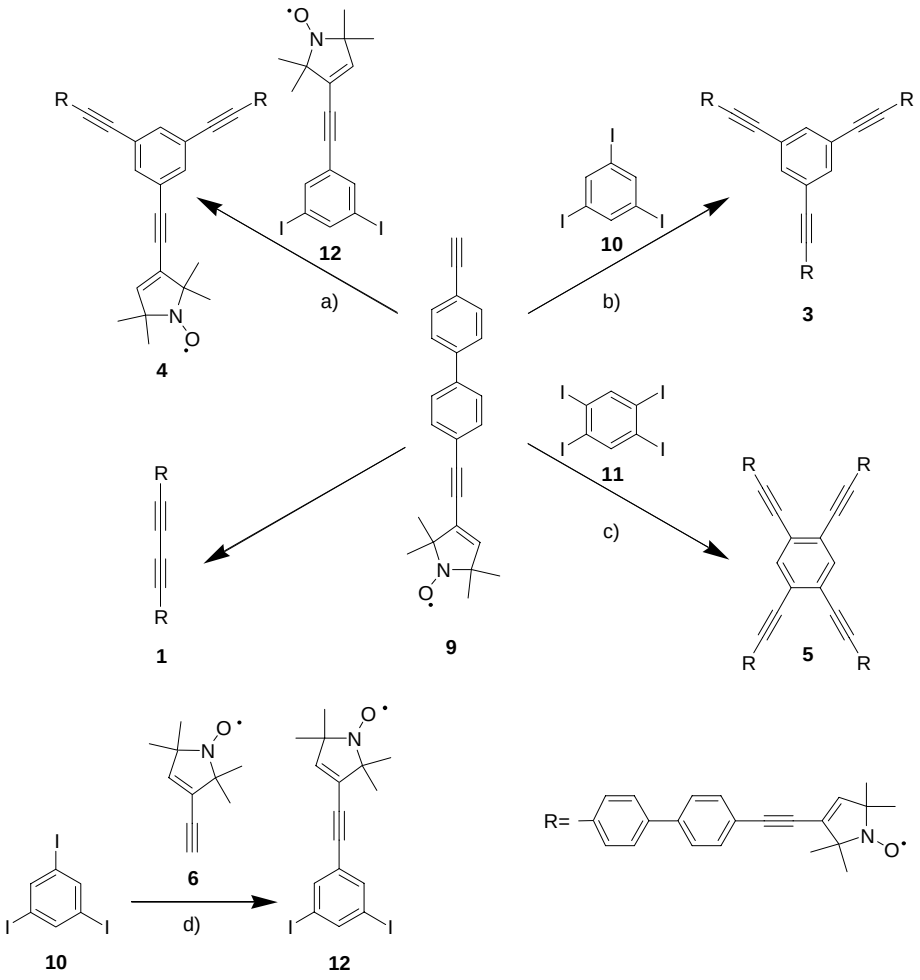

Scheme 4: Synthesis of polyradical systems.
a) NEt_3, DMF, CuI, $PdCl_2(C_6H_5CN)_2$, **12**, 66%; b) $HNEt_2$, C_6H_6, CuI, $PdCl_2(PPh_3)_2$, **10**, 14%; c) NEt_3, piperidine, DMF, CuI, $PdCl_2(C_6H_5CN)_2$, **11**, 18%; d) NEt_3, piperidine, DMF, CuI, $PdCl_2(C_6H_5CN)_2$, **6**, 32%.

The asymmetric triradical **4** was obtained by coupling **12**, obtained by reacting **6** with **10**, to precursor **9**. Molecules **3**, **4** and **5** were yielded in 14%, 66% and 18%, respectively. The low yields observed when coupling more than one acetylene unit to an aromatic system are commonly observed for phenylacetylene systems.[82]

Yields of Sonogashira couplings involving nitroxides **6** and **9** could be raised by up to 18% using bis(benzonitrile)palladium(II)chloride as a catalyst and either triethylamine or a 1:5 mixture of piperidine and triethylamine instead of bis(triphenylphosphine)-palladium(II)chloride in triethyl- or diethylamine (see Scheme 4).

The initial attempt to couple **9** two times to **10** to obtain a biradical from the given pool of building blocks failed, as the product could not be isolated as a pure substance. Synthesizing the corresponding non-iodo substituted biradical **2** from 1,3-Diiodobenzene did also not succeed again due to problems in purification. These purification problems are addressed to the dimerization of **9** to the homo-coupling product **1** and further uncharacterized by-products.

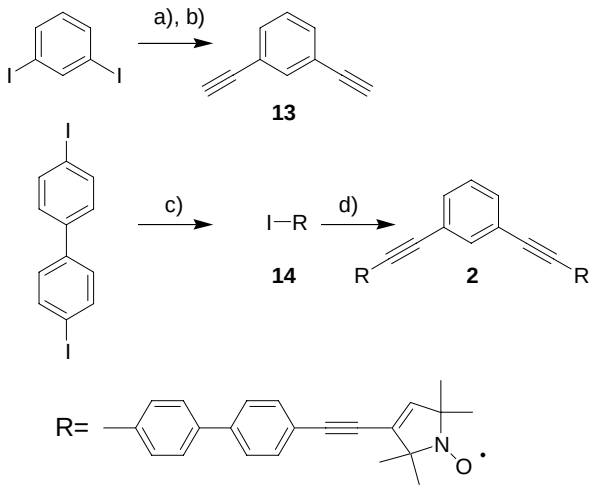

Scheme 5: Synthesis of biradical **4**
a) NEt_3, piperidine, DMF, CuI, $PdCl_2(C_6H_5CN)_2$, trimethylsilylethyne; b) TBAF, THF; c) NEt_3, piperidine, DMF, CuI, $PdCl_2(PPh3)_2$, **6**, 33%; d) NEt_3, piperidine, DMF, CuI, $PdCl_2(C_6H_5CN)_2$, **13**, 11%.

The formation of **1** could not be avoided in any Sonogashira coupling using precursor **9**. It can be isolated in a yield of up to 15% following the synthesis of **3 - 5** given in Scheme 3. To overcome these problems, 1,3-Diethynylbenzene **13**[83] was synthesized and attached to the iodo-substituted radical **14** (see Scheme 5). In that manner the formation of **1** is excluded and **14** was obtained in 45% yield. The homo-coupling products of **13** were readily separated off via column chromatography. (*Note: The colorless oil **13** is known to explode upon attempts of vacuum distillation. **13** should*

only be distilled at high vacuum and temperatures of less than 60 °C in well-shielded equipment. Only limited quantities should be stored or manipulated as pure, undiluted material). Molecules **3** and **5** were not prepared using the strategy shown in Scheme 4 because of the increasing reactive character of higher polyethynyl compounds such as 1,2,4,5-tetraethynylbenzene.[84]

2.4 Conclusion

Hence, convenient routes to rigid, shape persistent polyradical systems have been established by means of Sonogashira couplings and a corresponding polar protective group strategy. This route is easily extendable to a variety of iodo substituted arylic compounds. In comparison to a synthesis strategy where a spin label bearing an acid functionality is attached via esterification as in **16** in the final step of the synthesis[85] less coupling and deprotection steps are needed here. The overall yields are comparable for both strategies.

2.5 Experimental Section

Analytic mostly relied on mass spectrometry such as EI, ESI and MALDI and elemental analysis, as the target compounds are paramagnetic and thus lead to line broadening in ^{1}H-NMR spectra. NMR-signals resulting from the spin label moiety could not be detected. Proton nuclear magnetic resonance spectra of diamagnetic molecules were acquired at 250 MHz on a Bruker AM-250 spectrometer and calibrated using residual non-deuterated solvents as internal standard ($\delta_{CHCl3} = 7.240$). For nitroxides such as **6** the loss of several methyl groups (M - 15, M - 30, …) upon ionization in mass spectrometry is commonly observed.[86,87] This fragmentation could also be seen in most mass spectra of the presented target molecules. EI mass spectra were recorded on a CH7A spectrometer from MAT. ESI mass spectra were acquired on a LCQ Classic spectrometer from Thermo Electron. MALDI mass spectra were recorded on a Voyager DE-Pro or STR spectrometer from Applied Biosystems.
The deprotection of **8** to **9** was monitored by means of IR-spectroscopy due to the appearance of the characteristic ethynyl-H stretching mode on a Jasco FT-IR 420 spectrometer using KBr pellets. Benzene was distilled from Na under argon atmosphere and amines were distilled from CaH_2 under argon atmosphere. Dry DMF was degassed with argon. Dry toluene was degassed by several freeze-thaw cycles. Coupling reactions and deprotection steps were carried out applying standard Schlenck-technique under argon atmosphere.

1 The homo-coupling by-product **1** can be isolated from Sonogashira couplings following scheme 3. Column chromatography on aluminumoxide Super 2 in dichloromethane yields **1** as a white powder (R_f: 0.6). It was isolated from the synthesis of tetraradical **5** due to the largest difference in R_f-values (13 mg, 4%). MALDI-TOF-MS (matrix, DHB) m/z calcd. for $C_{48}H_{42}N_2O_2$: 678.86; Found: 679.8 (M + H, 10%), 663.83 (M - CH_3, 30%), 648.85 (M - 2xCH_3, 45%), 633.87 (M - 3xCH_3, 100%), 617.90 (M - 4xCH_3, 79%), 602.90 (M - 5xCH_3, 20%). Anal. Calcd. for $C_{48}H_{42}N_2O_2$: C, 84.92; H, 6.24; N, 3.97; Found: C, 85.15; H, 6.42; N, 4.13.

2 200 mg of **13**, 17 mg $PdCl_2(C_6H_5CN)_2$ and 4 mg CuI are dissolved in 30 ml of dry, degassed NEt_3:piperidine (5:1) and 5 ml DMF in a Schlenck-flask. 343 mg of **14** and 6 mg PPh_3 in 15 ml NEt_3:piperidine (5:1) and 5 ml DMF are added drop wise to

the stirred yellow solution. The formation of a white precipitate is observed. After 16 hours at room temperature the reaction mixture is quenched with water and the solvents are removed in vacuo. The solids are redissolved in dichloromethane and water. The phases are separated and the organic phase is washed with water and dried over Na_2SO_4. Column chromatography on aluminumoxide Super 2 in dichloro-methane yielded 15 mg (11%) of a white powder in the second band (R_f: 0.6). **2** is recrystallized in $CHCl_3$. ESI-MS(+) m/z calcd. for $C_{54}H_{46}N_2O_2$: 754.96; Found: 755.1 (M, 30%), 754.01 (M – H, 51%), 738.21 (M - H- CH_3, 100%), 694.27 (M - 4xCH_3, 15%). Anal. Calcd. for $C_{54}H_{46}N_2O_2$: C, 85.91; H, 6.14; N, 3.49; Found: C, 85.74; H, 6.32; N, 3.71.

3 36 mg of **10** are dissolved in 10 ml dry, degassed benzene and 20 ml dry, degassed diethylamine in a Schlenck-flask. 25 mg of $PdCl_2(PPh_3)_2$, 25 mg CuI, 50 mg PPh_3 and 147 mg of **9** are added. The formation of a white precipitate in the yellow solution is observed. The solution is stirred at 55°C for 100 hours. After the reaction is quenched with water the solvents are removed in vacuo and the solids are redissolved in dichloromethane and water. The phases are separated and the organic phase is washed with water and dried over $MgSO_4$. Column chromatography on aluminumoxide Super 2 in dichloromethane yielded 12 mg (14%) of a white powder in the last band (R_f: 0,2). **3** is recrystallized in benzene/n-pentane. ESI-MS(+) m/z calcd. for $C_{78}H_{66}N_3O_3$: 1093.38; Found: 1095.31 (M + 2H, 24%), 1094.23 (M + H, 49%), 1093.22 (M, 80%), 1092.11 (M - H, 100%). Anal. Calcd. for $C_{78}H_{66}N_3O_3$: C, 85.68; H, 6.08; N, 3.84; Found: C, 85.84; H, 6.02; N, 3.97.

4 68 mg of **12**, 8 mg $PdCl_2(C_6H_5CN)_2$ and 4 mg CuI are dissolved in 20 ml of dry, degassed NEt_3 and 5 ml DMF in a Schlenck-flask. 140 mg of **9** and 5 mg PPh_3 in 8 ml dry, degassed NEt_3 and 2 ml DMF are added drop wise to the stirred yellow solution. The formation of a white precipitate is observed. After 16 hours at room temperature the reaction mixture is heated to 55°C for 2 hours and quenched with water. The solvents are removed in vacuo. The solids are redissolved in dichloromethane and water. The phases are separated and the organic phase is washed with water and dried over Na_2SO_4. Column chromatography on aluminumoxide Super 2 in dichloromethane yielded 83 mg (66%) of a white powder in the second band (R_f: 0.3). **4** is recrystallized from benzene/hexanes. ESI-MS(+) m/z calcd. for $C_{64}H_{58}N_3O_3$:

917.16; Found: 918.27 (M + H, 44%), 917.15 (M, 63%), 916.01 (M – H, 100%). Anal. Calcd. for $C_{64}H_{58}N_3O_3$: C, 83.81; H, 6.37; N, 4.58; Found: C, 83.54; H, 6.58; N, 4.32.

5 93 mg of **11**, 8 mg $PdCl_2(C_6H_5CN)_2$ and 2 mg CuI are dissolved in 15 ml of dry, degassed NEt_3:piperidine (5:1) in a Schlenck-flask. 343 mg of **9** and 6 mg PPh_3 in 15 ml dry, degassed NEt_3:piperidine (5:1) and 5 ml dry, degassed DMF are added drop wise to the stirred yellow solution. The formation of a white precipitate is observed. After 16 hours at room temperature the reaction mixture is quenched with water and the solvents are removed in vacuo. The solids are redissolved in dichloromethane and water. The phases are separated and the organic phase is washed with water and dried over Na_2SO_4. Column chromatography on aluminumoxide Super 2 in dichloromethane yielded 26 mg (18%) of an intensely yellow powder in the last band (R_f: 0,1). **5** is recrystallized in benzene. ESI-MS(+) m/z calcd. for $C_{102}H_{86}N_4O_4$: 1431.80; Found: 1325.34 (M - 7xCH_3, 96%), 1000.39 (M - (9-H) – 6xCH_3, 31%), 663.26 (M - (2x9-H) - 6xCH_3, 100%). Anal. Calcd. for $C_{102}H_{86}N_4O_4$: C, 85.68; H, 6.08; N, 3.84; Found: C, 85.84; H, 6.02; N, 3.97.

6 10 g of **24** in 200 ml of THF are stirred with 15,36 g KO^{t}Bu at 55°C for 2 hours. The red-brown reaction mixture is quenched with water, extracted with diethylether (3x100 ml) and dried over $MgSO_4$ yielding a greenish brown powder. Sublimation at $3x10^{-3}$ mbar (52°C) leads to 4,05 g of intensely yellow crystals of **6**. (yield: 48% over 2 steps). EI-MS(+) m/z calcd. for $C_{10}H_{14}NO$: 164.22; Found: 134 (M - 2xCH_3; 100%). Anal. Calcd. for $C_{10}H_{14}NO$: C, 73.14; H, 8.59; N, 8.53; Found: C, 73.35; H: 8.98; N, 8.92.

7 5 g of 4',4-Diiodobiphenyl (90%, tech.) are dissolved under reflux in 40 ml dry, degassed benzene and 60 ml dry, degassed diethylamine in a Schlenck-flask. 175 mg of $PdCl_2(PPh_3)_2$, 175 mg CuI, 350 mg PPh_3 and 1.2 ml of degassed 2-Methyl-3-butyn-2-ol are added. The formation of a white precipitate is observed. The red-brown solution is stirred at reflux for 16 hours. After the reaction is quenched with water the solvents are removed in vacuo and the solids are redissolved in dichloromethane and water. The phases are separated and the organic phase is washed with water and dried over $MgSO_4$. Column chromatography on aluminumoxide Super 2 in dichloro-

methane yielded 1.56 g (43%) of a white powder in the second band (R_f: 0.5). **7** is recrystallized in CH_2Cl_2/n-pentane. ^{1}H-NMR ($CDCl_3$, 250 MHz): 1.616 (s, 6H, CH_3); 7.280 (d, 2H, Ar-H, $^3J_{HH}$ = 8.5 Hz); 7.467 (s, 4H, Ar-H); 7.730 (d, 2H, Ar-H, $^3J_{HH}$ = 8.5 Hz). MALDI-TOF-MS (matrix, HCCA) m/z calcd. for $C_{17}H_{15}IO$: 362,20; Found: 345.01 (M – OH, 100%). Anal. Calcd. for $C_{17}H_{15}IO$: C, 56.37; H, 4.17; Found: C, 56.33; H, 4.19.

8 884 mg of **7** and 500 mg of **6** are dissolved in 50 ml dry, degassed NEt_3 and 10 ml dry, degassed piperidine in a Schlenck-flask. 94 mg of $PdCl_2(C_6H_5CN)_2$, 19 mg CuI and 59 mg PPh_3 are added. The formation of a white precipitate in the yellow solution is observed. The solution is stirred at room temperature overnight. After the reaction is quenched with water the solvents are removed in vacuo and the solids are redissolved in dichloromethane and water. The phases are separated and the organic phase is washed with water and dried over Na_2SO_4. Column chromatography on silica gel in THF:toluene (1:5) yielded 722 mg (74%) of a golden yellow powder in the fourth band (R_f: 0.6). **8** is recrystallized in THF/toluene at –30°C. EI-MS(+) m/z calcd. for $C_{27}H_{28}NO_2$: 398.21; Found: 400 (M + 2H, 32%), 369 (M - 2xCH_3, 100%), 354 (M - 3xCH_3, 33%), 340 (M – acetone, 31%), 59 (acetone, 2%). Anal. Calcd. for $C_{27}H_{28}NO_2$: C, 81.37; H, 7.19; N, 3.50; Found: C, 81.31; H, 7.08; N, 3.51.

9 500 mg of **8** are dissolved in 25 ml of dry, degassed toluene in a Schlenck-flask. 560 mg of KOH are added and the yellow solution is immersed into a pre-heated oil bath of 110°C for 5 minutes. The oil bath is removed and after cooling down the solids are filtered off and extracted with $CHCl_3$. The organic phases are combined and the solvents are removed in vacuo. **9** is directly converted after aqueous work-up in CH_2Cl_2 and drying of the organic phase with Na_2SO_4 without any further purification (yield: 393 mg; 93%). MALDI-TOF-MS (matrix, DHB) m/z calcd. for $C_{24}H_{22}NO$: 340.44; Found: 342.00 (M + 2H, 39%), 341.00 (M + H, 67%), 339.98 (M, 100%), 325.99 (M - CH_3, 46%), 310.03 (M - 2xCH_3, 93%). IR (KBr, cm^{-1}): 3446, 3206, 3055, 2979, 2925, 2853, 2101, 1491, 1460, 1439, 1370, 1359, 1309, 1248, 1163, 1078, 1002, 878, 855, 822, 739, 701, 677, 363, 565, 533, 442, 429.

12 228 mg of **10**, 19 mg $PdCl_2(C_6H_5CN)_2$ and 10 mg CuI are dissolved in 20 ml of dry, degassed NEt_3:piperidine (5:1) in a Schlenck-flask. 82 mg of **6** and 13 mg

PPh_3 in 10 ml dry, degassed NEt_3:piperidine (5:1) are added dropwise to the stirred yellow solution. The formation of a white precipitate is observed. After 16 hours at room temperature the reaction mixture is heated to 55°C for 2 hours and quenched with water. The solvents are removed in vacuo. The solids are redissolved in dichloromethane and water. The phases are separated and the organic phase is washed with water and dried over Na_2SO_4. Column chromatography on aluminumoxide Super 2 in dichloromethane:hexanes (1:1) yielded 78 mg (32%) of a yellow powder in the second band (R_f: 0.7). **12** is recrystallized from hexanes. MALDI-TOF-MS (matrix, DHB) m/z calcd. for $C_{16}H_{16}I_2NO$: 492.10; Found: 494.03 (M + 2H, 100%). Anal. Calcd. for $C_{16}H_{16}I_2NO$: C, 39.05; H, 3.28; N, 2.85; Found: C, 39.29; H, 3.35; N, 2.74.

14 1 g of 4',4-Diiodobiphenyl, 50 mg $PdCl_2(PPh_3)_2$ and 50 mg CuI are dissolved in 30 ml of dry, degassed NEt_3:piperidine (5:1) and 5 ml DMF in a Schlenck-flask. 404 mg of **6** and 50 mg PPh_3 in 25 ml NEt_3:piperidine (5:1) and 5 ml DMF are added dropwise to the stirred yellow solution at 0°C. The ice bath is removed after 1 hour. The formation of white precipitates is observed. After 16 hours at room temperature the reaction mixture is quenched with water and the solvents are removed in vacuo. The solids are redissolved in dichloromethane and water. The phases are separated and the organic phase is washed with water and dried over Na_2SO_4. Column chromatography on silica gel in dichloromethane:methanol (30:1) yielded 360 mg (33%) of a yellow powder in the third band (R_f: 0.7). EI-MS m/z calcd. for $C_{22}H_{21}INO$: 442.32; Found: 442 (M, 2%), 412 (M - 2xCH_3, 51%), 397 (M - 3xCH_3, 11%). Anal. Calcd. for $C_{22}H_{21}INO$: C, 59.74; H, 4.78; N, 3.16; Found: C, 59.82; H, 4.77; N, 3.30.

16 2.67 g of **21** 686 mg 4,4'-Dihydroxybiphenyl, 2.2 g N,N-dimethylamino-pyridine and 18.1 ml dicyclohexylcarbodiimide (1mM in CH_2Cl_2) are dissolved in 40 ml dry THF in a Schlenck-flask and stirred overnight. The white precipitate is filtered off and the solvents are removed in vacuo. The yellow solids are redissolved in dichloromethane and column chromatography on aluminumoxide Super 2 in diethylether:n-hexanes (3:1) yields 745 mg (86%) of **16** (R_f: 0.5) in the first band. Single crystals suitable for X-ray analysis were obtained after recrystallization in toluene:n-hexane (3:1). EI-MS m/z calcd. for $C_{30}H_{34}N_2O_6$: 518.60; Found: 521

(M + 2H, 100%). Anal. Calcd. for $C_{30}H_{34}N_2O_6$: C, 69.48; H, 6.61; N 5.40; Found: C, 69.31; H, 6.63; N 5.46.

18 60 g of **17** (90% techn. pur.) are dissolved in 360 ml of conc. acetic acid. 39.8 ml of bromine are added drop wise at room temperature to the red-brown solution. The reaction mixture is heated to 60°C for 30 minutes and product is filtered off and washed with cold water yielding a white powder that is used without further purification. (95% yield).

19 136 g of **18** are dissolved in 460 ml conc. aq. (33%) ammonia and stirred for 2 hours at room temperature. The solution is filtered and the clear orange filtrate is saturated with KOH in a 3L Erlenmeyer flask (cave: formation of foam). The formation of a precipitate is observed. Recrystallization in toluene leads to pale yellow crystals. The product is directly converted without further purification.

20 55 g of **19** are suspended in 600 ml dest. water. 3.04 g of EDTA, 3.04 g Na_2WO_4*$2H_2O$ and 60.75 ml of 30% aq. H_2O_2 are added and stirred for 5 minutes. After 5 days at 4°C 23.94 g of intensely yellow crystals are obtained and filtered off (yield: 40% over 2 steps). ESI-MS(+) m/z calcd. for $C_9H_{15}N_2O_2$: 183.23; Found: 181.8 (M – 2 H, 100%).

21 23.94 g of **20** are suspended in 600 ml of 10% aq. NaOH and heated to reflux for 2 hours. The clear yellow solution is neutralized with half-concentrated aq. HCl. The yellow precipitate is filtered off. The aqueous filtrate is extracted with diethylether (3x100 ml), the combined organic phases are dried over $MgSO_4$ and the solvent is removed in vacuo. The solid phases (15.75 g of yellow crystals) are combined (yield : 64%). ESI-MS(+) m/z calcd. for $C_9H_{14}NO_3$: 184.21; Found: 182.8 (M – 2 H, 100%). Anal. Calcd. for $C_9H_{14}NO_3$: C, 58.68; H, 7.66; N, 7.60; Found: C, 58.92; H, 7.42; N, 7.86.

22 In a Schlenck-flask 15.75 g of **21** are dissolved in 250 ml abs. toluene and 95 ml of Red-Al® (Na-bis(2-methoxy-ethoxy)-AlH_2) are added drop wise to the yellow solution. The solution turns slightly orange and is heated to 60°C for 90 minutes. After cooling down to room temperature 200 ml of 5% aq. NaOH are added.

The phases are separated and the aqueous phase is extracted with toluene. The solvent of the combined organic phases is removed in vacuo and chromatographied on silica using diethylether:n-pentane (40:1, yield: 92%). %). ESI-MS(+) m/z calcd. for $C_9H_{16}NO_2$: 170.23; Found: 168.8 (M – 2 H, 100%). Anal. Calcd. for $C_9H_{16}NO_2$: C, 63.50; H, 9.47; N, 8.23; Found: C, 63.65; H, 9.38; N 8.27.

23 In a Schlenck-flask 13.35 ml of dry, abs. DMSO in 40 ml dry, abs. CH_2Cl_2 are added drop wise to 7.85 ml $C_2O_2Cl_2$ in 100 ml dry, abs. CH_2Cl_2 at –60°C. Afterwards 13.37 g of **22** in 80 ml abs. CH_2Cl_2 are added drop wise within 10 minutes. The solution turns from yellow to orange-brown. 54.95 ml of dry, abs. NEt_3 are added to the solution within 15 minutes. A white precipitate forms immediately. The reaction mixture is slowly brought to room temperature and quenched with water. The phases are separated and the organic phase is washed with brine, 1% H_2SO_4 and 5% $NaHCO_3$. Recrystallization from ethylester:n-hexane (1:3) at –20°C yielded yellow needles. Only the first fraction of crystals (8.39 g; 62%) is used.

24 At 0°C 21.65 g of $ClCH_2PPh_3Cl$ are suspended in 125 ml dry, abs. THF in a Schlenck-flask. 35.85 ml of n-BuLi (15% in n-hexane) are added drop wise. The solution is stirred at room temperature for 45 minutes. At 0°C 8.39 g of **23** in 100 ml abs. THF are added and stirred for 1.5 hours. The reaction mixture is slowly heated to 50°C for 1 hour. After quenching with water the aqueous phase is washed with diethylether (3x100 ml) and dried over $MgSO_4$. The organic phase is reduced to half its volume and filtered over a short column of silica gel. An equal volume of n-hexane is added and the white precipitate is filtered off. The light brown solution is again reduced to half its volume and kept at –20°C overnight. The yellow-orange crystals are used without further purification.

3. Crystal Structures

This chapter has been published in *Acta Crystallographica*, 2006, E62, o502-o504 and *Acta Crystallographica*, 2009, E65, o1784, and discusses the crystals structures of **10** and **16**, respectively. The author contributed the synthesis and crystallization of the compounds.

3.1 1,3,5-triidobenzene

The unit-cell dimensions of **10**[79] are rather similar to those reported for the structures of 1,3,5-trichlorobenzene and 1,3,5-tribromobenzene.[88] The space group is also identical. Thus, all three structures are probably isomorphous.

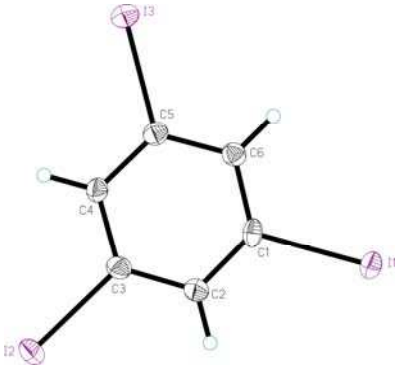

Figure 1: The molecule of **10**, showing the atom-numbering scheme. Displacement ellipsoids are drawn at the 50% probability level and H atoms are shown as small spheres of arbitrary radii.

Surprisingly, the fractional coordinates observed for **10** do not agree with those reported for the corresponding Cl and Br compounds. There is an approximate correspondence, however, if the coordinates reported for the Cl and Br compounds are shifted by a vector (1/4, 1/8, 1/4). The structures reported by Milledge and Pant[88] are based on a limited number of film reflections, and so a systematic error in those structures cannot be excluded. The molecular structure of **10** is shown in Figure 1. The benzene ring is essentially planar, with a mean deviation of the C atoms from this plane of 0.004 Å . Atom I1 deviates by 0.104 (5) Å from the plane of the benzene ring. Atoms I2 and I3 show no significant deviation from this plane [0.006 (5) Å for I2 and 0.002 (5) Å for I3]. The C-I bond lengths of 2.090 (3), 2.091 (3) and 2.101 (3) Å are in good agreement with the values of 2.086 and 2.096 Å found for two

triiodobenzene clathrates.[89] The molecules form stacks parallel to the a axis (see Figure 2) and the distance between the planes of neighboring benzene rings in the stack is 3.58 Å. Neighboring benzene rings show partially overlapping π-systems. The shortest intermolecular C(π)···C(π) distance is 3.605 (5) Å , between atoms C1 and C4(*x*-1, *y*, *z*). Deviation of atom I1 from the benzene plane is required in order to avoid a short intermolecular contact between atoms I1 and C1(x-1, y, z). The observed inter-molecular I···C distance is 3.696 (3) Å. Neighboring stacks are connected by weak intermolecular C-H···I interactions (see Figure 3).

There are three symmetry-independent C-H···I interactions, with H···I distances of 3.27, 2.37 and 3.38 Å, and C-H-I angles of 156, 160 and 164°, respectively. Equivalent reflections were merged and Friedel opposites were not merged. There are 1223 unique Friedel pairs. The value of the Flack parameter[90] indicates that the crystal was probably a twin consisting of domains with opposite chirality. H atoms were positioned geometrically and refined as riding, with C(sp^2)-H = 0.95 Å and U_{iso}(H) = 1.2 U_{eq}(C).

Single crystals of **10** were obtained from d_8-toluene.

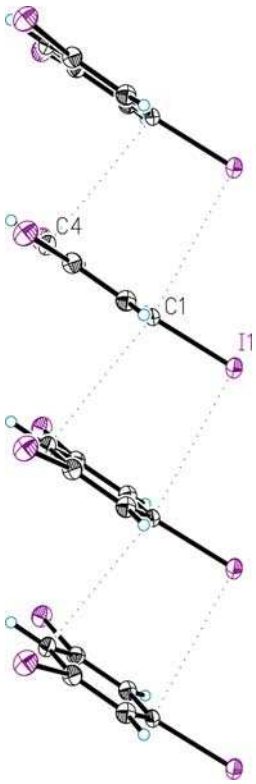

Figure 2: Molecules of **10**, stacked along the a axis. Dotted lines represent the shortest intermolecular C(π)···C(π) contact of 3.605 (5) Å and the intermolecular steric C···I contact of 3.696 (3) Å

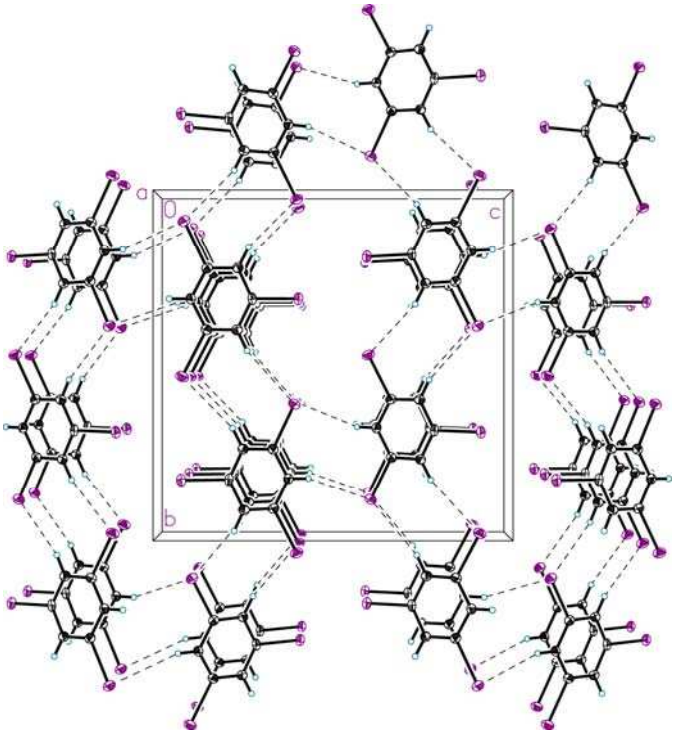

Figure 3: The crystal packing of **10**, viewed down the a axis. Weak intermolecular C-H···I interactions are represented as broken lines. Displacement ellipsoids are drawn at the 50% probability level.

3.2 Biphenyl-4,4'-diyl-bis(2,2,5,5-tetramethyl-1-oxyl-3-pyrroline-3-carboxylate)

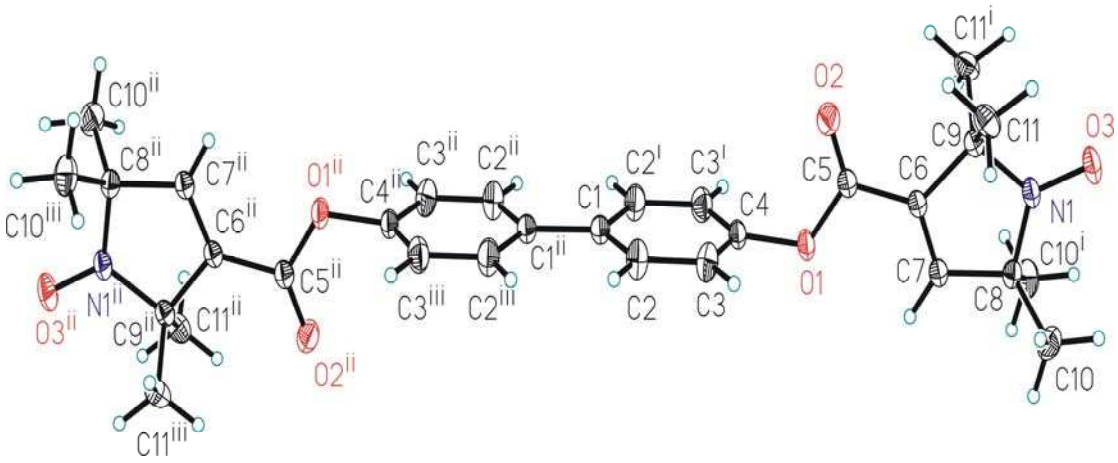

***Figure 4*:** Structure of **16** shown with 50% probability displacement ellipsoids. The H atoms are drawn as small spheres with arbitrary radii. Symmetry equivalent atoms (marked with index *i*) are related by a) *x*, *-y*, *z*, b) *–x,-y,1*, c) *2 - x*, *y*, *1 – z*.

The crystal structure of **16**[91] is depicted in Figure 4 the complete molecule is generated by a crystallographic 2/m symmetry operation: atoms C1, C4, O1, C5, O2, C6, C7, C8, C9, N1 and O3 lie on a mirror plane. There is a twofold symmetry axis perpendicular to this mirror plane and passing through the center of the central C-C single bond. Also, an inversion center exists at the midpoint of the central C-C single bond. The two six-membered rings of the biphenyl group are coplanar meaning that the dihedral angle between the ring planes of the biphenyl fragment is constrained by symmetry to be zero, resulting in rather short intramolecular H···H contact distances of 2.02 Å. The 1-oxyl-3-pyrroline-3-carboxylate group is planar. Approximate planarity of this group has been observed in a number of related crystal structures.[85,92,93,94,95,96]

In the crystal (see Figure 5), molecules are connected along the a-axis direction by very weak intermolecular methyl–phenyl C–H···π interactions. The C-H bond is not directed to the center of the benzene ring, but mainly to one C atom [C-H···C(*x - 1*, *y*, *z*): H···C = 2.91 A and C-H···C = 143°].

The H atoms were positioned geometrically and treated as riding: C_{methyl}-H = 0.98 Å, C_{planar}-H = 0.95 Å, $U_{iso}(H) = 1.2\ U_{eq}(C_{non\text{-}methyl})$ and $U_{iso}(H) = 1.5\ U_{eq}(C_{methyl})$. The torsion angles about the C-C_{methyl} bonds were refined for the methyl groups. Single crystals were obtained by recrystallization from a mixture of toluene and n-hexane (3:1).

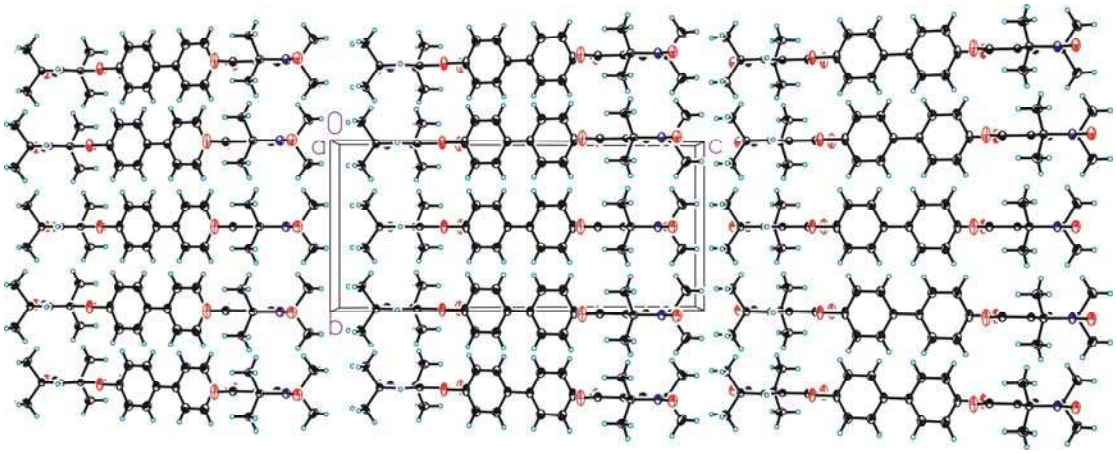

***Figure 5*:** Crystal Packing viewed down the a axis.

4. EPR Primer

Electron Paramagnetic Resonance (EPR) experiments take advantage of manipulating a sample's macroscopic magnetization. Spins may be electron spins ("*dipolar spectroscopy"*) or nuclear and electron spins ("*hyperfine spectroscopy"*) The origin of this macroscopic magnetization in the presence as well as absence of an external magnetic field following standard text books of magnetic resonance[11,97,98,99] will be discussed within this chapter.

4.1 An Electron in a Magnetic Field

In a fundamental experiment performed at the Institute of Physics at Goethe-University Frankfurt Stern and Gerlach observed a splitting of an Ag^+-beam into two discrete states in an inhomogeneous magnetic field.[100,101] As the single unpaired electron is located in a *s*-orbital (l = 0), the interaction of the silver ion's magnetic moment with the applied external magnetic field cannot be attributed to orbital angular momentum. An intrinsic angular momentum of the electron, $\hat{\vec{s}}$, the so called *electron spin*, was introduced to take the experimental effects into account. Deduced from classical physics any particle with a charge q, mass m and angular momentum s causes a magnetic moment $\vec{\mu} = \frac{q}{2m}\vec{s}$. In quantum mechanics the magnetic moment of a free electron, $\vec{\mu}_e$ is described by a similar expression:

$$\hat{\vec{\mu}}_e = -g_e \frac{e}{2m_e}\hat{\vec{s}} \qquad \text{(eq. 1)}$$

with $\hat{\vec{s}} = \hbar \begin{pmatrix} \hat{S}_x \\ \hat{S}_y \\ \hat{S}_z \end{pmatrix} = \hbar\hat{\vec{S}}$ and $\hat{S}_x = \frac{1}{2}\begin{pmatrix} 0 & 1 \\ 1 & 0 \end{pmatrix}, \hat{S}_y = \frac{1}{2}\begin{pmatrix} 0 & -i \\ i & 0 \end{pmatrix}, \hat{S}_z = \frac{1}{2}\begin{pmatrix} 1 & 0 \\ 0 & -1 \end{pmatrix}$

Eq. 1 contains the electron charge e, the electron mass m_e and an additional factor g_e, which is called g-factor of electron. According to the Dirac Equation the value of g_e is exactly equal to 2. Precise quantum electrodynamics calculations yield a slightly

different value g_e = 2.0023193043737(82) arising from the electrons interaction with virtual photons. The notion $\hat{\vec{s}}$ in eq. 1 corresponds to the electron spin operator which is expressed via the Pauli matrixes $\hat{S}_x, \hat{S}_y, \hat{S}_z$. $\hbar$ is the Planck constant, *h*, divided by 2π. In this terms the value of magnetic moment can be written as:

$\hat{\vec{\mu}}_e = -g_e \beta_e \hat{\vec{S}}$ where $\beta_e = \frac{e\hbar}{2m_e}$ is the Bohr magneton. (eq. 2)

Keeping in mind that the energy *E* of a magnetic moment $\vec{\mu}$ in an external magnetic field $\vec{B}_0$ can be expressed as:

$$E = -\vec{\mu} \cdot \vec{B}_0 \quad \text{(eq. 3)}$$

and substituting eq. 2 into eq. 3 the Hamilton operator of a free electron in a magnetic field is:

$\hat{H} = g_e \cdot \beta_e \cdot \hat{\vec{S}} \cdot \vec{B}_0$ with: $\vec{B}_0 = (B_x, B_y, B_z)$. (eq. 4)

If the magnetic field in laboratory axis system is applied along the z-axis of the Cartesian coordinate system, $\vec{B}_0 = (0, 0, B_0)$ and eq. 4 simplifies to:

$$\hat{H} = g_e \cdot \beta_e \cdot \hat{S}_z \cdot \left|\vec{B}_0\right| \quad \text{(eq. 5)}$$

and two energy eigenvalues result:

$E_1 = \frac{1}{2} g_e \beta_e \left|\vec{B}_0\right|$ (eq. 6) and $E_2 = -\frac{1}{2} g_e \beta_e \left|\vec{B}_0\right|$ (eq. 7)

Eq. 7 and 8 are often stated as:

$$E = m_S g_e \beta_e \vec{B}_0 \text{ with } m_S = \pm\frac{1}{2} \qquad \text{(eq. 8)}$$

m_S, the magnetic quantum number, is the *z*-component of the electron spin. This splitting of energy levels in an external magnetic field is referred to as the *electron Zeeman splitting* (*EZ*). It is linearly depending on the magnetic field. A resonance transition between these two states is induced according to the rules of selection in case $\Delta m_S = \pm 1$ upon irradiation, *hν*, matching the energy difference ΔE. This frequency is referred to as the *Lamor frequency*.

$$\Delta E = h\nu = \hbar\omega = E_2 - E_1 = g_e \beta_e \left|\vec{B}_0\right| \qquad \text{(eq. 9)}$$

4.2 Spin Interactions and the Spin Hamiltonian

The above considerations are valid regarding an electron isolated from other particles. Considering a bound electron the *g*-value will deviate due to a manifold of electrostatic and magnetic interactions. Moreover, orientation dependent (anisotropic) effects have to be taken into account. Abragam and Pryce[102,103] introduced the static Spin Hamilton Operator containing elements describing the interaction of the electron and nuclear spins with the external magnetic field as well as the magnetic dipole interaction of electrons spins (*A* and *B*) and the interaction between nuclei and electrons spins. Only terms relevant in the course of this work are stated, meaning that nuclear quadrupole interaction and zero field splitting are omitted.

$$\hat{H} = \underbrace{\beta_e \vec{\hat{S}}_A \cdot \vec{\vec{g}}_A \cdot \vec{B}_0 + \beta_e \vec{\hat{S}}_B \cdot \vec{\vec{g}}_B \cdot \vec{B}_0}_{EZ} \underbrace{- g_{IA}\beta_I \vec{B}_0 \cdot \vec{\hat{I}}_A - g_{IB}\beta_I \vec{B}_0 \cdot \vec{\hat{I}}_B}_{NZ} + \underbrace{\vec{\hat{S}}_A \cdot \vec{\vec{A}} \cdot \vec{\hat{I}}_A + \vec{\hat{S}}_B \cdot \vec{\vec{A}} \cdot \vec{\hat{I}}_B}_{HF}$$
$$+ \underbrace{\vec{\hat{S}}_A \cdot \vec{\vec{D}} \cdot \vec{\hat{S}}_B}_{DD} + \underbrace{J\ \vec{\hat{S}}_A \cdot \vec{\hat{S}}_B}_{EXCH} \qquad \text{(eq. 10)}$$

Here, *EZ* abbreviates the electron Zeeman interaction, *NZ* the nuclear Zeeman interaction, *HF* the hyperfine interaction, *EXCH* the exchange interaction and *DD* the dipole-dipole interaction. *EXCH* and *DD* have to be treated in case of more than one

unpaired coupled electron. The first three terms will be discussed in more detail in the following section and the last two terms in Section 4.6 and 4.7.

4.3 The Electron Zeeman Interaction

The electron Zeeman interaction depends linearly on the Cartesian spin operator and on the magnetic field. In the laboratory coordinate system, where $\vec{B}_0 = (0,0,B_0)$, it is given by:

$$\hat{H}_{EZ} = \beta_e \hat{\vec{S}} \cdot \vec{\vec{g}}^{\,L} \cdot \vec{B}_0 \text{ with } \vec{\vec{g}}^{\,L} = \begin{pmatrix} g_{xx}^{\ L} & g_{xy}^{\ L} & g_{xz}^{\ L} \\ g_{yx}^{\ L} & g_{yy}^{\ L} & g_{yz}^{\ L} \\ g_{zx}^{\ L} & g_{zy}^{\ L} & g_{zz}^{\ L} \end{pmatrix} \qquad \text{(eq. 11)}$$

$\Rightarrow$

$$\hat{H}_{EZ} = \beta_e \left|\vec{B}_0\right| (g_{xz}^L \hat{S}_x + g_{yz}^L \hat{S}_y + g_{zz}^L \hat{S}_z)$$

Any information regarding the orientation dependence of the electron Zeeman interaction is expressed in terms of the *g*-matrix, $\vec{\vec{g}}^{\,L}$ in laboratory coordinate system. Usually the *g*-tensor is known in the *principal axes system* (PAS), where it is diagonal

$$\vec{\vec{g}} = \begin{pmatrix} g_{xx} & 0 & 0 \\ 0 & g_{yy} & 0 \\ 0 & 0 & g_{zz} \end{pmatrix} \qquad \text{(eq. 12)}$$

The laboratory coordinate frame is transformed in the PAS via a rotation matrix ***R*** depending on the Euler angles Ω.

$$\vec{\vec{g}}^{\,L} = R^{-1}(\Omega)\vec{\vec{g}}R(\Omega) \text{ with } \Omega(\alpha,\beta,\gamma) \qquad \text{(eq. 13)}$$

It yields:

$$g_{xz}^L = g_{xx}\cos\alpha\sin\beta,\ g_{yz}^L = g_{yy}\sin\alpha\sin\beta,\ g_{zz}^L = g_{zz}\cos\beta \qquad \text{(eq. 14)}$$

Using eq. 14 one can transform eq. 11 to:

$$\hat{H}_{EZ} = \beta_e B_0 \left(g_{xx} \cos\alpha \sin\beta \hat{S}_x + g_{yy} \sin\alpha \sin\hat{S}_y + g_{zz} \cos\beta \hat{S}_z \right)$$

and after digitalization the electron Zeeman Hamilton operator is:

$$\hat{H}_{EZ} = \beta_e g_{eff} \left| \vec{B}_0 \right| \hat{S}_z \qquad \text{(eq. 15)}$$

with $g_{eff} = \sqrt{(g_{xx} \cos\alpha \sin\beta)^2 + (g_{yy} \sin\alpha \sin\beta)^2 + (g_{zz} \cos\beta)^2}$ as the effective *g*-value. This equation may be interpreted geometrically as an ellipsoid with the three axes g_{xx}, g_{yy} and g_{zz} in which g_{eff} is a vector from the origin to the surface. Eq. 15 lays the base to derive orientation dependent resonance frequencies in one of the author's publications.[104]

If the molecule is tumbling fast versus the inverse applied microwave frequency or in the absence of an external magnetic field only the isotropic part of the *g*-matrix is of concern. In general, the isotropic part of a tensor is given by the trace of the matrix.

$$g_{iso} = \frac{g_{xx} + g_{yy} + g_{zz}}{3} = \frac{1}{3} \boldsymbol{Tr}(\vec{\vec{g}}) \qquad \text{(eq. 16)}$$

This equation is independent of the coordinate system representing the tensor as a matrix.

4.4 The Nuclear Zeeman Interaction

In most EPR experiments the nuclear Zeeman Hamilton operator is not effecting the allowed transitions ($\Delta m_S = \pm 1$, $\Delta m_I = 0$), as it causes an equal shift of the energy levels. This approximation is valid if the Electron Zeeman interaction is much larger compared to the hyperfine interaction (*high field approximation*). It can be described in analogy to the electron Zeeman interaction (see above) with exception to the sign of the *g*-value. It has to be opposite to the, as commonly defined, positive *g*-value of the negatively charged electron due to the positive charge of the nucleus. Anisotropic effects can be neglected, because they are usually smaller than the line width.

$$\hat{H}_{NZ} = -g_I \beta_I \cdot \vec{B}_0 \cdot \vec{\hat{I}} \qquad \text{(eq. 17)}$$

g_I states the nuclear g-factor, β_I the nuclear magneton and $\vec{\hat{I}}$ the nuclear spin operator.

4.5 The Hyperfine Interaction

The nuclear spin as well as the electron spin possesses a magnetic moment. Therefore, a distance dependent dipole-dipole interaction between the two exists - the anisotropic part of the hyperfine interaction. Moreover, an isotropic part of the hyperfine interaction namely the Fermi contact interaction has to be treated. Nevertheless, owing to the smaller magnetic moment of the nuclear spin with respect to the electron spin the overall distance dependent interaction usually takes place in a smaller range compared to two dipolar coupled electrons (see Section 4.7).

$$\hat{H}_{HF,aniso} = \vec{\hat{S}} \cdot \vec{\vec{T}} \cdot \vec{\hat{I}} \qquad \text{(eq. 18)}$$

$\vec{\vec{T}}$ is the traceless dipolar coupling tensor describing the interaction of the nuclear spin with the magnetic moment of the electron spin neglecting spin orbit coupling. It is correlated to the interconnecting electron nucleus distance vector in the PAS which e.g. allows to localize protons in the vicinity of an unpaired electron. Introduction of spin orbit coupling alters the dipolar hyperfine interaction to:

$$\vec{\vec{A}}_{dip} = \frac{\vec{\vec{g}} \cdot \vec{\vec{T}}}{g_e} \qquad \text{(eq. 19)}$$

giving the overall anisotropic contribution to the hyperfine interaction. In a spherically symmetric *s*-orbital one would expect the dipole-dipole interaction to average to zero (see Section 4.7). As electrons do have a defined spatial probability at the nucleus ($|\Psi_0(r=0)|^2 > 0$) an isotropic part, the Fermi contact interaction has to be included:

$$A_{iso} = \frac{2}{3}\frac{\mu_0}{\hbar} g_e \beta_e \beta_I |\Psi_0(r=0)|^2 \qquad \text{(eq. 20)}$$

Here, μ_0 is the vacuum permeability and the overall hyperfine interaction treating isotropic and anisotropic contributions can be written as:

$$\hat{H}_{HF} = \vec{\hat{S}} \cdot \vec{\vec{A}} \cdot \vec{\hat{I}} \text{ with } \vec{\vec{A}} = A_{iso}\vec{\vec{1}}_3 + \frac{\vec{\vec{g}} \cdot \vec{\vec{T}}}{g_e} \qquad \text{(eq. 21)}$$

$\vec{\vec{1}}_3$ is a (3 x 3) unit matrix and A_{iso} is given as:

$$A_{iso} = \frac{1}{3}(A_{xx} + A_{yy} + A_{zz}) = \frac{1}{3}\boldsymbol{Tr}(\vec{\vec{A}}) \qquad \text{(eq. 22)}$$

Figure 6 illustrates the influence of the isotropic and anisotropic part of the ^{14}N-hyperfine interaction on a nitroxide spectrum depending on temperature at X-band frequency. At room temperature, in the fast tumbling regime only the isotropic part needs to be considered, whereas at low temperatures anisotropy has be treated.

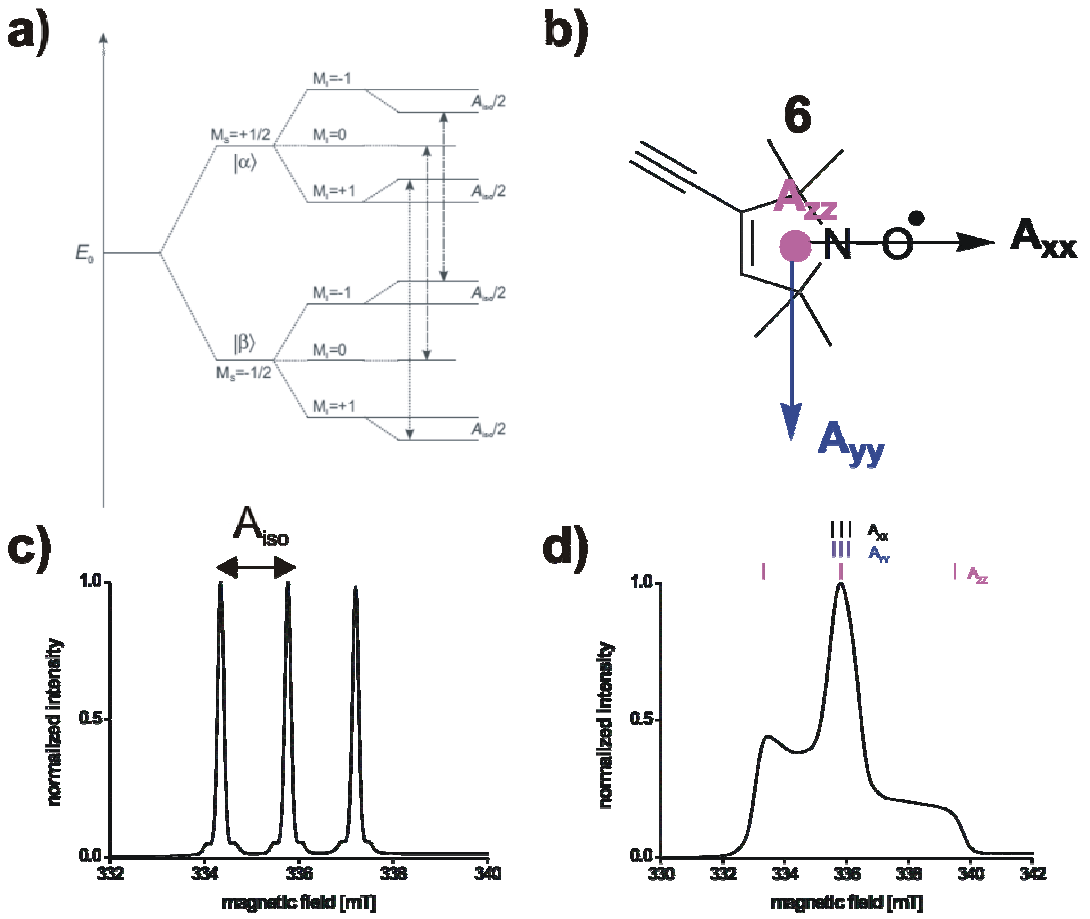

***Figure 6*:** a) schematic energy level diagram for a S = ½ and I = 1 species, e.g. a nitroxide; b) nitroxide **6** with the molecular axis system indicated; c) isotropic cw-X-band EPR spectrum of **6** recorded at room temperature, additional small lines are ^{13}C-satellites in natural abundance; d) anisotropic cw-X-band EPR spectrum of **6** recorded at 70K and the corresponding ^{14}N stick spectrum.

4.6 Electron-Electron Interactions

In EPR spectroscopy the electron-electron magnetic dipole interactions allow for determination of the distance between the spin bearing units and thus gain insight to molecular structure. The following section treats the theoretical aspects of dipolar spectroscopy laying the base to experiments performed in the publications of the author. It will discuss unpaired electrons in weakly overlapping orbitals meaning that it is more convenient to describe the system to consist of individual spins instead of introducing a group spin. These interactions will contain a dipolar contribution (see Section 4.7) as well as a contribution resulting from lifting the degeneracy of the parallel and anti-parallel spin state of the electrons (see Section 4.8).

4.6.1 The Dipole-Dipole Interaction

This section discusses the electron-electron dipole-dipole interaction based on standard text books of magnetic resonance.[105,106] In classical physics the energy of two interacting dipoles A and B connected by a vector $\vec{r}$ is:

$$E = \frac{\mu_0}{4\pi}\left(\frac{\vec{\mu}_A \cdot \vec{\mu}_B}{\vec{r}^3} - \frac{3(\vec{\mu}_A \cdot \vec{r})(\vec{\mu}_B \cdot \vec{r})}{\vec{r}^5}\right) \qquad \text{(eq. 23)}$$

Conversion to a compact quantum mechanical spin Hamiltonian in angular frequency units is achieved assuming only a slightly anisotropic *g*-matrix and the point dipole approximation[107] of the electrons and via usage of the correspondence principle (see eq. 2):

$$\hat{H}_{DD} = \frac{\mu_0}{4\pi\hbar}\left(\frac{(-g_{eff}^A \beta_e \hat{\vec{S}}_A)\cdot(-g_{eff}^B \beta_e \hat{\vec{S}}_B)}{\vec{r}^3} - \frac{3(-g_{eff}^A \beta_e \hat{\vec{S}}_A \cdot \vec{r})(-g_{eff}^B \beta_e \hat{\vec{S}}_B \cdot \vec{r})}{\vec{r}^5}\right)$$
$$\hat{H}_{DD} = -\frac{\mu_0 \cdot g_{eff}^A \cdot g_{eff}^B \cdot \beta_e^2}{4\pi\hbar}\left(\frac{\hat{\vec{S}}_A \hat{\vec{S}}_B}{\vec{r}^3} - \frac{3(\hat{\vec{S}}_A \cdot \vec{r})(\hat{\vec{S}}_B \cdot \vec{r})}{\vec{r}^5}\right) = \hat{\vec{S}}_A \vec{\vec{D}} \hat{\vec{S}}_B \qquad \text{(eq. 24)}$$

Eq. 24 is commonly stated by means of spherical coordinates θ, φ and *r*, representing the orientation of the molecule with respect to the external magnetic field as:

$$\hat{H}_{DD} = \frac{\mu_0}{4\pi\hbar}\frac{g_{eff}^A g_{eff}^B \beta_e^2}{\vec{r}^3}\left(A + B + C + D + E + F\right)$$
$$A = \hat{S}_z^A \hat{S}_z^B \left(1 - 3\cos^2\theta_{dip}\right)$$
$$B = \frac{1}{4}\left(\hat{S}_+^A \hat{S}_-^B + \hat{S}_-^A \hat{S}_+^B\right)\left(1 - 3\cos^2\theta_{dip}\right)$$
$$C = -\frac{3}{2}\left(\hat{S}_+^A \hat{S}_z^B + \hat{S}_z^A \hat{S}_+^B\right)\sin\theta_{dip}\cos\theta \cdot e^{-i\varphi} \qquad \text{(eq. 25)}$$
$$D = -\frac{3}{2}\left(S_-^A S_z^B + S_z^A S_-^B\right)\sin\theta_{dip}\cos\theta_{dip} \cdot e^{i\varphi}$$
$$E = -\frac{3}{4}\hat{S}_+^A \hat{S}_+^B \sin^2\theta_{dip} \cdot e^{-2i\varphi}$$
$$F = -\frac{3}{4}\hat{S}_-^A \hat{S}_-^B \sin^2\theta_{dip} \cdot e^{2i\varphi}$$

with the raising operator $\hat{S}_+$ and the lowering operator $\hat{S}_-$:

$$\hat{S}_+ = \hat{S}_x + i\hat{S}_y$$
$$\hat{S}_- = \hat{S}_x - i\hat{S}_y$$

either raising or lowering the magnetic quantum number by 1.

The terms *A* - *F* are ordered in a way reflecting their influence on the magnetic quantum number $M = m_S^A + m_S^B$. Terms *A* and *B* correspond to $\Delta M = 0$, *C* to $\Delta M = +1$, *D* to $\Delta M = -1$, E to $\Delta M = +2$, and F to $\Delta M = -2$. Note that *E* and *F* are forbidden transitions. In case the spins are quantized along the direction of the external magnetic field only terms *A* and *B* have to be treated.

$$\hat{H}_{DD} = \frac{\mu_0}{4\pi\hbar}\frac{g_{eff}^A g_{eff}^B \beta_e^2}{\vec{r}^3}\left(A + B\right)$$
$$\hat{H}_{DD} = \frac{\mu_0}{4\pi\hbar}\frac{g_{eff}^A g_{eff}^B \beta_e^2}{\vec{r}^3}\left(\hat{S}_z^A \hat{S}_z^B + \frac{1}{4}\left(\hat{S}_+^A \hat{S}_-^B + \hat{S}_-^A \hat{S}_+^B\right)\right)\left(1 - 3\cos^2\theta_{dip}\right) \qquad \text{(eq. 26)}$$
$$\hat{H}_{DD} = \omega_{dip}\left(\hat{S}_z^A \hat{S}_z^B + \frac{1}{4}\left(\hat{S}_+^A \hat{S}_-^B + \hat{S}_-^A \hat{S}_+^B\right)\right)$$

with:

$$\omega_{dip} = \frac{\mu_0 g_{eff}^A g_{eff}^B \beta_e^2}{4\pi\hbar} \frac{1}{r^3}\left(1-3\cos^2\theta_{dip}\right) = 2\pi\nu_{dip} = \frac{D_{dip}}{r^3}\left(1-3\cos^2\theta_{dip}\right) \qquad \text{(eq. 27)}$$

If, in addition, the dipolar coupling is small compared to the difference in Lamor frequencies of the two spins (*weak coupling limit*) only the diagonal elements of $\hat{H}_{dip}$ need to be taken into account (*secular approximation*).

This leads to the four energy levels $\varepsilon_1 = \frac{1}{4}\omega_{dip}$, $\varepsilon_2 = -\frac{1}{4}\omega_{dip}$, $\varepsilon_2 = -\frac{1}{4}\omega_{dip}$ and $\varepsilon_4 = \frac{1}{4}\omega_{dip}$:

$$\hat{H}_{DD} = \begin{pmatrix} +\frac{1}{4}\omega_{dip} & & & 0 \\ & -\frac{1}{4}\omega_{dip} & & \\ & & -\frac{1}{4}\omega_{dip} & \\ 0 & & & +\frac{1}{4}\omega_{dip} \end{pmatrix} \rightarrow \begin{matrix} \varepsilon_1 = +\frac{1}{4}\omega_{dip} \\ \varepsilon_2 = -\frac{1}{4}\omega_{dip} \\ \varepsilon_3 = -\frac{1}{4}\omega_{dip} \\ \varepsilon_4 = +\frac{1}{4}\omega_{dip} \end{matrix} \qquad \text{(eq. 28)}$$

For allowed EPR transitions the dipolar contribution is thus:

$$\begin{aligned} \varepsilon_1 - \varepsilon_3 = \varepsilon_1 - \varepsilon_2 = +\frac{1}{2}\omega_{dip} \\ \varepsilon_2 - \varepsilon_4 = \varepsilon_3 - \varepsilon_4 = -\frac{1}{2}\omega_{dip} \end{aligned} \qquad \text{(eq. 29)}$$

Therefore, a pair of doublets split by $\left|\omega_{dip}\right|$ appears in the spectrum only taking into account dipolar coupling.

As eq. 27 is assuming a quantization of the magnetic dipoles parallel to the external magnetic field $\vec{B}_{0,z}$, θ_{dip} describes the angle between the spin-spin distance vector *r*

and $\vec{B}_{0,z}$. Eq. 27 can also be rewritten as a second order Legendre polynomial whose integral over the unit sphere vanishes demonstrating that the dipolar interaction will average to zero for molecules rotating fast compared to the inverse coupling strength. In case of slowly rotating molecules or frozen solutions three extreme values are to be regarded. For θ_{dip} equals 54.7° (so called *magic angle*) $\omega_{dip} = 0$. Moreover, ω_{dip} will vary from $-2\frac{D_{dip}}{r^3}$ to $+1\frac{D_{dip}}{r^3}$ for the extreme values of θ = 180° and 0°, respectively. The resulting spectrum of such *randomly oriented molecules* is named *Pake pattern* and shown in Figure 7.

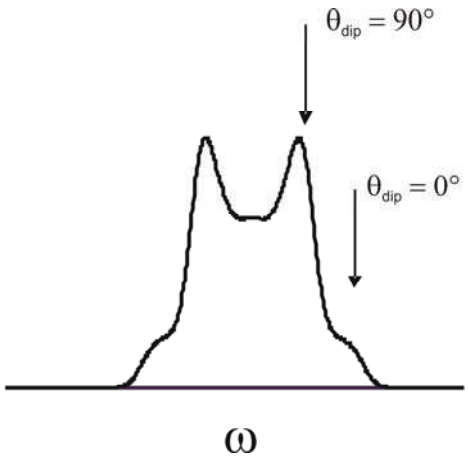

***Figure 7*:** Pake pattern. Arrows indicate the most prominent observables θ_{dip} = 90° and θ_{dip} = 0°. For J = 0 the splitting between the two peaks is $\omega_{dip}\left(\theta_{dip} = 0°\right)$ and between the two edges $\omega_{dip}\left(\theta_{dip} = 0°\right) = 2\omega_{dip}\left(\theta_{dip} = 90°\right)$. In case of pulsed EPR experiments like PELDOR the peaks appear at $\pm\omega_{dip}$ and $\pm 2\omega_{dip}$.

4.6.2 The Exchange Interaction

A simple expression for the exchange interaction *J* between two open-shell molecules in terms of the SOMO-SOMO interactions following the work of Hoffmann[108] is obtained. Generally, two electrons in weakly overlapping orbitals may either be arranged in a parallel (triplet state) or anti-parallel (singlet state) manner. Note that according to the definition of the Heisenberg-Dirac-van Vleck-Hamiltonian in eq. 10:

$$\hat{H}_{Exch} = J \cdot \vec{\hat{S}}_A \cdot \vec{\hat{S}}_B \qquad \text{(eq. 30)}$$

a positive value of *J* indicates an *antiferromagnetic coupling*, representing a singlet ground state, whereas a negative value (*ferromagnetic coupling*) reflects a triplet ground state. Assuming a small overlap of the SOMOs Φ_a and Φ_b as well as the Wolfsberg-Helmholtz relation in extended Hückel theory[109] the energy separation between the singlet state and the triplet state being equal to *J* can be written as:

$${}^1\mathrm{E} - {}^3\mathrm{E} = J = -5\left(h_{aa} + h_{bb}\right)S_{ab}^2 + 2\left(aa \mid bb\right) - 2\left(ab \mid ba\right) \qquad \text{(eq. 31)}$$

with:

$$h_{aa} = \int \Phi_a^*(1)\hat{h}\Phi_a(1)d\tau_1$$

$$h_{bb} = \int \Phi_b^*(1)\hat{h}\Phi_b(1)d\tau_1$$

$$S_{ab} = \int \Phi_a^*\Phi_b d\tau$$

$$\left(aa \mid bb\right) = \iint \Phi_a^*(1)\Phi_a(1)\frac{1}{r}\Phi_b^*(2)\Phi_b(2)d\tau_1 d\tau_2$$

$$\left(ab \mid ba\right) = \iint \Phi_a^*(1)\Phi_b(1)\frac{1}{r}\Phi_b^*(2)\Phi_a(2)d\tau_1 d\tau_2$$

Here, $\hat{h}$ is the one electron Hamilton operator, S_{ab} the overlap integral between Φ_a and Φ_b, $\left(aa \mid bb\right)$ the Coulomb integral, *r* the distance between the two electrons and $\left(ab \mid ba\right)$ the two electron exchange integral. As h_{aa} and h_{bb} are negative and the overlap and Coulomb integral are positive by definition, the first and second term in eq. 31 are positive thus favoring antiferromagnetic coupling. However, the negative

third term accounts for net ferromagnetic coupling. In consequence a ferromagnetic coupling is preferred if the overlap between the SOMOs is small and a singlet state will prevail for a large orbital overlap. Molecular geometric preconditions altering orbital overlap to either stabilize a singlet or triplet ground state are extensively discussed in literature[110]. Moreover, according to standard text books of physical chemistry the overlap of wave functions exponentially decreases depending on the distance between the two electrons, *r*, and therefore *J* is also exponentially dependent on *r*. Hence, *J* decreases faster upon increasing *r* than ω_{dip} which decays with $\frac{1}{r^3}$. At sufficiently large *r* values the dipole-dipole interaction will dominate the coupling of two electron spins. Nevertheless, *J* is purely isotropic and simply the sum of both ferromagnetic and antiferromagnetic contributions:

$$J = J_f + J_{af} \qquad \text{(eq. 32)}$$

This coupling may either be mediated via a direct overlap of the SOMOs (*through space interaction*) or via chemical bonds in a delocalized system (*through bond interaction*). Instead of a delocalization, one unpaired electron may polarize a neighboring paired electron increasing its spin density resulting in a favored alignment of the second unpaired spin. This *spin polarization* mechanism is also a through bond interaction. Both through space and through bond interaction may each have a ferromagnetic and an antiferromagnetic component.

In order to yield the eigenstates of $\hat{H}_{Exch}$ eq. 30 can be stated as:

$$\hat{H}_{Exch} = J \cdot \vec{\hat{S}}_A \cdot \vec{\hat{S}}_B = J\left(\hat{S}_x^A \hat{S}_x^B + \hat{S}_y^A \hat{S}_y^B + \hat{S}_z^A \hat{S}_z^B\right)$$
$$\hat{H}_{Exch} = J\hat{S}_z^A \hat{S}_z^B + \frac{1}{2} J\left(\hat{S}_+^A \hat{S}_-^B + \hat{S}_-^A \hat{S}_+^B\right) \qquad \text{(eq. 33)}$$

Within the weak coupling limit the resulting eigenstates are expressed in analogy to eq. 26-29:

$$\hat{H}_{Exch} = \begin{pmatrix} +\frac{1}{4}J & 0 & & \\ & -\frac{1}{4}J & & \\ & & -\frac{1}{4}J & \\ 0 & & & +\frac{1}{4}J \end{pmatrix} \rightarrow \begin{matrix} \varepsilon_1 = +\frac{1}{4}J \\ \varepsilon_2 = -\frac{1}{4}J \\ \varepsilon_3 = -\frac{1}{4}J \\ \varepsilon_4 = +\frac{1}{4}J \end{matrix} \qquad \text{(eq. 34)}$$

and

$$\begin{aligned} \varepsilon_1 - \varepsilon_3 = \varepsilon_1 - \varepsilon_2 = +\frac{1}{2}J \\ \varepsilon_2 - \varepsilon_4 = \varepsilon_3 - \varepsilon_4 = -\frac{1}{2}J \end{aligned} \qquad \text{(eq. 35)}$$

This gives rise to calculating the overall electron-electron contribution to the EPR transition frequencies as described in the next section.

4.6.3 The overall Electron-Electron Interaction

This section describes the overall electron-electron contribution to EPR frequencies for a pair of coupled spin one-half system. For reason of simplification the nuclear Zeeman and hyperfine interactions are omitted and only the electron Zeeman, dipolar and exchange interaction are considered within the high-field approximation in the weak coupling limit. A more precise definition is to state that the off-diagonal elements are much smaller than the difference in Lamor frequencies: $\left|J-\frac{1}{2}\omega_{dip}\right| \ll \left|\omega_A-\omega_B\right|$.

$$\hat{H} = \hat{H}_{EZ} + \hat{H}_{Exch} + \hat{H}_{DD} \qquad \text{(eq. 36)}$$

with :

$$\hat{H}_{EZ} = \begin{pmatrix} +(\omega_A+\omega_B) & & & 0 \\ & +(\omega_A-\omega_B) & & \\ & & -(\omega_A-\omega_B) & \\ 0 & & & -(\omega_A+\omega_B) \end{pmatrix}$$

$$\hat{H}_{Exch} = \begin{pmatrix} +\frac{1}{4}J & & & 0 \\ & -\frac{1}{4}J & & \\ & & -\frac{1}{4}J & \\ 0 & & & +\frac{1}{4}J \end{pmatrix} \text{ and } \hat{H}_{DD} = \begin{pmatrix} +\frac{1}{4}\omega_{dip} & & & 0 \\ & -\frac{1}{4}\omega_{dip} & & \\ & & -\frac{1}{4}\omega_{dip} & \\ 0 & & & +\frac{1}{4}\omega_{dip} \end{pmatrix}.$$

Leading to:

$$\begin{aligned}
\varepsilon_1 &= +\frac{1}{2}(\omega_A + \omega_B) + \frac{1}{4}(J + \omega_{dip}) \quad \downarrow\downarrow \\
\varepsilon_2 &= +\frac{1}{2}(\omega_A - \omega_B) - \frac{1}{4}(J + \omega_{dip}) \quad \uparrow\downarrow \\
\varepsilon_3 &= -\frac{1}{2}(\omega_A - \omega_B) - \frac{1}{4}(J + \omega_{dip}) \quad \downarrow\uparrow \\
\varepsilon_4 &= -\frac{1}{2}(\omega_A + \omega_B) + \frac{1}{4}(J + \omega_{dip}) \quad \uparrow\uparrow
\end{aligned} \qquad \text{(eq. 37)}$$

For the electron Zeeman interaction in its matrix representation concerning a two spin system see above stated standard text books of magnetic resonance.

The frequencies of the resulting EPR transitions are therefore:

$$\begin{aligned}
\varepsilon_1 - \varepsilon_3 &= +\omega_A + \frac{1}{2}(J + \omega_{dip}) & \varepsilon_1 - \varepsilon_2 &= +\omega_B + \frac{1}{2}(J + \omega_{dip}) \\
\varepsilon_2 - \varepsilon_4 &= +\omega_A - \frac{1}{2}(J + \omega_{dip}) & \varepsilon_3 - \varepsilon_4 &= +\omega_B - \frac{1}{2}(J + \omega_{dip})
\end{aligned} \qquad \text{(eq. 38)}$$

The resulting spectrum thus comprises a pair of doublets, centered at ω_A and ω_B with the total splitting $|\omega_{AB}|$:

$$\omega_{AB} = \omega_{dip} + J = \frac{\mu_0 g_{eff}^A g_{eff}^B \beta_e^2}{4\pi\hbar}\frac{1}{r^3}(1 - 3\cos^2\theta_{dip}) + J = 2\pi\nu_{dip} + J = \frac{D_{dip}}{r^3}(1 - 3\cos^2\theta_{dip}) + J$$

(eq. 39)

By monitoring a distance or change in distance conclusion concerning molecular structure may be obtained. Unfortunately, the dipolar splitting ω_{AB} for distances of above 1.5 nm is often covered within the inhomogeneous line width of the investigated system. One pulsed EPR method capable of revealing the electron-electron interaction ω_{AB} and additionally disentangling J and ω_{dip}, PELDOR will be discussed in detail in the next chapter. Determination of ω_{AB} allows for a parameter

free straightforward determination of the distance vector connecting the spin centers. Figure 7 illustrates the easy applicability of eq. 39 regarding distance determination.

E. g for a pair of radicals with $g_A = g_B = 2.005$ and $J = 0$ it follows for a PELDOR experiment:

$$\left|\nu\left(\theta_{dip} = 90°\right)\right| = \frac{52.18}{r^3[\text{nm}]} \qquad \text{(eq. 40)}$$

or:

$$r\ [\text{nm}] = \sqrt[3]{\frac{52.18}{\left|\nu\left(\theta_{dip} = 90°\right)\right|}} \qquad \text{(eq. 41)}$$

Note that in case of pulsed EPR experiments like PELDOR the singularities of the Pake pattern appear at $\pm\omega_{dip}$ and $\pm 2\omega_{dip}$.

5. Pulsed Electron-Electron Double Resonance Primer

PELDOR[27,46] is a powerful tool to measure distances between paramagnetic centers in the nanometer range.[42] The method has been widely applied[12,14,30,31,32,33,34] to determine distances in spin labeled macromolecules such as polymers and biomolecules. Not only the distance, but also the orientation of the two dipoles with respect to the interconnecting distance vector *r* between the two radical centers affects the coupling strength. Nitroxides, which are commonly used as spin labels, typically have a large rotational and conformational freedom. Therefore, in most studies the relative orientation has been considered as random, leading to the well known Pake pattern distribution of dipolar coupling strengths (see Figure 7). In such cases the most prominent coupling strength corresponds to an orientation where the *r*-vector is perpendicular to the external magnetic field. The frequency resulting from the perpendicular orientation of the *r*-vector with respect to the external magnetic field is usually chosen in order to extract the distance between the two radicals. Observation of the full Pake pattern by a 4-pulse PELDOR sequence[111,112](see Figure 8) enables to disentangle the orientation dependent dipolar coupling $D_{dip}(\theta)$ from the isotropic exchange coupling *J* which additionally may usually occur for distances smaller than 2 nm.[44]

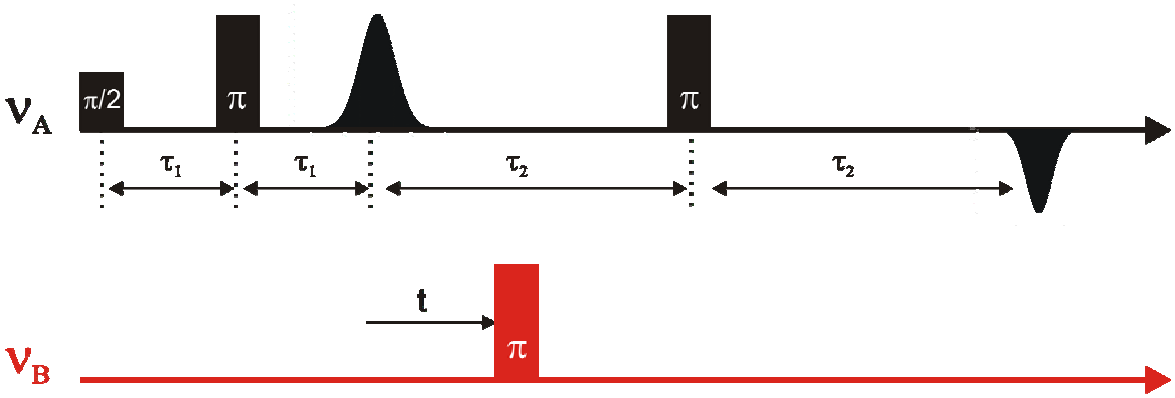

***Figure 8*:** Dead time free PELDOR sequence used for these measurements. The variable time *t* of the pump pulse is zero at the first Hahn-echo position.

In cases where the orientation of the radicals to the interconnecting vector *r* is fixed, as for example for natural paramagnetic cofactors in proteins, a different situation arises if specific orientations of the radicals can be selected by the resonant microwave pulses. Here, the orientation of the radicals with respect to the *r* vector

enters into the analysis. The observed coupling strength and the modulation depth λ_B as well as the attenuation of the dipolar oscillations will depend on the specific choice of the detection and the pump frequencies.[42] Especially at high magnetic field values, where the *g*-tensor anisotropy of the radicals is usually resolved, such orientation selectivity has been demonstrated for two tyrosyl radicals in a ribonucleotide reductase dimer at G-band frequency.[43] In this case a strong orientation dependence of the experimentally observed dipolar oscillation frequency was observed permitting to additionally obtain the relative orientation of the tyrosyl radicals with respect to the *r* vector. Such orientation selection and angular correlation effects were already studied in nitroxide biradicals with different linkers at various frequencies such as X, S, and W-band.[28,44,45]

5.1 Flexible Biradicals

The echo intensity $V(t)$ of a 4-pulse PELDOR sequence for a fixed orientation of the magnetic field B_0 in the A spin molecular axis system (of an A-B spin system described by the angles φ and ϕ) is given by:

$$V\left(t,\nu_{\mathrm{A}},\nu_{\mathrm{B}},\varphi,\phi\right)=V_0\left(\nu_{\mathrm{A}},\varphi,\phi\right)\cdot\left(1-\lambda_B(\nu_{\mathrm{B}},\Omega,\varphi,\phi)\cdot\left[1-\cos(\omega_{\mathrm{dip}}(\varphi,\phi)\cdot t)\right]\right) \quad \text{(eq. 42)}$$

where V_0 describes the A spin echo intensity for t = 0, Ω is the set of Euler angles, describing the orientation of spin B in the axis system of spin A (see Figure 9) and λ_B is the efficiency of inversion of the dipolar coupled spin B by the pump pulse.

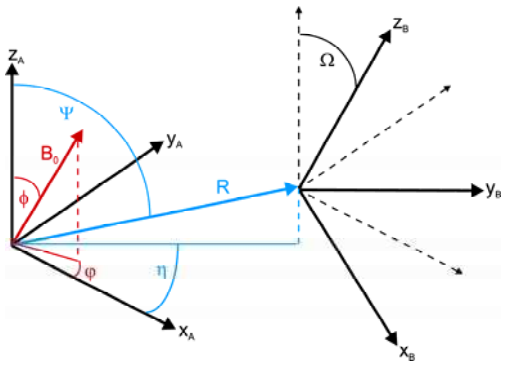

***Figure 9*:** Definition of the axis system of the discussed biradicals **1** and **2**.

For disordered powder samples the observed echo intensity is obtained by integration over all magnetic field orientations:

$$V\left(t,\nu_{\mathrm{A}},\nu_{\mathrm{B}}\right)=\iint V\left(t,\nu_{\mathrm{A}},\nu_{\mathrm{B}},\varphi,\phi\right)\sin\left(\phi\right)d\phi\,d\varphi \qquad \text{(eq. 43)}$$

The relative orientation between spin A and B as well as with respect to the vector *r* will all be random regarding flexible nitroxides in a biradical. In such cases the integration over all Ω values will effectively average the magnetic field orientation dependence of the modulation depth parameter λ_B.[33] In such cases the integration over different magnetic field orientations of equation 43 can be readily converted into an integration over all dipolar angles:

$$V\left(t,\nu_{\mathrm{A}},\nu_{\mathrm{B}}\right)=V_0\left(\nu_{\mathrm{A}}\right)\cdot\left(1-\lambda_B\left(\nu_{\mathrm{B}}\right)\cdot\left[1-\int_0^{\pi/2}\cos\left(\frac{D_{\mathrm{dip}}}{r^3}\left(1-3\cos^2\theta_{\mathrm{dip}}\right)\;\;t\right)\sin\theta_{\mathrm{dip}}d\theta_{\mathrm{dip}}\right]\right) \qquad \text{(eq. 44)}$$

5.2 Rigid Biradicals

For more rigid biradicals this simplification is not valid. The pump efficiency, described by the modulation depth parameter λ_B will depend on the mutual orientation of the two radicals A and B, described by the Euler angles Ω. Additionally, the orientation selectivity of the excitation of spin A as a function of ν_{A}, described by $V_0\left(\nu_A,\varphi,\phi\right)$, will lead to a distribution function $P\left(\Delta\nu_{AB},\theta_{dip}\right)$ of dipolar angles which differs from the $\sin\left(\theta_{dip}\right)$ distribution of a Pake pattern (see Figure 7). $\Delta\nu_{\mathrm{AB}}$ is the frequency offset between pump and detection frequency. The echo signal intensity for a given pump and detection frequency can in such general cases be described by:[33,42]

$$V\left(t,\nu_{\mathrm{A}},\nu_{\mathrm{B}}\right)=V_0\left(\nu_{\mathrm{A}}\right)\left\{1-\int_0^{\pi/2}P\left(\Delta\nu_{\mathrm{AB}},\theta_{\mathrm{dip}}\right)\cdot\left[1-\cos\left(\frac{D_{dip}}{r^3}\left(1-3\cos^2\theta_{dip}\right)\cdot t\right)\right]d\theta_{\mathrm{dip}}\right\} \qquad \text{(eq. 45)}$$

Thus, the observed dipolar frequency spectrum cannot be converted directly to a distance *r*, if the geometry of the biradical, and therefore the function $P\left(\Delta\nu_{AB},\theta_{dip}\right)$ is unknown. To unravel orientation and distance information in such cases, the excitation and pump frequencies have to be varied to excite and pump differently oriented sub-ensembles of the powder sample (see Figures 11, 22 and Section 6.1 to 6.4).

Integration of eq. 45 can be circumvented by creating an ensemble of conformers based on educated guesses using a simple geometric model of the molecule under study (see Figure 10). Calculating each conformer's PELDOR time trace with PESIM and generating the overall PELDOR interference pattern allows after comparison with the experiment insights towards the conformational flexibility of polyradicals (see Section 6.1). An alternative analysis of orientation selective PELDOR data is based on Tikhonov regularization utilizing the average overall PELDOR time traces from measurements with different $\Delta\nu_{\mathrm{AB}}$. Angular correlations of the spin labels are neglected in order to determine the distance distribution function. Afterwards, a convolution relation assigns $P\left(\Delta\nu_{AB},\theta_{dip}\right)$ via Tikhonov regularization (see Section 6.2). Generally, quantitative understanding of orientation selective PELDOR experiments or precise knowledge of the orientation and distance function in eq. 45 gives rises to comprehending conformational freedom and relative orientations of spin labels with respect to each other (see Section 6.3) in addition to the distance between the spin centers.

5.3 PELDOR "Spin Counting"

There is a growing interest in the study of large protein-protein complexes in membranes. For example, it is known from crystal structures that ion-channels and transporters[113,114] e.g. the ClC chloride channel, potassium channels, or glutamate transporters are complexes constituted out of two or more[115,116,117,118] monomeric protein units. For other ion-channels or transporters, like the polypeptide antibiotic Antiamobin,[119] the number of constituting monomers have been proposed based on molecular modeling but not verified experimentally. Furthermore, several signal transduction proteins like the fumarate sensor DcuS[120] are only active in membranes. It is proposed that the active DcuS is a specific homo-oligomer, which is only formed in membranes, the number of constituting monomers is, however, unknown. Another highly debated topic is the question whether electron transfer-proteins of the respiratory chain form super complexes[121,122] to enable fast and reliable inter-protein electron transport. An example from the RNA world is the RNA processing spliceosome - a huge machinery depending on the binding of several proteins during the catalytic cycle.[123] The number and type of interacting partners change from state to state through the process of RNA cleavage and ligation. For several of these functional states it is not fully understood how many and which proteins are involved.
X-ray crystallography can be employed to investigate the number of monomers in the oligomer, but it is still demanding to obtain suitable single crystals of large complexes and it has not yet been possible to crystallize them within membranes. Therefore, complementary biophysical methods capable of measuring the number of interacting monomers with or without membrane, like cryo-electron microscopy,[124] are needed. Electrospray ionization mass spectrometry (ESI) is a well established method for the determination of such non-covalent interactions in solution.[125,126] Two other methods able to extract the number of constituting units in solution are confocal time correlated fluorescence spectroscopy,[127,128] and as shown recently, fluorescence resonance energy transfer (FRET).[129,130] Dynamic light scattering can be employed to monitor soluble aggregates and oligomers by their hydrodynamic properties,[131,132,133] and first approaches in liquid-[134] and ssNMR[135] are published.
1984 Milov, Tsvetkov et al. suggested that PELDOR may not only be employed in order to access spin-spin distances, but also to count the number of spin centers from the modulation depth.[46] They used this to postulate the aggregation state of small

peptides.[47] Hence, this thesis shows an experimental verification of PELDOR "Spin Counting" using fully characterized test systems (see Section 2) for up to four spins. Therefore, suitable model systems mimicking different geometries and aggregation states of biomolecules were synthesized and used as model systems to evaluate the method with respect to accuracy and limitations for biological applications.

Assuming that the spin-orientations are not changed due to spin diffusion or spin-lattice relaxation, J_{AB} to be negligible versus ω_{dip} and also that the radical centers in a cluster do not bear any angular correlation $V\left(t,\nu_A,\nu_B\right)$ can be described by:[33,46]

$$V\left(t,\nu_A,\nu_B\right)=\frac{V_0}{n}\sum_{A=1}^{n}\int_0^{\pi/2}\prod_{\substack{B=1\\B\neq A}}^{n}\left(1-P\left(\Delta\nu_{AB},\theta_{dip}\right)\left[1-\cos\left(\omega_{AB}t\right)\right]\right)d\theta \qquad \text{(eq. 46)}$$

Considering a random distribution of clusters and neglecting excluded volumes the coupling between spins can be deduced parameter-free from the time domain signal by division of *V(t)* by the intermolecular background and cosine Fourier transformation. In disordered samples a broad distribution of ω_{AB} values exists. Therefore, the $\cos\left(\omega_{AB}t\right)$ terms in eq. 46 will interfere to zero for times $t\gg\omega_{AB}^{-1}$ and $V\left(t,\nu_A,\nu_B\right)$ will tend to its limit V_λ, which is the value of $V\left(t,\nu_A,\nu_B\right)$ when all modulation is damped. Assuming that all B spins are of similar nature, V_λ can be written in the form of eq. 47:

$$V_\lambda=\left(1-\lambda_B\right)^{(n-1)} \qquad \text{(eq. 47)}$$

Thus, V_λ values factorize under the conditions given above, e.g. a triradical can be described as the square of a biradical and a tetraradical as the cube of a biradical. This approximation will not be valid if the coupling spins belong to radicals with different spectral widths. In that case the different λ_B-values have to be taken into account explicitly.

From eq. 46 follows that the number of radicals in a cluster is:

$$n = \frac{\ln V_\lambda}{\ln\left(1-\lambda_B\right)} + 1 \qquad \text{(eq. 48)}$$

If $\lambda \ll 1$, then eq. 47 can be approximated linearly to eq. 49:[46]

$$V_\lambda = 1 - \lambda_B\left(n-1\right) \qquad \text{(eq. 49)}$$

The only free parameter in the calculation of n is λ_B, which can be determined experimentally using standard biradical **16**. In case of strong angular correlations different λ_B-values for each A-B pair in eq. 46 have to be explicitly taken into account.

5.4 Disentangling Exchange and Dipolar Coupling

Commonly, the PELDOR data are analyzed under the assumption that the isotropic exchange coupling constant J is negligible versus the anisotropic dipolar coupling. However, if J is non-zero, its inclusion into the PELDOR analysis by using eq. 50 may enable separating J from D and determining its magnitude and sign.

$$\nu_{AB} = \frac{\mu_0 h}{4\pi}\frac{\gamma_A\gamma_B}{r^3}\left(1-3\cos^2\theta\right) + J = \frac{D_{dip}}{r^3}\left(1-3\cos^2\theta\right) + J = D\left(1-3\cos^2\theta\right) + J \qquad \text{(eq. 50)}$$

Several examples with an explicit inclusion of J in the PELDOR analysis were reported: a theoretical description with examples of molecules exhibiting very small exchange coupling constants,[33,49] and experiments on spin labeled copper(II)-porphyrines[50,51] and aromatic systems.[44]

In eq. 50, J is defined via the Hamiltonian $H_{Exch} = JS_AS_B$ and thus a positive value for J indicates an antiferromagnetic whereas a negative sign reflects a ferromagnetic coupling. Note that D is according to its definition in eq. 50 always positive. Taking J explicitly into account may yield more accurate distances as well as information regarding the nature of the magnetic coupling (see Section 6.4). The latter is especially important for the design of molecular magnets.[73,110,136,137,138,139,140]

5.5 Brief Comparison with other Methods

Another EPR based method for nanometer distance measurements is the excitation of double quantum coherences (DQC).[15,16,17] However, this method is technically more demanding, because the full EPR-spectra have to be excited and the nature of the experiment does not allow counting the number of spins in a cluster easily.

In comparison to high-resolution NMR, dynamic light scattering, fluorescence spectroscopy, or ESI that can all be performed in solution under native conditions, PELDOR measurements need to be performed in immobilized samples, usually glassy frozen solutions. On the other hand, PELDOR is not as restricted in system size as NMR and measurements can be performed in membranes yielding in the same measurement not only the number of constituting monomers, but also precise information about their geometric arrangement. The method is comparable to spin-spin distance measurements in ssNMR e.g. REDOR,[41] however, due to the higher magnetic moment of electron spins, distances of up to 80 Å[28,29] are accessible by PELDOR. More detailed comparisons to other methods are to be found e.g. in a review article by Schiemann and Prisner[12] or in the Introduction.

6. Results and Discussion

6.1 Orientation Selection and Conformational Flexibility: a Benchmark Study using Model Nitroxide Biradicals and PESIM

This chapter has been published in the Journal of *Molecular Physics*, **105**, 2153, 2007. and discusses the influence of orientation selection in rigid biradicals and its quantitative analysis via PESIM leading to insights towards conformational flexibility of the investigated model biradicals. It is entitled "Conformational flexibility of nitroxide biradicals determined by X-band PELDOR experiments" and may be regarded as a benchmark test for further conformational studies of biomolecules (see Section 6.3). The author contributed all experimental PELDOR spectra, the synthesis of the organic model compounds as well as in depth literature research regarding the flexibility of related systems.

6.1.1 Abstract

PELDOR experiments have been performed at X-band (9 GHz) frequencies on **1** and **2**. All PELDOR time traces were recorded with the pump frequency ν_B set at the center of the nitroxide spectra to achieve maximum pumping efficiency, while the detection frequency ν_A was stepped between a frequency offset $\Delta\nu_{AB} = \nu_A - \nu_B$ of +40 to +80 MHz. The modulation frequencies and the damping of the oscillations change as a function $\Delta\nu_{AB}$, whereas the modulation depth λ_B for **1** and **2** was only very slightly altered. This can be explained by the selection of different orientations of nitroxide radicals with respect to the external magnetic field as a function of $\Delta\nu_{AB}$. Quantitative simulations of the PELDOR time traces could be achieved for both molecules and for all offset frequencies using a simple geometric model, described by a free rotation of the nitroxide radical around its acetylene bond and a single bending mode of the interconnecting molecular bridge. The results show that the distribution function for the relative orientations of nitroxides **1** and **2** with respect to each other and with respect to the dipolar vector *r* deviates from a random distribution and thus have to be taken into account to quantitatively simulate the PELDOR traces. Vice

versa, a quantitative simulation via PESIM of PELDOR time traces with variable offset frequencies allows for extraction of the conformational freedom of **1** and **2**.

6.1.2 Simulation of Orientation Selective PELDOR Data using PESIM

A conformational ensemble of biradicals is created and their calculated PELDOR time traces are compared with experiments. The conformational ensemble contains a number N (typically 1000 to 10000) of different conformers, each characterized by a distance vector R, with polar angles (ψ,η) in the axis system of spin A and Euler angles Ω describing the mutual orientation of molecule B with respect to molecule A. For a definition of the axis system see Figure 9.

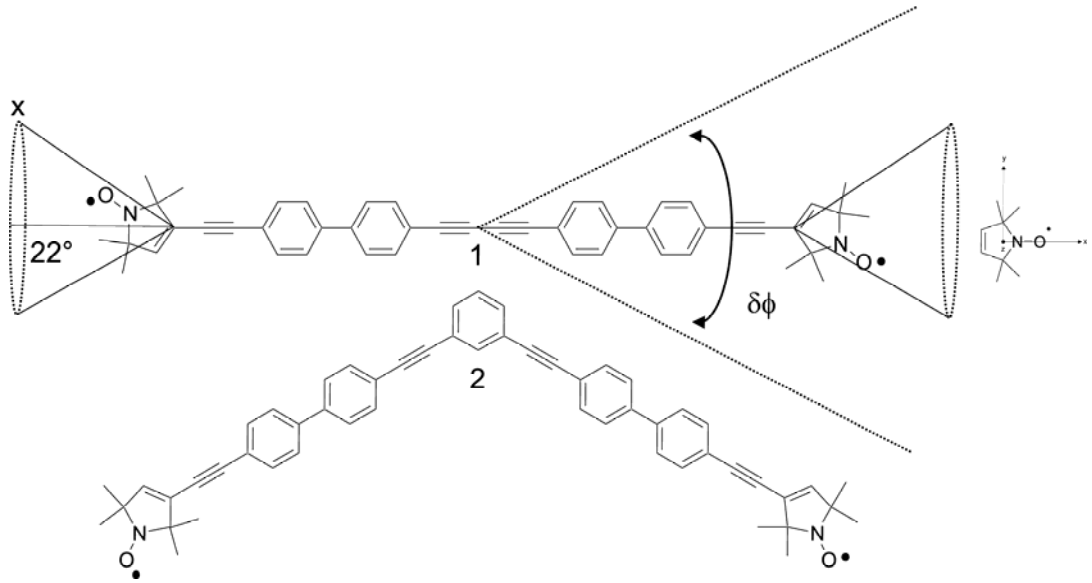

***Figure 10*:** Structures of the two molecules **1** and **2** used in the experiments. The geometric model used to create an ensemble of conformers for this biradicals and the molecular axis system are indicated. The nitroxide radicals are assumed to rotate freely around their acetylene bond (cone with angle of 22°) and the mobility of the bridge is described by a single bending motion with a Gaussian distributed width $\delta\phi$.

The input data for the structure of the conformers was generated by a simple geometrical model of the biradical (see Figure 10). For each of these conformers the resonance positions of molecules A and B are calculated for all orientations of the magnetic field vector B_0 in the molecular axis frame of spin A, taking anisotropic nitrogen hyperfine coupling and the anisotropy of the g-tensor into account:

$$\nu_{\mathrm{res}}^{\mathrm{A}} = \beta_{\mathrm{e}} \cdot B_0 \cdot g_{\mathrm{eff}}^{\mathrm{A}} + m_{\mathrm{I}} \cdot A_{\mathrm{eff}}^{\mathrm{A}}$$
$$g_{\mathrm{eff}}^{\mathrm{A}} = \sqrt{(g_{\mathrm{xx}} \cdot \cos\varphi \cdot \sin\phi)^2 + (g_{\mathrm{yy}} \cdot \sin\varphi \cdot \sin\phi)^2 + (g_{\mathrm{zz}} \cdot \cos\phi)^2} \qquad \text{(eq. 51)}$$
$$A_{\mathrm{eff}}^{\mathrm{A}} = \sqrt{(A_{\mathrm{xx}} \cdot \cos\varphi \cdot \sin\phi)^2 + (A_{\mathrm{yy}} \cdot \sin\varphi \cdot \sin\phi)^2 + (A_{\mathrm{zz}} \cdot \cos\phi)^2}$$

A_{eff} and g_{eff} are the effective hyperfine couplings and g-values for the specific magnetic field orientation described by the polar angles φ and ϕ, m_{I} is the nuclear spin value (-1, 0, +1 for ^{14}N). Hyperfine and g-tensor axis are considered as collinear to the molecular axis system for this simulations. The resonance frequencies of spin B can be calculated after describing the hyperfine and g-tensor of spin B in the coordinate system of spin A, as given by the transformation:

$$G_{\mathrm{B}}^{\mathrm{A}} = D(\Omega) G_{\mathrm{B}}^{\mathrm{B}} D^{-1}(\Omega)$$
$$A_{\mathrm{B}}^{\mathrm{A}} = D(\Omega) A_{\mathrm{B}}^{\mathrm{B}} D^{-1}(\Omega) \qquad \text{(eq. 52)}$$

where $D(\Omega)$ is the respective rotation matrix. Additionally, an inhomogeneous line width of 0.6 mT has been taken into account by a Gaussian distribution to calculate the final resonance frequencies for spin A and spin B respectively.
Using these calculated resonance frequencies the excitation efficiency of pump and detection pulses for spin A and B can easily be determined. For a microwave pulse with a Rabi oscillation frequency $\omega_{\mathrm{I}}=\gamma B_1$ and a resonance frequency $\Delta\omega_{\mathrm{r}} = 2\pi\,(\nu_{\mathrm{mw}}-\nu_{\mathrm{res}})$, the inversion efficiency is given by:

$$I_{\mathrm{ex}}(\Delta\omega_{\mathrm{r}}, \varphi, \phi) = \left(\frac{1}{2} - \frac{\Delta\omega_{\mathrm{r}}^2 + \omega_{\mathrm{I}}^2 \cdot \cos\left(\frac{\pi\sqrt{\Delta\omega_{\mathrm{r}}^2 + \omega_{\mathrm{I}}^2}}{\omega_{\mathrm{I}}} \right)}{2\left(\Delta\omega_{\mathrm{r}}^2 + \omega_{\mathrm{I}}^2\right)} \right) \qquad \text{(eq. 53)}$$

For a large sample size the inhomogeneous field strength B_1 distribution over the resonator height can be described by a half sine-wave. Integration of eq. 53 over the resonator length leads to an excitation profile which can be approximated by:

$$I_{ex}(\Delta\omega_r,\varphi,\phi)=\frac{\omega_1^2}{\omega_1^2+4\cdot\Delta\omega_r^2} \qquad \text{(eq. 54)}$$

This allows to calculate the excitation functions of spin A, $V_0(\nu_A,\varphi,\phi)$, and of spin B, $\lambda(\nu_B,\Omega,\varphi,\phi)$, and thereafter the dipolar distribution function $P(\Delta\nu_{AB},\theta_{dip})$ for each conformer. The pump pulse frequency ν_B is fixed to the centre of the nitroxide spectrum in these experiments and only the detection frequency ν_A is varied. The final PELDOR signal for a given frequency offset $\Delta\nu_{AB}$ is a sum over all magnetic field orientations equally distributed on a sphere (typically 20000) and over all conformers. All simulations are performed with PESIM.

6.1.3 Results and Discussion

For **1** and **2** (see Figure 10) the experimental PELDOR time traces as a function of the detection frequency offset $\Delta\nu_{AB}$ ranging from 40-80 MHz are shown in Figure 11.
The pumping frequency ν_B is for all experiments kept at the centre of the nitroxide spectra, as shown in the inset of Figure 11. As can be seen the oscillation frequencies vary as a function of $\Delta\nu_{AB}$. This indicates the presence of angular correlation effects for **1** and **2**. For the 80 MHz offset a high orientation selectivity for the observer spin A is obtained with the chosen pulse lengths; only nitroxide molecules with the plane normal almost parallel to the external magnetic field are observed, whereas for an offset of 40 MHz the orientation distribution of the excited nitroxides is broader. This is illustrated in Figure 12. The contribution to the signal is encoded in color for each orientation of the external magnetic field with respect to the nitroxide molecular axis system. Pumping in the centre of the nitroxide spectra with a 12 ns π–pulse length excites all molecular orientations. Only nitroxide molecules with the plane normal parallel to the external magnetic field and in the ^{14}N nuclear $m_I = \pm 1$ spin states (with a large hyperfine coupling) are not excited. For the linear biradical **1**, where the molecular *z*-axis of the two nitroxides is perpendicular to the *r* vector (considering a rigid molecule), this orientation selection leads to simple predictions for the observable dipolar frequencies: The parallel frequency component should only appear for small frequency offsets $\Delta\nu_{AB}$, whereas at 80 MHz, with high orientation selection, only the perpendicular component of the Pake pattern should be observable.

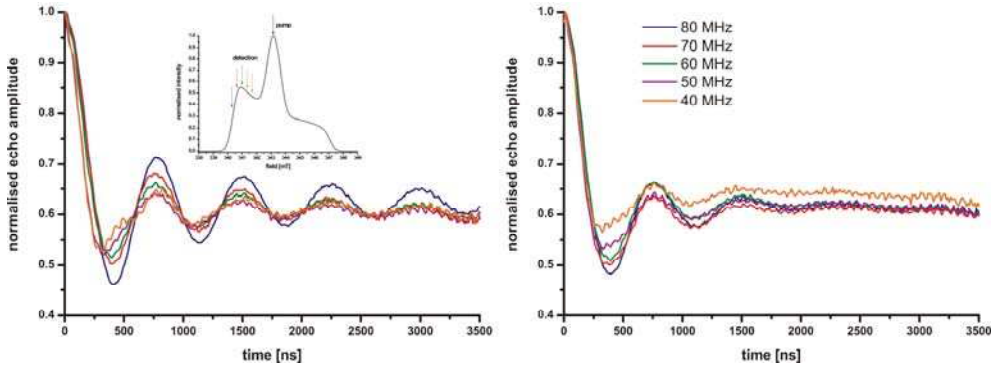

***Figure 11*:** Experimental PELDOR time traces for offset frequencies $\Delta\nu_{AB}$ between 40 and 80 MHz for molecule **1** (a) and **2** (b). All time traces are normalized to 1 for $t = 0$ and the intermolecular decay is removed by division by a mono-exponential decay, which is determined by fitting the experimental time traces for long t values. Inset: Field swept EPR spectra of the nitroxide with the position of pump and detection frequencies indicated by arrows.

This tendency is experimentally observed, as shown in Figure 11. On the other hand the modulation depth λ_B does not change as a function of $\Delta\nu_{AB}$ for **1** and **2**. Also for the bent biradical **2** a change of oscillation frequencies is observed as a function of $\Delta\nu_{AB}$ (see Figure 11b). The effect is less pronounced, compared to **1**, because for **2** a much faster damping of the oscillations occurs.

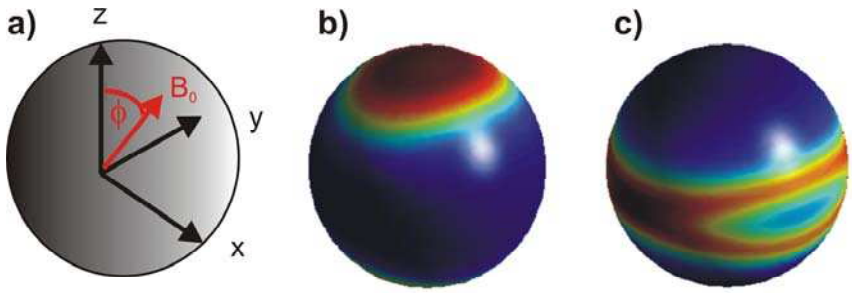

***Figure 12*:** a) definition of the axis system. b) calculated orientation selection for a nitroxide radical with $\Delta\nu_{AB}$ = 80 MHz c) $\Delta\nu_{AB}$ = 40 MHz. A pulse length of 32 ns and an inhomogeneous line width of 6 G is used for the simulations. The color code gives the intensity of the excitation efficiency (increasing from blue to red).

The simple geometric model applied to simulate the conformational distribution of the biradicals is shown in Figure 10. The 5-ring nitroxide molecules are allowed to rotate freely around their acetylene bond axis. This leads to a random orientation of the nitroxide x-axis (N-O) on a cone with an angle of 22° with respect to the linear acetylene linker. The nitroxide *z*-axis (out of plane) is perpendicular to the linear linker but otherwise randomly oriented. The conformational flexibility of the interconnecting molecular bridge is modeled by a simple bending motion, as depicted

in Figure 10, with a Gaussian half width angle $\delta\phi$. The highest orientation selection and symmetry is achieved for molecule **1** with a frequency offset of 80 MHz. Under these conditions only nitroxide radicals with the normal parallel to the external magnetic field contribute to the signal. The bending angle $\delta\phi$ was optimized on the basis of this experimental data set. The best result was obtained with a bending angle of $\delta\phi = 40°$. With the same conformational distribution the frequencies, modulation depth and attenuation of the PELDOR traces obtained with other frequency offsets could also be well reproduced, as shown in Figure 13 for $\Delta\nu_{AB}$ = 80 MHz and 40 MHz.

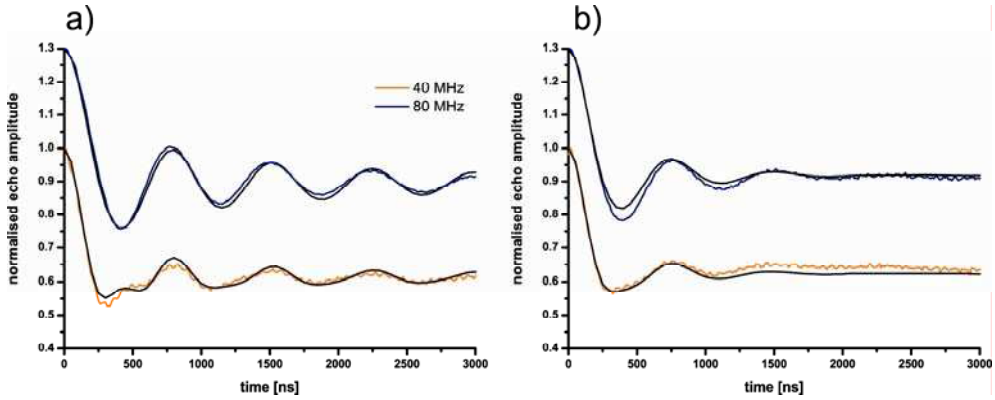

***Figure 13*:** Simulated PELDOR time traces for **1** (a) and **2** (b) for $\Delta\nu_{AB}$ = 80 MHz (blue, the normalized trace in the graph was shifted by +0.3 in y-direction for reasons of better visibility) and $\Delta\nu_{AB}$ = 40 MHz (orange). Simulations are shown in black. Parameters for the conformational distribution used for the simulation are given in the text.

Especially the damping and modulation depth can be compared much better with a simulation of the time domain data instead of often used frequency domain data. The attenuation of the oscillations is strongly influenced by the bending angle $\delta\phi$. A quantitative reproduction of the experimentally observed attenuation of the oscillations can only be achieved taking into account this relatively strong bending. The large conformational freedom of the molecular bridge is in qualitative agreement with published MD-studies.[141,142] The MD and the simple conformational model both lead to a slightly shorter average distance than the predicted minimum energy structure and therefore a faster oscillation period, in agreement with the experimental data. Nevertheless, even with this fairly large flexibility of the bridge, orientation correlations exist, evident from the changes in oscillation frequencies for the smaller offset frequency of 40 MHz. Another factor that could alter the shape of the PELDOR traces with varying frequency offset is the spectral overlap between pump and

detection pulses. The most prominent effect is that the short pump pulse also interacts with A spins excited by the detection pulse echo sequence. These A spins will not refocus at the echo position anymore and therefore do not contribute to the PELDOR signal. Indeed switching on the pump pulse leads to an experimentally observed reduction in echo intensity. Simulation of this interference effect for $\Delta\nu_{AB}$ = 40 MHz also showed a reduction in echo intensity for the studied conformer ensemble, but it did not change the PELDOR time trace shape within the experimental accuracy. This effect will be smaller for larger offset values, indicating that it does not contribute to the offset dependent change in oscillation frequencies for the chosen experimental conditions.

Thus, the obvious change in oscillation frequency as a function of $\Delta\nu_{AB}$ can be attributed to a different selection of dipolar angles in both experiments. Figure 14 depicts the dipolar angle distribution function $P(\Delta\nu_{AB},\theta_{dip})$ for **1** extracted from the simulations for $\Delta\nu_{AB}$ = 40 MHz and 80 MHz. Both distributions deviate strongly from the $\sin\theta_{dip}$ -distribution expected for random orientations of the nitroxides with respect to the bridge. Whereas the distribution for $\Delta\nu_{AB}$ = 80 MHz is mainly located around θ_{dip} = 90° also smaller dipolar angles contribute to the simulations with 40 MHz frequency offset. Especially values close to θ_{dip} = 0° lead to the additional faster oscillations seen in this time trace.

For biradical **2**, with an angle of 60° in the bridge, the same conformational model, with a free rotation of the nitroxides around the acetylene linker bond and a single bending distribution $\delta\phi$, was used to simulate the PELDOR time traces. The experimental PELDOR time traces for all offset frequencies are reproduced well with a smaller mobility of the bridge of $\delta\phi$ = 20°. Simulations and experimental data are summarized in Figure 13 for 80 MHz and 40 MHz frequency offsets. The much faster damping of the oscillations is a consequence of the angle in the bridge. The bending motion causes a much more pronounced effect on the distance in this case, leading to a broader distance distribution and therefore faster damping of the oscillations.

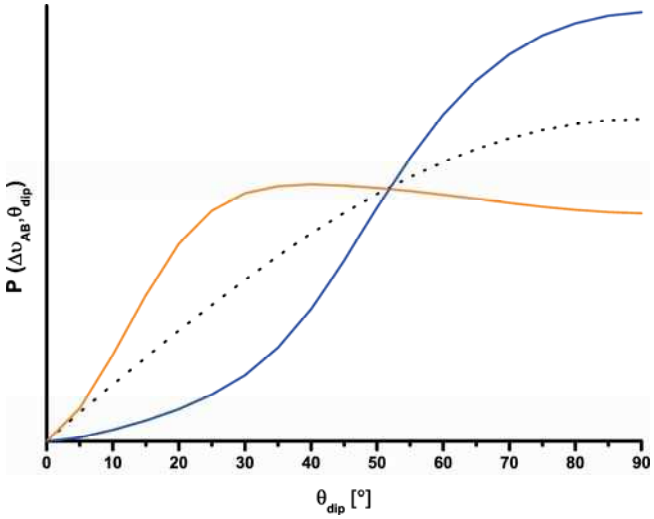

***Figure 14*:** The function $P(\Delta\nu_{AB}, \theta_{dip})$ describing the relative intensities of dipolar frequencies contributing to the PELDOR signal of an disordered powder sample for two offset frequencies of $\Delta\nu_{AB}$ = 80 MHz (blue) and $\Delta\nu_{AB}$ = 40 MHz (orange). For the simulation the geometric model of biradical 1 as defined in the text was used. The black line shows the expected $\sin(\theta_{dip})$ intensity for a biradical without any angular correlations, corresponding to a Pake pattern.

This might also explain the slightly smaller angle $\delta\phi$ for this molecule: Based on the simple model, where the conformational freedom of the bridge is approximated by only a single bending motion, the distance variation is obviously underestimated for the linear biradical **1**.

Both cases demonstrate that X-band PELDOR time traces are very sensitive to the conformational freedom of the biradical, which in both cases cannot be described accurately by a random orientation of the nitroxide radicals with respect to the molecular bridge. Both molecules can be reasonably well simulated by applying simple geometric models.

6.1.4 Conclusion

On a set of two biradicals it was shown that the $\Delta\nu_{AB}$-dependence of the oscillation frequencies arises from orientation correlations between the nitroxides and the distance vector *r*. Even with large bending motions of the bridge such effects may remain and hamper the analysis of the distance *r* between the two unpaired electrons. If the experiment is performed only with one fixed offset frequency and analyzed by assuming a random orientation distribution, a wrong *r* distribution could result. This can be avoided by taking PELDOR time traces with different pump and detection frequencies. Summing all these time traces may lead to an averaging of such

orientation correlations, as has been shown by Godt et al.[28] On the other side a quantitative analysis of the frequency offset dependence will allow to gather a detailed picture of the conformational distribution of the molecule. An analogous situation might also arise in biological applications where steric constrains restrict the mobility of the spin labels. By a systematic variation of the detection frequency ν_A such effects can easily be detected and taken into account. This yields additional information on the mutual orientation of the two nitroxide radicals, which might be interesting in structural studies.

6.2 An Alternative Analysis of Orientation Selective PELDOR Data: a Benchmark Study using Model Nitroxide Biradicals and Tikhonov Regularization

This chapter was published in *The Journal of Chemical Physics*, **130**, 064102, 2009, DOI:10.1063/1.3073040 and is entitled "Molecular orientation studies by pulsed electron-electron double resonance experiments". The author contributed all experimental PELDOR spectra as well as the synthesis of the organic model compounds and simulations of PELDOR time traces from MD generated conformers.

6.2.1 Abstract

In case of rigid spin labels, the PELDOR signal can be represented as a convolution of a kernel function containing the distance distribution function and an orientation intensity function (see eq. 45). The last chapter circumvented the integration of eq. 45 by creating a conformational ensemble of biradicals and comparing their calculated PELDOR time traces with the respective experiments.
Here, the following strategy is proposed to obtain both functions directly from the experimental data:

1.) the distance distribution function is estimated by Tikhonov regularization with DeerAnalysis[143,144] using the average over all PELDOR time traces with different frequency offsets and neglecting angular correlations of the spin labels.
2.) the convolution relation is employed to determine the orientation intensity function, using again Tikhonov regularization.

Adopting small nitroxide biradical molecules **1** and **2** as simple examples, it is shown that the approach works well and is internally consistent. Furthermore, independent molecular dynamics simulations are performed and utilized to calculate PELDOR signals, distance distributions, and orientational intensity functions. The calculated and experimental results are found to be in excellent overall agreement.

6.2.3 Introduction

As discussed in the previous chapter X-band PELDOR time traces can be employed to deduce the conformational flexibility of molecules **1** and **2**. In this case, the conformational flexibility could be satisfactory described by a simple geometrical model. A more complex situation arises in biological macromolecules, where the restricted flexibility of the spin label and the biomolecule itself are unknown. Thus, a method capable of disentangling the distance information, *f(r)*, from the orientational information $P\left(\Delta\nu_{\mathrm{AB}},\theta_{\mathrm{dip}}\right)$ is required. A PELDOR signal can be represented as a convolution of the orientation intensity function $P'\left(\Delta\nu_{\mathrm{AB}},\theta_{\mathrm{dip}}\right)=\dfrac{P\left(\Delta\nu_{\mathrm{AB}},\theta_{\mathrm{dip}}\right)}{\sin\theta_{dip}}$ and a kernel function containing the distance distribution function *f(r)*. This relation is used to determine both *f(r)* and $P'\left(\Delta\nu_{\mathrm{AB}},\theta_{\mathrm{dip}}\right)$ from the experimental data. The following strategy is employed. In a first step, the distance distribution *f(r)* is estimated by the Tikhonov regularization using the average of all PELDOR time traces with different detection frequency offsets and neglecting angular correlations of the spin labels. Second, the convolution relation is employed to determine the orientation intensity function $P'\left(\Delta\nu_{\mathrm{AB}},\theta_{\mathrm{dip}}\right)$ via the Tikhonov regularization of the experimental data. To study its potential and numerical stability, the method is first validated by considering various computer-generated PELDOR time traces with given functions $P'\left(\Delta\nu_{\mathrm{AB}},\theta_{\mathrm{dip}}\right)$. Then the approach is applied to analyze PELDOR experiments on two nitroxide biradicals. The obtained experimental results for the functions *f(r)* and $P'\left(\Delta\nu_{\mathrm{AB}},\theta_{\mathrm{dip}}\right)$ are compared to results obtained by independent all-atom molecular dynamics simulations in explicit solvent. An excellent overall agreement between theory and experiment is obtained, suggesting the applicability of the proposed approach.

6.2.4 Determination of the Orientation Intensity Function via Tikhonov Regularization

The measured PELDOR signal depends in a complicated way on both experimental conditions and on the structure of the molecular system. In an experimental study, however, one is typically interested to solve the inverse problem. That is, given some experimental data:

$$V(t,\nu_{\mathrm{A}},\nu_{\mathrm{B}}) = V_0(\nu_{\mathrm{A}})\left\{1-\int_0^{\pi/2} P(\Delta\nu_{\mathrm{AB}},\theta_{\mathrm{dip}})\cdot\left[1-\cos(\omega_{dip}\cdot t)\right]d\theta_{\mathrm{dip}}\right\} \qquad \text{(eq. 45)}$$

one wants to determine the underlying molecular structure causing the signal. This factorization in eq. 45 is justified, if the fluctuations of the spin label distances *r* are only weakly correlated with the fluctuations of spin label orientations. The above factorization allows to write the normalized PELDOR signal $S(t,\nu_A,\nu_B) = \frac{V(t,\nu_A,\nu_B)}{V_0(\nu_A)}$ in the form of a Fredholm integral of the first kind:[145]

$$S(t,\nu_A,\nu_B) = 1+\int_0^1 P'(\Delta\nu_{\mathrm{AB}},\theta_{\mathrm{dip}})K(\cos\theta_{dip},t)\,d\cos\theta_{dip}$$

with (eq. 55)

$$P'(\Delta\nu_{\mathrm{AB}},\theta_{\mathrm{dip}}) = \frac{P(\Delta\nu_{\mathrm{AB}},\theta_{\mathrm{dip}})}{\sin\theta_{dip}}$$

and the kernel function

$$K(\cos\theta_{dip},t) = \frac{1}{N}\sum_i^N\left[\cos\left(D_{dip}\frac{1-3\cos^2\theta_{dip}}{r_i^3}t\right)-1\right] \qquad \text{(eq. 56)}$$

in a sample with $i = 1...N$ molecular structures.

Eq. 55 and 56 represent the central theoretical result of this paper. Representing the PELDOR signal as a convolution of two functions, $K\left(\cos\theta_{dip},t\right)$ and $P'\left(\Delta\nu_{\mathrm{AB}},\theta_{\mathrm{dip}}\right)$ the formulation allows calculating one of the functions provided if the other is known. For example, by assuming that the distances between the radical electrons are described by a Gaussian distribution $f\left(r,r_0,\sigma\right)=\frac{1}{\sqrt{2\pi\sigma^2}}\exp\left[-\frac{\left(r-r_0\right)^2}{2\sigma^2}\right]$ the resulting kernel is:

$$K\left(\cos\theta_{dip},t\right)=\frac{1}{\sqrt{2\pi\sigma^2}}\int_0^{\infty}\exp\left[-\frac{\left(r-r_0\right)^2}{2\sigma^2}\right]\left[\cos\left(D_{dip}\frac{1-3\cos^2\theta_{dip}}{r_i^3}t\right)-1\right]dr \quad \text{(eq. 57)}$$

In a second step, this result in combination with eq. 55 can be employed to calculate the orientation intensity function $P'\left(\Delta\nu_{\mathrm{AB}},\theta_{\mathrm{dip}}\right)$ from the experimental data. It is worthwhile to note that the function $P'\left(\Delta\nu_{\mathrm{AB}},\theta_{\mathrm{dip}}\right)$ has two important features. First, if it is constant, orientation selection will not occurs in the system. Second, at long times, when all PELDOR oscillations are damped, the asymptotic value of the signal is given by:

$$S\left(t\to\infty,\nu_A,\nu_B\right)=1-\int_0^1 P'\left(\Delta\nu_{\mathrm{AB}},\theta_{\mathrm{dip}}\right)d\cos\theta_{\mathrm{dip}} \quad \text{(eq. 58)}$$

Assuming that an explicit form of the kernel is given, eq. 55 can be solved numerically to deduce the intensity function $P'\left(\Delta\nu_{\mathrm{AB}},\theta_{\mathrm{dip}}\right)$. To this end, the time *t* is discretized into *L* steps of length $\Delta t=\frac{t_{\max}}{L}$ and the parameter $\cos\theta_{dip}\in\left[0,1\right]$ into *M* steps of length $\Delta\cos\theta_{dip}=\frac{1}{M}$. This allows a representation of eq. 55 in matrix form as:

$$s_i=\sum_j K_{ij}P'_j\left(\Delta\nu_{\mathrm{AB}},\theta_{\mathrm{dip}}\right)\text{ or }\mathbf{s}=\hat{K}\mathbf{P}'\left(\mathbf{\Delta\nu_{AB}},\mathbf{\theta_{dip}}\right) \quad \text{(eq. 59)}$$

where $s_i \equiv S\left(t_i, \nu_A, \nu_B\right) - 1$, $K_{ij} \equiv K\left(T_i, \cos\theta_{dip,j}\right)\Delta\cos\theta_{dip}$ and

$$P_j'\left(\Delta\nu_{\mathrm{AB}}, \theta_{\mathrm{dip}}\right) = P'\left(\Delta\nu_{\mathrm{AB}}, \theta_{\mathrm{dip,j}}\right)$$

Expression 59 constitutes an over-determined system of linear equations, i.e., it represents an ill-posed problem whose solutions may be unstable. As a consequence, small differences in the experimental data, such as noise, can lead to large deviations of the estimated results for λ. To solve eq. 59, Tikhonov regularization[29,34,145,146] is utilized in order to minimize the functional

$$\left\|\mathbf{s}_{\exp} - \hat{K}\mathbf{P}'\left(\mathbf{\Delta\nu_{AB}}, \mathbf{\theta_{dip}}\right)\right\| + \alpha\left\|\frac{d^2P'\left(\Delta\nu_{\mathrm{AB}}, \theta_{\mathrm{dip}}\right)}{d\cos^2\theta_{dip}}\right\| \rightarrow \min \qquad \text{(eq. 60)}$$

Here, α is a regularization parameter that depends on the quality of the experimental data and determines the smoothness of the solution. The above expression is minimized, when:

$$\mathbf{P}'\left(\mathbf{\Delta\nu_{AB}}, \mathbf{\theta_{dip}}\right) = \frac{1}{\left|\hat{K}^T\hat{K} + \alpha\hat{D}^T\hat{D}\right|}\hat{K}^T\mathbf{s}_{\exp} \qquad \text{(eq. 61)}$$

where $\hat{D}$ is the second derivative operator written in matrix representation.
To study its performance and numerical stability, the method was first validated by considering various computer generated PELDOR time traces with polynomial test functions $P_i'\left(\cos\theta_{dip}\right)$ (see Figure 15). The kernel function 57 is assumed with Gaussian parameters r_0 = 3 nm and σ = 0.1 nm, and Gaussian noise of zero mean and 0.75% of the total echo amplitude is added to the PELDOR signals. The resulting set of signals was employed to find the function $P_i'\left(\cos\theta_{dip}\right)$ on the basis of the Tikhonov regularization method, assuming a regularization parameter of α = 50. Figure 15 demonstrates that the regularized orientation intensity functions are in good agreement.

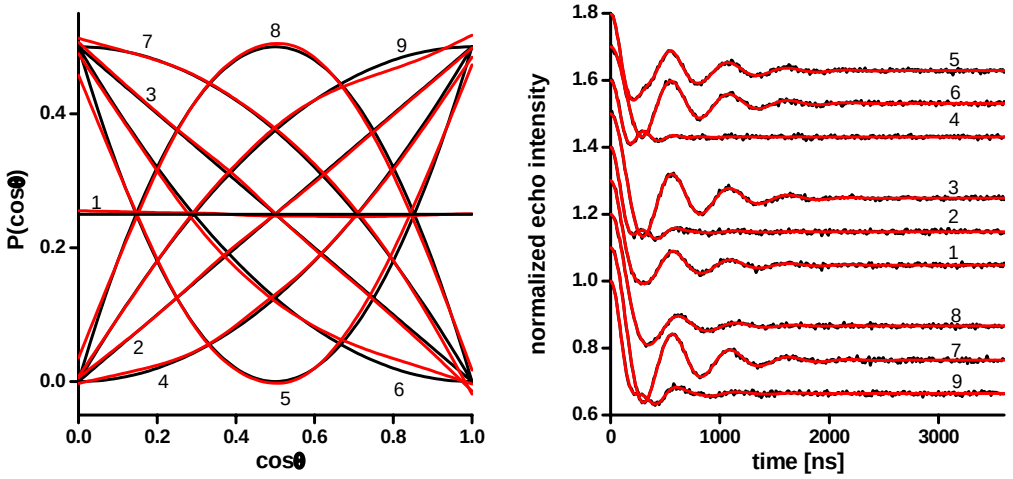

***Figure 15*:** Validation of the proposed deconvolution method of synthesized PELDOR signals, assuming a Gaussian distribution of spin label distances with superimposed noise and various test functions $P_i'\left(\cos\theta_{dip}\right)$ of the orientation intensity:

$$P_1'\left(\cos\theta_{dip}\right)=0.25,\ P_2'\left(\cos\theta_{dip}\right)=0.5\cos\theta_{dip},\ P_3'\left(\cos\theta_{dip}\right)=0.5\left(1-\cos\theta_{dip}\right),\ P_4'\left(\cos\theta_{dip}\right)=0.5\left(\cos\theta_{dip}\right)^2,$$
$$P_5'\left(\cos\theta_{dip}\right)=2\left(0.5-\cos\theta_{dip}\right)^2,\ P_6'\left(\cos\theta_{dip}\right)=\left(0.5-\cos\theta_{dip}\right)^2,\ P_7'\left(\cos\theta_{dip}\right)=0.5\left(0.5-\cos\theta_{dip}\right)^2,$$
$$P_8'\left(\cos\theta_{dip}\right)=0.5-2\left(0.5-\cos\theta_{dip}\right)^2 \text{ and } P_9'\left(\cos\theta_{dip}\right)=0.5\left(1-\left(0.5-\cos\theta_{dip}\right)\right)^2$$

The left panel compares these polynomial functions (black lines) with the regularized orientation intensity functions (red lines) obtained from the deconvolution method. The right panel compares PELDOR time traces as obtained from the input polynomial functions (black lines) and the regularized functions (red lines).

The damped oscillations of the PELDOR time traces shown in Figure 16a reveal that the mean distance between the two nitroxide spin labels is ~ 3.3 nm for both biradicals (eq. 57).

The somewhat faster damping of the oscillations of compound **2** indicates that the underlying distance distribution is broader for the bent radical **2** as for the linear system **1**. Furthermore, the dependence of the oscillation frequency on the offset $\Delta\nu_{AB}$ indicates the presence of angular correlation effects. Indeed, previous studies[104] have shown that the motion of the spin labels is quite restricted in these molecules. Despite a certain rotational and conformational flexibility, the orientations of the spin labels do not significantly deviate from their minimal energy conformation. This orientation selection can be deduced from the experimental PELDOR time traces by applying the above proposed deconvolution methods to determine the orientation intensity function. To this end, the following strategy is employed. First, the distance distribution $f(r)$ is estimated by DeerAnalysis.[143,144] In this first step, possible angular

correlation effects are disregarded by using the average $S(t,\nu_A,\nu_B)=\sum_i S(t,\Delta\nu_{AB_i})$ over all offset frequencies $\Delta\nu_{AB}$ as input data in the Tikhonov regularization. Figure 16b shows the resulting spin label distance distribution for compounds **1** and **2**.

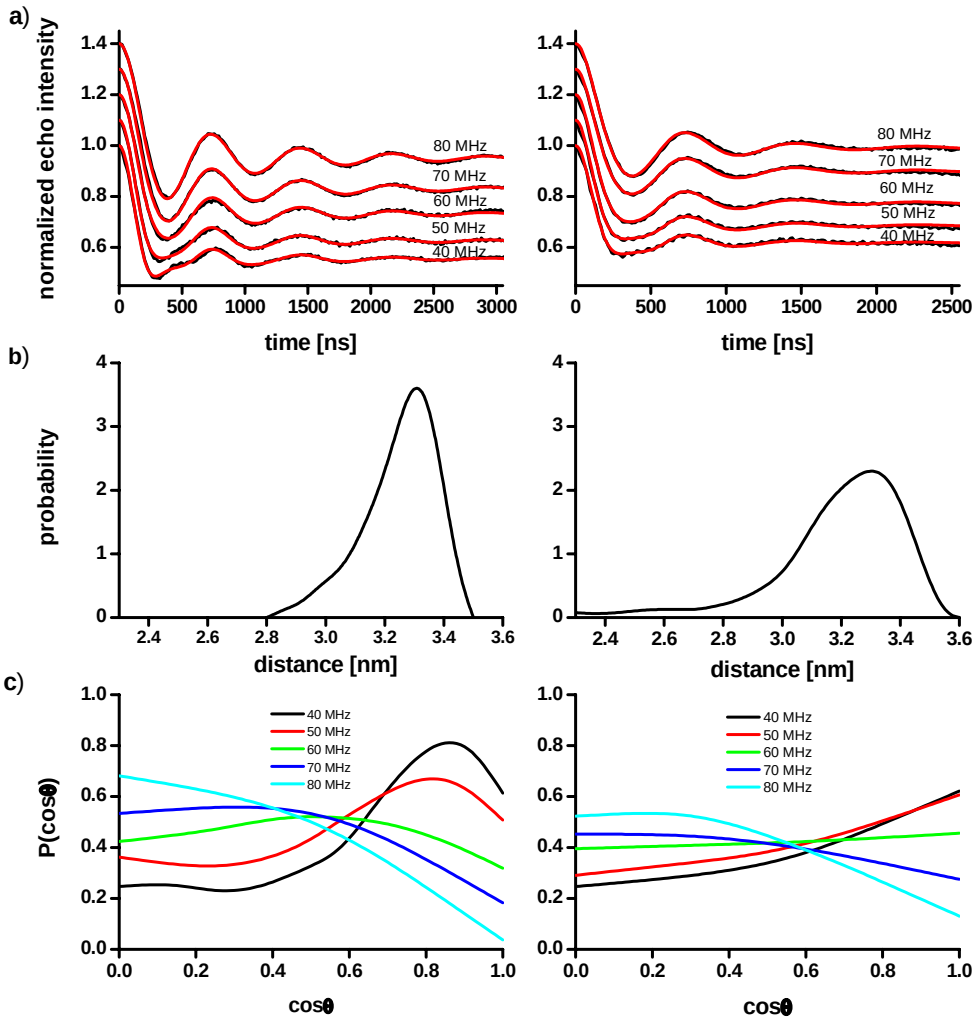

***Figure 16*:** Analysis of the PELDOR measurements obtained for compound **1** (left panels) and compound **2** (right panels). a) Comparison of measured (black lines) and reconstructed (red lines) PELDOR time traces. For convenient presentation, the signals obtained for the offsets 50, 60, 70, and 80 MHz were shifted by 0.1, 0.2, 0.3, and 0.4, respectively. b) Distribution of the spin label distances, obtained from DeerAnalysis[143,144]of the averaged time traces (see text). c) Orientation intensity functions obtained by the Tikhonov regularization, assuming the distance distribution shown in panel b.

As already anticipated in the discussion of the time traces, the peak of the distribution is located at 3.3 nm for both molecules, while its width is larger for compound **2** than for compound **1**. In a second step, the convolution expression (eq. 55) is employed to determine the orientation intensity function $P'(\Delta\nu_{\mathrm{AB}},\theta_{\mathrm{dip}})$ from the experimental data

via Tikhonov regularization. The resulting functions $P'\left(\Delta\nu_{\mathrm{AB}},\theta_{\mathrm{dip}}\right)$ obtained for compounds **1** and **2** are displayed in Figure 16c. Using these functions in combination with the distance distribution shown in Figure 16b, the PELDOR signals can be recalculated. As shown in Figure 16a, recalculated and original PELDOR time traces are in absolute agreement, thus demonstrating the internal consistency of the method. Several technical issues should be mentioned at this point. First, it is to be noted that the second step of the procedure [i.e., the evaluation of eq. 60] requires to choose the regularization parameter α. Usually, the *L*-curve method[145] is used to determine α. However, it was found that in this case the parametric plot of the deviation of the regularized signal from the experimental data versus the smoothness in logarithmic scale does not yield curves with a pronounced *L*-shape. Therefore, the regularization parameter is estimated by setting a limit ε for the deviation between measured and regularized time traces. The parameter ε can be estimated from the level of noise and the inaccuracy caused by the elimination of the intermolecular relaxation contribution. For example, if the uniform noise level is 1%, then the logarithm of the averaged squared deviation between experiment and regularized signal is equal to $\varepsilon = \log_{10}\left(\frac{1}{3}\cdot 0.01^2\right) = -4.47$. Having determined ε, eq. 60 is solved with the largest overall parameter α. Setting the deviation limit to $\varepsilon = -4.47$ for molecule **1** the regularization parameters $\alpha = 3^2, 3^3, 3^5, 3^7$ and 3^7 for the frequency offsets 40, 50, 60, 70, and 80 MHz, respectively are obtained. Similarly, for molecule **2** the values 3^5, 3^5, 3^{10}, 3^8, and 3^8 are gathered. As the calculation of the regularization parameters is rather approximate, it is reassuring to know that the procedure depends only weakly on the exact choice of α. In all cases considered, the PELDOR time traces are of similar nature, even if the smallest or largest considered value of α is employed.

Furthermore, problems regarding the Tikhonov regularization may arise if the underlying distributions of distance and orientations are not smooth, single peaked functions, but exhibit several, possibly sharp, maxima. This is because the Fredholm integral equation of the first kind eq. 55 is an ill-posed problem, implying that some columns of the kernel matrix $K_{ij} = \left\langle \cos\left(\frac{D_{dip}}{r^3}\left(1-3\cos^2\theta_{dip_j}\right)t_i\right)\right\rangle$ can be nearly linearly dependent, which makes the computed solutions potentially sensitive to small

perturbations of the data. For example, one may find that $K_{ij} \approx K_{ij'}$ for all times t_i, even if the corresponding values for $\cos\theta_{dip\,j}$ and $\cos\theta_{dip\,j'}$ are not similar. (Note that $K\left(\cos\theta_{dip}, t\right)$ exhibits the same values in the intervals $\cos\theta_{dip} \in \left[0, \sqrt{1/3}\right]$ and $\cos\theta_{dip} \in \left[\sqrt{1/3}, \sqrt{2/3}\right]$.) Practice has shown so far, however, that orientation intensity functions are usually rather smooth. A final note of caution is to mention that the usual subtraction of intermolecular relaxation from the measured PELDOR time traces may be problematic if the intermolecular decay is non-exponential or in case the PELDOR oscillations exceed the observation time window.

6.2.5 Calculation of PELDOR Signals with MD Based Conformers

The PELDOR time traces from MD generated conformers for both molecular systems are shown in Figure 17.

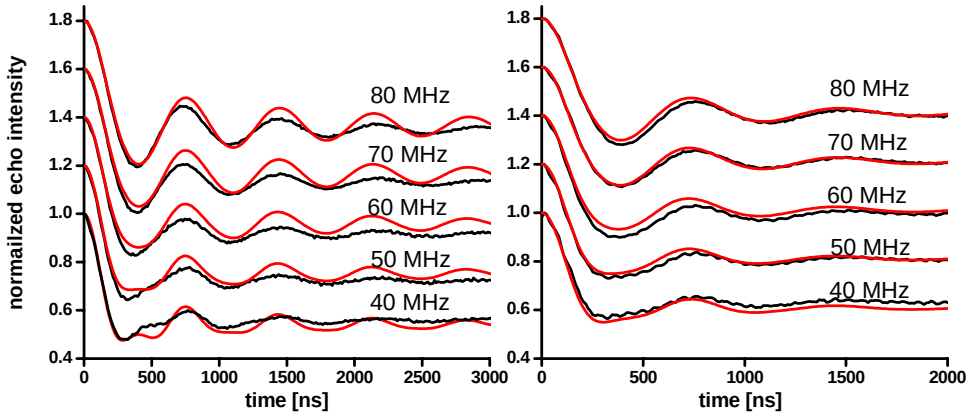

***Figure 17*:** Comparison of measured (black lines) and MD simulated (red lines) PELDOR time traces obtained for compound **1** (left) and compound **2** (right).

Considering the fact that parameters were not adjusted, the overall agreement between theory and experiment is remarkable. In the case of the bent system **2**, the MD results match the experimental signals almost quantitatively. In the case of the linear system **1**, the frequency of the oscillations is reproduced faithfully, while the simulations somewhat underestimate the overall damping of the experimental signal. The latter finding already indicates that the width of the inter-spin distance distribution is

somewhat too small in the MD description of system **1**. Indeed, the comparison of distance distributions extracted from experimental time traces and from MD simulations in Figure 18 reconfirms this finding and also shows that both mean values and the distance distribution of system **2** are reproduced very well. Figure 18 also shows a comparison for the orientation intensity functions from both methods. Again, an almost quantitative agreement is found in the case of the bent system **2**. The calculated intensity functions of the linear system **1**, on the other hand, agree only well with experiment at high frequency offsets (60–80 MHz), but deteriorate at low offsets (40–50 MHz). Assuming that the proposed Tikhonov regularization procedure works well for this simple example, the deviations between theory and experiment are most likely caused by inaccuracies of the empirical force field. Furthermore, it should be kept in mind that the initial assumption is that the thermal distribution of conformational states (as seen in MD simulations) is preserved in a PELDOR experiment using a frozen sample.[104] Having validated the MD results by comparison to the experiment, the predicted orientational distribution of the spin labels can be investigated. To this end, the angle $\varphi \equiv \arccos\left(\mathbf{x}_i \cdot \mathbf{r}\right)$ describing the relative orientation of the two labels is considered first. As may be expected, the angle φ is uniformly distributed, which reflects the almost free rotation of the nitroxides around their connecting bond axes.

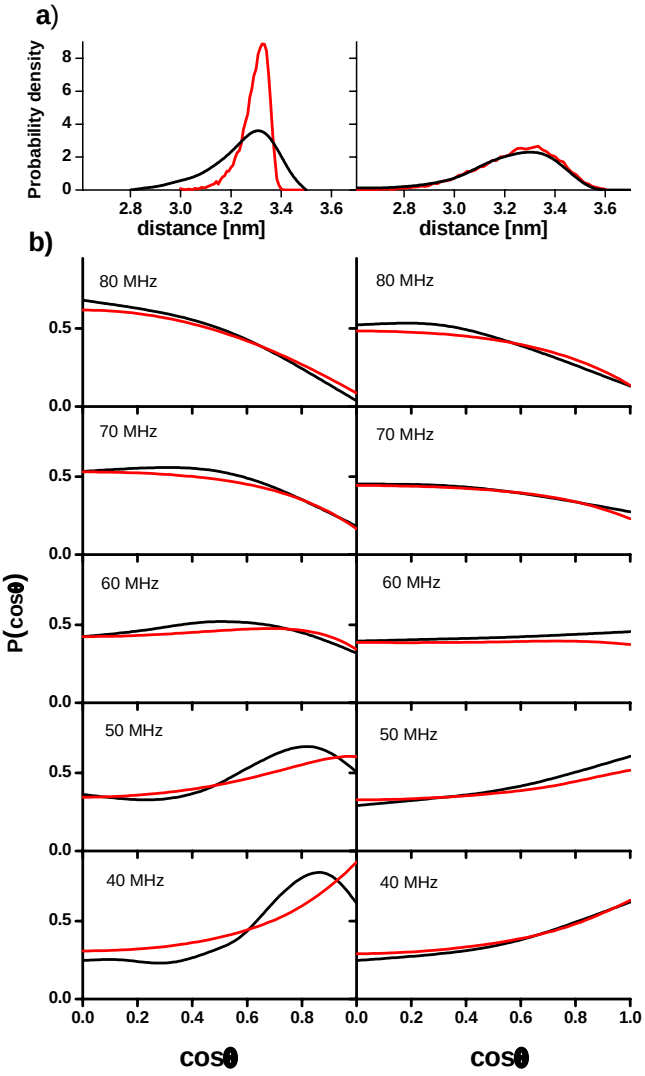

***Figure 18*:** a) Distributions of spin label distances and b) orientational intensity functions as obtained for **1** (left panels) and **2** (right panels). Compared are experimental results from a Tikhonov regularization (black lines) and calculated results from a MD simulation (red lines).

Next two angles describing the relative orientation of the labels and the dipolar vector ***r***, that is, $\beta_i \equiv \arccos\left(\cos\theta_{dip,i} \cdot \mathbf{r}\right)$ and $\delta i \equiv \arccos\left(\mathbf{x}_i \cdot \mathbf{r}\right)$ with i = 1, 2 (see Figure 19) are considered. The distributions of these angles are shown in Figure 19. For both molecular systems, $\beta_i = 90° \pm 30°$ i.e., on average the normal of the radical plane, $\cos\theta_{dip,i}$, is perpendicular to the connecting dipolar vector ***r***. The angle δ_i between the NO axis of the label and the dipolar vector, on the other hand, exhibits a mean value of ~ 140° for **1**. As expected from their molecular structures, the bent system **2** shows a larger fluctuations of the angle δ_l than the molecule **1**, due to the free rotation of the nitroxides.

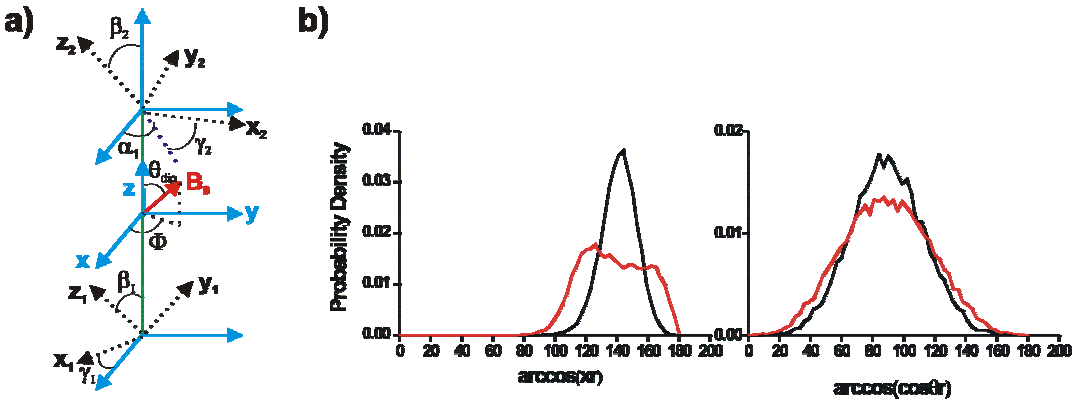

***Figure 19*:** a) The three used coordinate systems: the dipolar coordinate system (blue) $\{\vec{x},\vec{y},\vec{z}\}$ whose *z*-axis coincides with the inter-spin vector $\vec{r}$ (green), and the principal coordinate systems $\{\vec{x}_1,\vec{y}_1,\vec{z}_1\}$ and $\{\vec{x}_2,\vec{y}_2,\vec{z}_2\}$ of the first and second nitroxide radicals (black), respectively. The orientation of the two radicals is described by the Euler angles $(\alpha_1,\beta_1,\gamma_1)\equiv o_1$ and $(\alpha_2,\beta_2,\gamma_2)\equiv o_2$. Angles θ and Φ define the direction of the magnetic field $\vec{B}_0$ (red). b) MD simulation results for the orientation distribution of the spin labels in the linear (black lines) and bent (red lines) biradicals **1** and **2**. Shown are the distributions of (left) the angle between the dipolar vector *r* and the normal of the radical plane z_i and (right) the angle between *r* and the NO axis of the spin label.

6.2.6 Discussion and Conclusion

Ansatz 55 for the PELDOR signals allows obtaining both distance information [i.e., the distribution *f*(*r*)] and orientational information [i.e., the function $P'(\Delta\nu_{AB},\theta_{dip})$] from a PELDOR experiment. Adopting various polynomials as orientation intensity functions, the internal consistency of this approach is shown, that is, recalculated and original PELDOR time traces are in good agreement (see Figure 16). Furthermore, it is demonstrated that PELDOR signals, distance distributions, and orientational intensity functions obtained from the experimental data of small nitroxide biradicals and from MD simulations agree quite well (see Figures 15 and 16). The differences between the results obtained by both methods are surprisingly small, taking into account that the MD studies are performed in liquid water solution at room temperature, whereas PELDOR experiments were performed in frozen solution samples in *ortho*-terphenyl at 40 K. The observed differences might also be due to the limitations of both methods. On one hand, the precision of the Tikhonov regularization can be enhanced by an improved choice of the regularization parameter. On the other hand, MD simulation results can be enhanced by a more

accurate determination of empirical force fields. An analysis of the MD trajectories has revealed that:

1. the spin labels rotate freely around their connecting bond axes,
2. the normal of the radical planes is on average perpendicular to the connecting dipolar vector, and
3. the angle between the NO axis of the labels and the dipolar vector is on average ~ 140° for compound **1** whereas it is more or less uniformly distributed in the interval (110°,170°) for the compound **2** (see Figure 19).

At this point, the question arises to what extent this orientational information can also be inferred directly from the PELDOR experiments, i.e., by analysis of the orientational intensity functions $P'\left(\Delta\nu_{\mathrm{AB}},\theta_{\mathrm{dip}}\right)$. Generally speaking, all curves $P'\left(\Delta\nu_{\mathrm{AB}},\theta_{\mathrm{dip}}\right)$ as shown in Figure 18b are relatively flat for $0\le\cos\theta_{dip}\le 0.5$, although their levels are gradually increased for larger frequency offsets $\Delta\nu_{AB}$. That is, all molecules are similarly excited for small values of $\cos\theta_{dip}$, i.e., for angles $\theta_{dip}\equiv\arccos\left(\mathbf{r}\cdot\mathbf{B}_0\right)\approx 90°\ \left(\mathbf{r}\perp\mathbf{B}_0\right)$. For large values of $\cos\theta_{dip}$ corresponding to $\theta_{dip}\approx 0°\ \left(\mathbf{r}\,||\,\mathbf{B}_0\right)$ a strong intensity at small frequency offsets and a weak intensity at large offset frequencies is observed. To relate this finding to the underlying structure of the molecules, one has to recall that for small frequency offsets $\cos\theta_{dip_i}$ is preferentially perpendicular to $\mathbf{B}_0$. Assuming that $\cos\theta_{dip_i}\perp\mathbf{r}$, biradicals with both $\mathbf{r}\perp\mathbf{B}_0$ and $\mathbf{r}\,||\,\mathbf{B}_0$ can be excited, i.e., $P'\left(\Delta\nu_{\mathrm{AB}},\theta_{\mathrm{dip}}\right)$ has nonzero values for all $0\le\cos\theta_{dip}\le 1$. For large frequency offsets, on the other hand, $\cos\theta_{dip_i}\,||\,\mathbf{B}_0$ is found. In this case, only biradicals with $\mathbf{r}\perp\mathbf{B}_0$ can be excited, i.e., $P'\left(\Delta\nu_{\mathrm{AB}},\theta_{\mathrm{dip}}\right)$ vanishes for $\cos\theta_{dip}\approx 1$. In particular, for molecule **1** these structural constraints can be predicted from the orientational function $P'\left(\Delta\nu_{\mathrm{AB}},\theta_{\mathrm{dip}}\right)$. To summarize, this work shows that the possibility to separate the distance distribution function $f(r)$ from an intensity function $P'\left(\Delta\nu_{\mathrm{AB}},\theta_{\mathrm{dip}}\right)$ which only contains orientational information. The latter function has a clear physical meaning, as it reflects the PELDOR intensities

from molecules with different orientations in the external magnetic field. Dependence of function $P'\left(\Delta\nu_{\mathrm{AB}},\theta_{\mathrm{dip}}\right)$ on the detection pulse frequency offset $\Delta\nu_{AB}$ can be considered as a spectrum, which is determined by the orientations of the spin labels and vector ***r***. The orientation intensity function is directly obtained from the experimental data and its calculation is easier than the calculation of PELDOR time traces based on MD trajectories. Therefore, the function $P'\left(\Delta\nu_{\mathrm{AB}},\theta_{\mathrm{dip}}\right)$ can be conveniently used for the comparison of MD studies with experiments. Here, the intensity function obtained from PELDOR experiments by Tikhonov regularization are compared to intensity function calculated from MD simulations model dinitroxide compounds **1** and **2** and excellent agreement was achieved in both cases. The orientational information does not only yield the structure of the molecule but is also essential for a quantitative analysis of the molecular dynamics encoded in the attenuation of the PELDOR signal. Applications of this approach to biological macromolecules and a quantitative determination of the polar angle of the dipolar vector ***r*** in the nitroxide molecular axis system using detection pulse frequency dependence of the function $P'\left(\Delta\nu_{\mathrm{AB}},\theta_{\mathrm{dip}}\right)$ are currently in progress. First results are briefly sketched in Section 6.3.4.

6.3 Application of Orientation Selective PELDOR Measurements to DNA

The last two chapters concerned the analysis of orientation selective PELDOR data gained from organic model systems. Here, an application to DNA molecules is described as published in *Angewandte Chemie,* **121**, 3342, 2009. It is entitled: "Relative orientation of rigid nitroxides by PELDOR: Beyond distance measurements in nucleic acids."[147]
The author contributed all experimental PELDOR spectra as well as the respective simulations and their interpretation.

6.3.1 Abstract

Detection frequency offset ($\Delta\nu_{AB}$) dependent PELDOR measurements were performed at common X-Band frequency on two spin labeled DNA molecules and one organic model compound using the rigid nitroxide spin label **Ç**. In addition to the distance, the simulation of the respective experiments yielded angle φ between the *z*-component of the ^{14}N-hyperfine coupling tensor (A_{zz}) and the spin-spin distance vector *r* with high precision. This procedure allows to gain insight into the structure of biomolecules.

6.3.2 Introduction

In addition to distances, the angular dependence $\left(1-3\cos^2\theta_{dip}\right)$ of the dipole–dipole interaction provides the possibility to unravel the relative orientation of spin labels, thus yielding considerably more structural information. For example, continuous wave (cw) EPR spectroscopy has been utilized to obtain relative orientations of spin-labeled cofactors,[148] and more recently, PELDOR experiments at high frequencies have disentangled the orientation between protein-bound radical cofactors[149] or radical-containing amino acids.[43] These studies benefited from the immobilization of the free radical in the rigid protein scaffold, whereas orientation studies using spin labels are hampered by the flexibility of most labels.[45] This limitation can be overcome by using rigid spin labels like the recently described spin label **Ç**, in which

a nitroxide was incorporated into a polycyclic fused ring system of a cytidine analogue that forms a base pair with guanine (see Figure 20).[19]

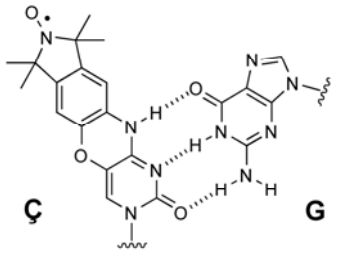

***Figure 20*:** Spin label **Ç** base-paired to G.

Ç enables grafting a rigid nitroxide onto chosen sites in nucleic acids and the preparation of samples with specific, fixed orientations of spin labels relative to the framework of the nucleic acid. Here, it is shown that this new generation of spin labels allows determination of both distance and the orientation of the two labels in DNA.

6.3.3 Results and Discussion

Two **Ç**-spin-labeled DNA duplexes, **DNA I** and **DNA II**, were designed for a proof-of-principle experiment (see Figure 21a, b). Molecular modeling shows that **Ç** is projected into the major groove of the DNA helix[19] and thermal denaturation studies have demonstrated that **Ç** does not appreciably affect the stability of DNA duplexes.[150] The distance and relative orientation of the spin labels differs in both DNAs: r = 3.7 and 2.1 nm whereas φ = 5 and 45° for **DNA I** and **DNA II**, respectively. φ is defined here as the angle between the z-component of the ^{14}N-hyperfine coupling tensor (A_{zz}) and r. Due to geometry constraints, a DNA sample in which φ = 90° could not be prepared. To circumvent this constraint, biradical **I** (see Figure 21c), in which the distance between the spin centers is 2.7 nm and φ equals 90° was synthesized.

The synthesis of **Ç** and its incorporation into DNA was performed as described earlier.[19,150] PELDOR experiments were performed on all three molecules with the 4-pulse sequence depicted in Figure 8.[53,111,112] The 12 ns pump pulse at microwave frequency ν_B was placed on the maximum of the nitroxide spectrum, thus exciting all

orientations (see Figure 22b). The detection pulses are applied at microwave frequency ν_A with a frequency offset $\Delta\nu_{AB} = \nu_A - \nu_B$ of 40 to 90 MHz (see Figure 22a).

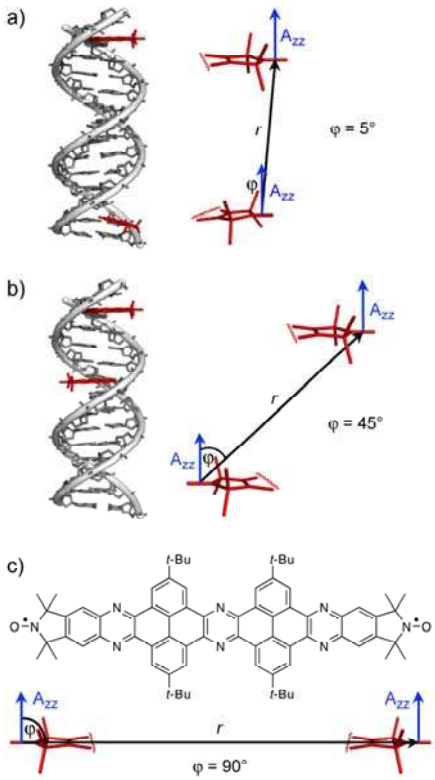

***Figure 21*: a, b) **DNA I** and **DNA II**, respectively, with the spin label **Ç** highlighted in red and simplified schematic structures showing the orientation of A_{zz} with respect to *r*. c) Structure of **I** and a simplified scheme of the orientation of A_{zz} with respect to *r*.**

The detection sequence consisting out of three pulses each with a length of 32 ns has an excitation bandwidth of 26 MHz[151] and, therefore, excites only a fraction of the nitroxide spectrum. For comparison, the nitroxide spectrum, which is at X-band frequencies dominated by the anisotropic ^{14}N-hyperfine coupling tensor $A(^{14}N)$ [A_{zz} = 34G, A_{yy} = 5G, A_{xx} = 6.5G], has a width of about 210 MHz. Thus, varying the position of the detection pulse, causes a selection of different components of $A(^{14}N)$. With $\Delta\nu_{AB}$ = 90 MHz, the detection pulses are placed on the low-field edge of the X-band EPR spectrum, selecting mainly A_{zz} (see Figure 22c). Decreasing $\Delta\nu_{AB}$ in 10 MHz steps down to 40 MHz leads to a deselection of A_{zz} and an increasing contribution of A_{xx}, A_{yy} and off-diagonal components (see Figure 22d). Importantly, the orientation of the nitrogen hyperfine tensor is fixed with respect to *r* as the nitroxides in **DNA I**, **DNA II** and **I**, are geometrically rigid.

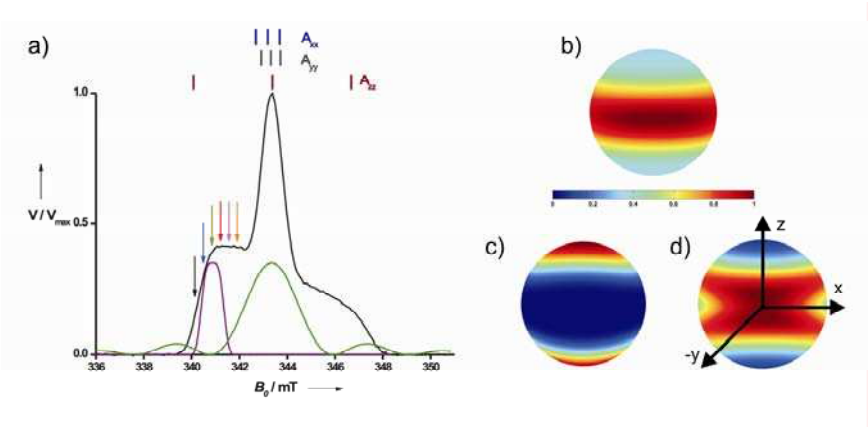

***Figure 22*: a) Field swept EPR spectrum of **DNA I** at 40 K with the excitation profiles of the observer pulses (purple) and pump pulse (olive) and the corresponding ^{14}N stick spectrum. Arrows indicate observer pulse positions varying from $\Delta\nu_{AB}$ = 40 MHz (orange) to 90 MHz (black). b) Excited orientations for the pump pulse and c) the detection sequence for $\Delta\nu_{AB}$ = 90 MHz and d) 40 MHz.**

Thus, selecting specific components of A selects at the same time specific components of the dipolar distance vector, depending on the molecular geometry. In the case of **I**, the selection of A_{zz} for $\Delta\nu_{AB}$ = 90 MHz leads to a selection of those molecules with the distance vector r perpendicular to B_0 (θ_{dip} = 90°) since A_{zz} is fixed perpendicular to ***r*** (φ = 90°). Decreasing $\Delta\nu_{AB}$ in 10 MHz steps excites more of A_{xx} and A_{yy} and less of A_{zz}, where A_{yy} is again perpendicular to r, but A_{xx} is parallel. Therefore, at smaller frequency offsets, the parallel component of the dipolar distance tensor (θ_{dip} = 0°) should contribute more to the PELDOR spectrum. This is exactly what is observed within the PELDOR time traces and the Fourier transformed spectra for **1** (see Figure 23g, i). In the case of **DNA I**, the geometry is such that A_{zz} is nearly parallel (φ = 5°) and A_{xx} perpendicular to r. Compared to **I**, one should expect the opposite trend in the PELDOR spectra. For $\Delta\nu_{AB}$ = 90 MHz, the parallel component of the dipolar distance tensor (θ_{dip} = 0°) should dominate and the perpendicular component should increase with decreasing $\Delta\nu_{AB}$. This is in full accordance with the experiment (see Figure 23a, c). For the intermediate case of **DNA II**, where φ = 45°, neither of the Pake pattern singularities at θ_{dip} = 0° or θ_{dip} = 90° can be selected without large contributions from the other orientations (see Figure 23d, f). A qualitative estimation of φ can thus be easily performed on the basis of the experimental data. If φ is close to 0°, as in **DNA I**, the parallel component of the Pake pattern (θ_{dip} = 0°) increases by varying $\Delta\nu_{AB}$ from 40 to 90 MHz, whereas it decreases if φ is about 90°, as in **I**. In cases of φ around 45°, as in **DNA II,** the shape of the Pake pattern remains constant with $\Delta\nu_{AB}$ - variation (see Figure 23c, f, i).

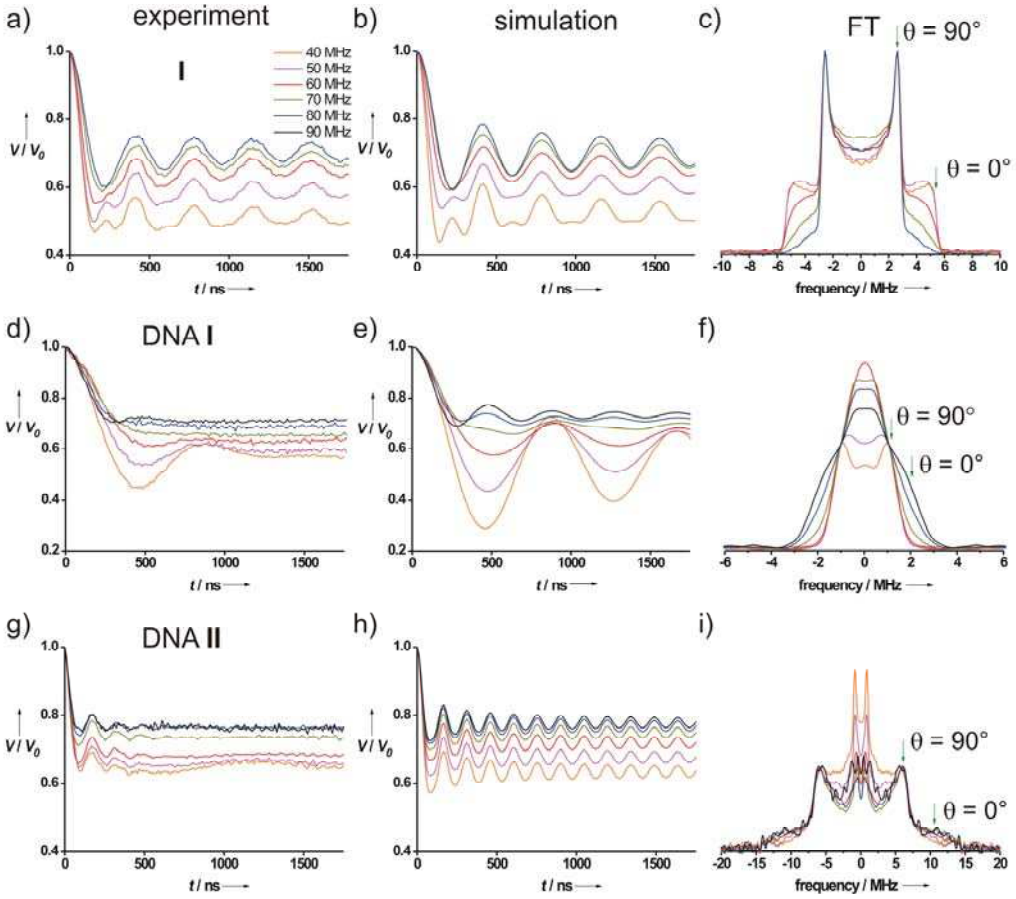

Figure 23: PELDOR data. a), d), g) PELDOR time traces recorded with $\Delta\nu_{AB}$ -values ranging from 40 to 90 MHz for **DNA I**, **DNA II** and **I**, respectively. b), e), h) Simulated PELDOR time traces for **DNA I**, **DNA II** and **I**, respectively. c), f), i) Fourier Transformations of the experimental PELDOR time traces. The peak at about 1 MHz in the Fourier Transformation of **DNA II** is attributed to end-to-end stacking of two DNAs.

This qualitative analysis of orientations requires, however, two coplanar spin labels. With respect to distances, a variation of $\Delta\nu_{AB}$ enables one to detect both singularities of the Pake pattern in all three cases and thus to easily calculate the distance by using the frequency corresponding to θ_{dip} = 90°. This frequency amounts to 2.7 MHz, 1.0 MHz and 6.0 MHz for **I**, **DNA I** and **DNA II**, respectively and thus distances of 2.7 nm, 3.7 nm and 2.1 nm can be extracted, respectively. All distances are in very good agreement with those gathered from molecular modeling (see Table 1).

A more quantitative analysis was performed for all three molecules by simulations (see Figure 23b, e, h) using PESIM. These simulations give an excellent fit to the experiment with respect to frequency and modulation depth variation with $\Delta\nu_{AB}$ using the angles given in Table 1 and prove at the same time that the observed effects are caused by orientation selection and are not due to pulse overlap or experimental artifacts.

molecule	*PELDOR r[a] [nm]*	*modeled r [nm]*	*φ [°]*
I	*2.7 (0.1)*	*2.6*	*90 (10)*
DNA I	*3.7 (0.1)*	*3.8*	*5 (15)*
DNA II	*2.1 (0.1)*	*2.1*	*45 (15)*

Table 1: Experimental and modeled distances and φ-values. [a]The numbers in brackets are the errors.

6.3.4 Conclusion and Outlook

In summary, the parameter free extraction of distances and relative orientations of spin centers in nucleic acids can be achieved via orientation selective PELDOR spectroscopy at common X-band frequencies. These studies lay the groundwork for the analysis of large biomacromolecular complexes.

Dr. Andriy Marko, Johann Wolfgang Goethe-University, is now establishing a numerical method to directly extract φ from such PELDOR data sets without simulations or *a priori* structural knowledge. Here, studied DNAs range from **DNA II** with 5 intervening base pairs (ibp) in one ibp steps to **DNA I** (12 ibp) to a maximum of 15 ibp. Preliminary results are shown in Figure 24. Further details of the underlying mathematical algorithm will be published in due course.

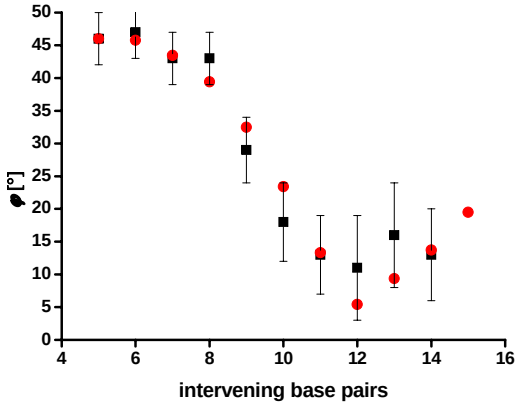

***Figure 24*:** Preliminary results of the numbers of intervening DNA base pairs extracted utilizing a numerical approach (black) in comparison to literature values (red).

Another manuscript currently in preparation attributes the experimentally observed faster damping of the oscillation for **DNA I** and **DNA II** as compared to simulations using one conformer (see Figure 23) to conformational flexibility.

In literature a description of overall DNA flexibility via a cooperative twist-stretch motion was already indirectly postulated from single molecule[152,153] or rotor bead tracking experiments.[154] Lately, small-angle X-ray scattering interference between gold nano-crystal labels deduced a quadratic dependence of the B-DNA end-to-end length variance, σ_z^2, on the number of base pairs, n, as $\sigma_z^2 = 0.0041 \bullet n^2$.[155]

Dr. Andriy Marko translated this experimental observation into a geometric model of DNA radial "breathing". An alteration of the helix radius, 5.8 Å ± 0.65 Å, with a constant helical pitch will effect the end-to-end distance, the distance between the nitroxide labels and their mutual orientation (twist-stretch mode). Quantitative simulations of multi-frequency PELDOR data with a single set of dynamical parameters (see Figure 25) allowed a detailed identification of this cooperative and correlated twist-stretch motion of DNAs.

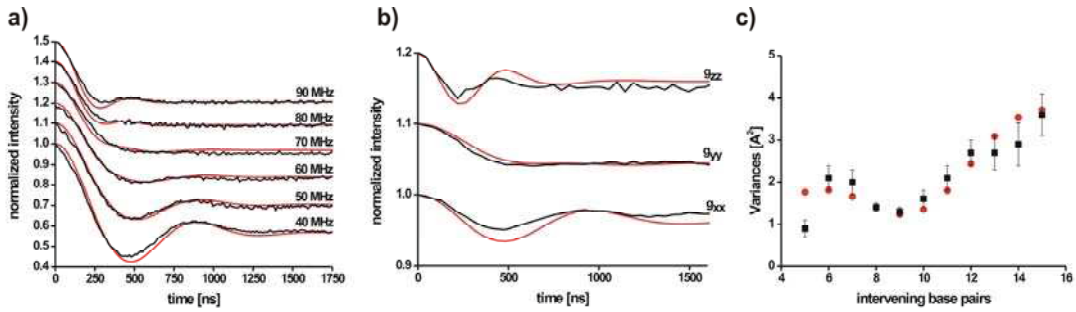

Figure 25**:** a) experimental (black) and simulated (red) X-Band PELDOR time domain signals of **DNA I** recorded at various spectral positions. b) experimental (black) and simulated (red) G-Band PELDOR time domain signals recorded at various spectral positions by Dr. Vasyl Denysenkov for **DNA I**. c) distance variances extracted based on the geometric assumption of radial "breathing" (red) in comparison to the experimental values (black).

6.4 Disentangling Exchange and Dipolar Coupling

This chapter has been published in the journal *Physical Chemistry Chemical Physics*, 2009, DOI:10.1039/ B905524J.[156] It discusses the analysis of PELDOR data in presence of a non-zero exchange coupling *J* and is entitled "Ferro- And Antiferromagnetic Exchange Coupling Constants in PELDOR Spectra".
The author contributed sample preparation including purification via recrystallization, all experimental PELDOR time traces as well as their according simulations and interpretation. Synthesis was performed by collaborators Dr. Pavol Cekan and Prof. Dr. Snorri Th. Sigurdsson, University of Iceland.

6.4.1 Abstract

It is demonstrated on three rigid and conjugated biradicals how the presence of an exchange coupling constant *J* and its distribution ΔJ influences PELDOR data and its analysis. In principle two combinations of *J* and *D* (see equation 50), fulfill the experimental data in each case. The correct one, including the sign of *J*, can be determined via simulations in case the two halves of the dipolar tensor are separated enough.

6.4.2 Introduction

In order to investigate the effect of the sign and magnitude of *J* on PELDOR data and its analysis in more detail, biradical **I**[147] as well as two novel organic biradicals **II** and **III** (see Scheme 6) using the same nitroxide as in Section 6.3. To allow for antiferromagnetic and ferromagnetic exchange coupling, the two spin centers were connected via rigid and conjugated bridges, but with different substitution patterns.

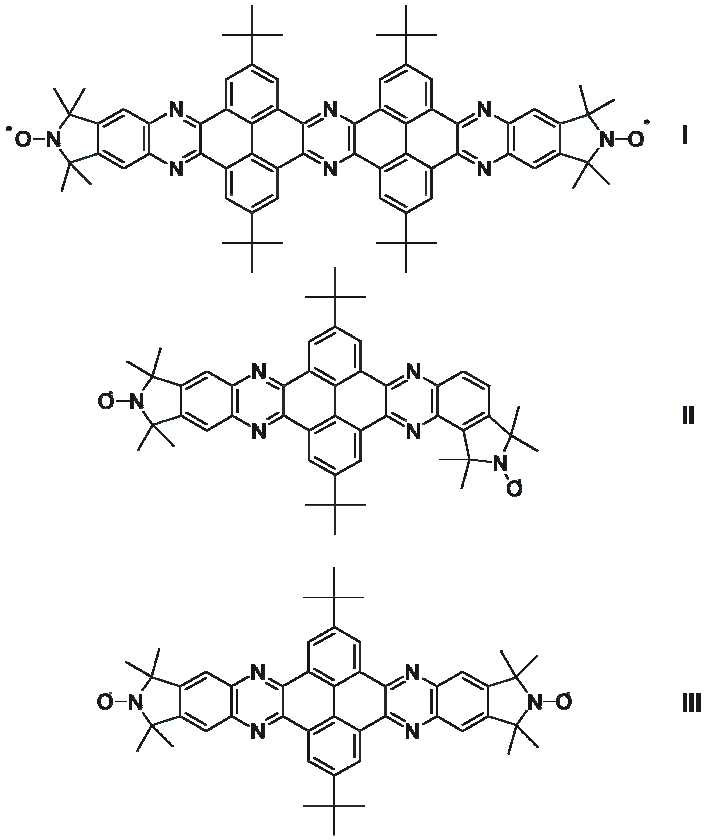

***Scheme 6**:* Nitroxide model systems used in this study

Modeling molecules **I** - **III** using a standard molecular modeling routine yielded the intramolecular spin-spin distances given in Table 2.

molecule	r_{MM} [Å][a]	r_{exp} [Å][b,d]	φ[°][b]	*J [MHz]*[b]	*ΔJ [MHz]*[b]
I	26.5	26.9(1)	90(15)[c]	0.0(1)	0.0(1)
II	18.5	18.2(4)	90(15)	-3.2(6)	±0.8(3)
III	20.1	19.9(4)	----[e]	+2.5(5)	±1.7(4)

a Measured as the average over the N-to-N and O-to-O distances.
b The number in brackets indicates the error in the last digits.
c The error is given in the previous chapter and is assumed to be the same for **II**.
d The error in r states an observable difference in the frequency.
e In this case φ cannot be determined from the PELDOR data (see text).

Table 2: Geometric and exchange coupling parameters for **I** – **III** as determined from simulating the PELDOR time traces using the values from the Fourier transformed spectra as initial guesses. r_{MM} is the distance derived from molecular mechanics simulations.

6.4.3 Results and Discussion

The presence of the nitroxide functional group in all three compounds was verified via cw X-band EPR measurements at 294 K. The typical nitroxide radical spectra are depicted in Figure 26 a), b), c). None of the spectra exhibits a splitting as anticipated for the expected small exchange coupling constants *J*. However, **II** and **III** reveal, compared to reference system **I**, a line-broadening of 0.4 G and 0.3 G for the central $m_I = 0$ transition, respectively, which is attributed to the presence of a weak exchange coupling.

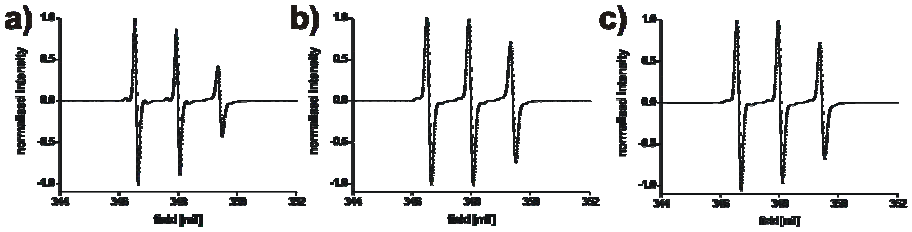

***Figure 26*:** cw X-band EPR spectra of a) **I**, b) **II** and c) **III** recorded at room temperature.

In contrast to frozen solution cw EPR spectra, where the resolution of dipolar coupling is limited by the inhomogeneous line width, PELDOR recovers the homogeneous line width and allows for the observation of weaker electron-electron interactions. PELDOR time traces of **I** - **III** (see Figure 28) were recorded by placing the 12 ns pump pulse on the maximum of the nitroxide spectrum (see Figure 29a), exciting all orientations of the nitroxide with respect to the external magnetic field (see Figure 29b). For example, commonly applied 32 ns long detection pulses correspond to an excitation bandwidth of 26 MHz, which cause, compared to a width of 210 MHz for the nitroxide field swept spectrum, a selection of spectral components depending on the position of the detection sequence (see Figure 29c, d). Applying the detection pulses on the low-field edge of the spectrum (frequency offset $\Delta\nu_{AB} = \nu_A - \nu_B = +80$ MHz) selects mainly the A_{zz} component of the ^{14}N-hyperfine tensor (see Figure 27c) whereas decreasing $\Delta\nu_{AB}$ in steps of 10 MHz down to 40 MHz leads to an increased contribution of the A_{xx}, A_{yy} and off-diagonal components (see Figure 29d). This translates into an orientation selection within the dipolar Pake pattern due to the rigid molecular frame of **I** – **III** fixing the orientation of the dipolar distance vector *r* with respect to the ^{14}N-hyperfine tensor. Since A_{zz} is fixed perpendicular to *r* in **I** – **III** ($\varphi = 90°$, see Figure 31), the selection of A_{zz} leads for all three molecules to a

selection of the perpendicular component ($\nu_{\perp}$, θ_{dip} = 90°) of the dipolar tensor. In turn, decreasing $\Delta\nu_{AB}$ increases contributions of the parallel component ($\nu_{||}$, θ_{dip} = 0°). This can be followed in the PELDOR time traces of **I** (see Figure 28a) and more clearly in the Fourier transformed spectra (see Figure 28b). The geometric change induced by the different substitution pattern in **II**, affects only the orientation of A_{xx} and A_{yy} with respect to r, which is difficult to resolve at X-band frequencies. Thus, compared to **I**, the same trend regarding the orientation selection is observed in **II** (see Figure 28c, d). It should, however, be noted, that the broad width of this electron-electron coupling tensor resulted in an increase of the video amplifier band width from 25 MHz to 50 MHz and to decreasing the detection pulse lengths from 32 ns to 16 ns in order to circumvent cut-offs by the amplifier and a too narrow excitation band width of the detection pulses, respectively (see Figure 27).

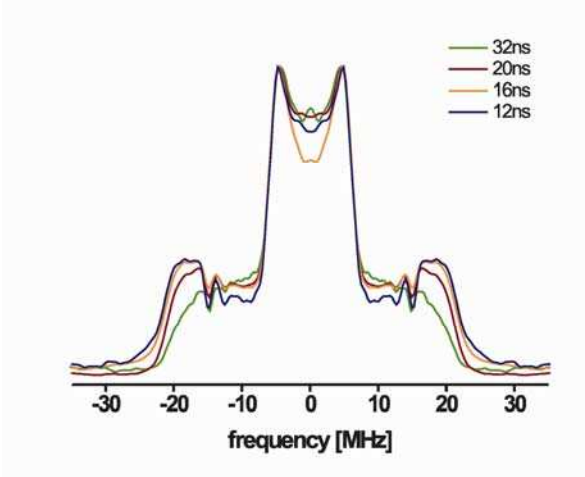

***Figure 27*:** Fourier Transformations of **II** at $\Delta\nu_{AB}$ = 40 MHz for detection pulse lengths of 32 ns, 20 ns, 16 ns and 12 ns in olive, wine, orange and navy, respectively. The shape of the Pake pattern remained constant with a detection pulse length of 16 ns or 12 ns.

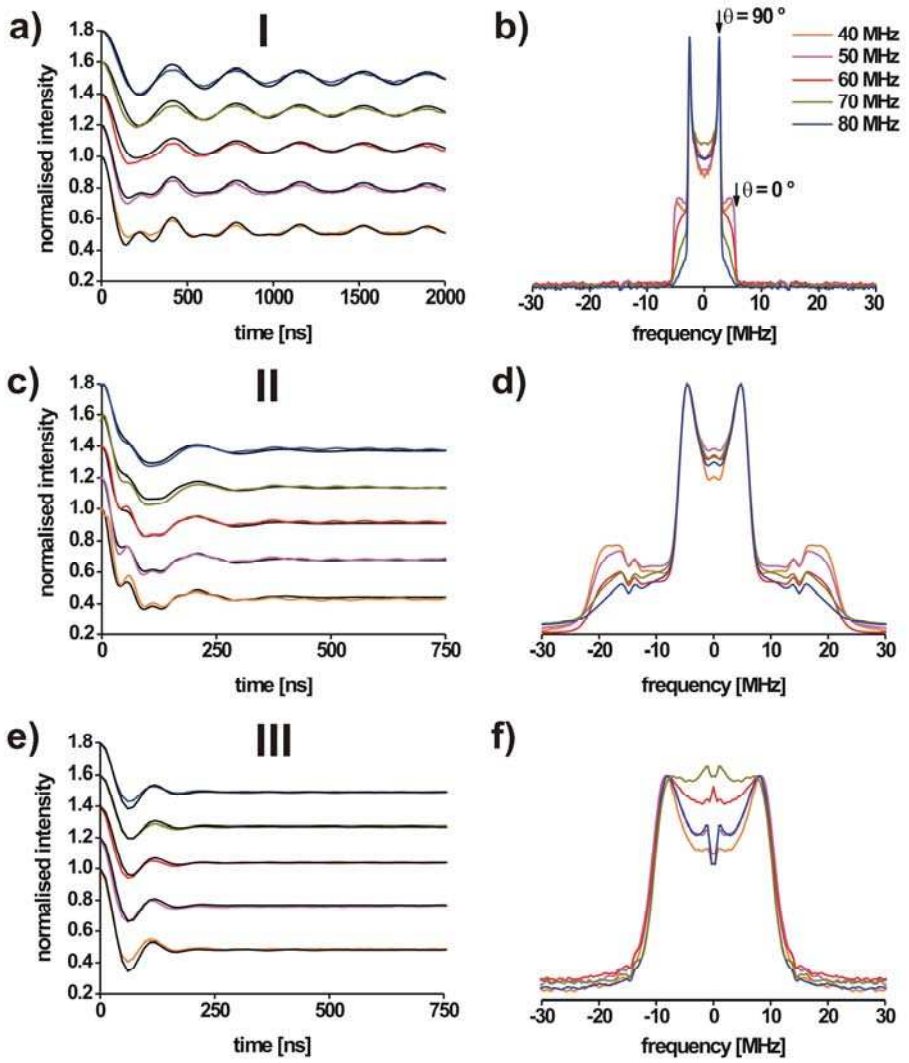

***Figure 28*:** Experimental PELDOR time traces recorded at different detection frequency offsets with simulations (parameters see Table 2) overlaid as black lines for a) **I**, c) **II** and e) **III** shifted along the *y*-axis for better visibility. The corresponding Fourier transformed spectra are depicted in b), d) and f) for **I**, **II** and **III**, respectively. The artifact at ~±14 MHz in panel d) is due to residual proton modulation caused by the short detection pulses.

In addition, the dipolar evolution time increment Δt was reduced from 12 ns to 4 ns to obtain enough data points to clearly resolve a modulation period of ~47 ns corresponding to a $\nu_{\parallel}$ of 22.2 MHz. The pump pulse length of 12 ns, corresponding to an excitation bandwidth of 83 MHz, was short enough to fully excite the electron-electron coupling. In the case of molecule **III** (see Figure 28e, f), the orientation selection effect is less pronounced. The reason is that $\nu_{\parallel}$ coincides with $\nu_{\perp}$, giving the same modulation frequency for either component. This prevents deriving a value for φ from the PELDOR data. The dependence of the modulation depth parameter λ_B on the fraction of molecules and orientations[42] excited can, however, be seen for all three molecules.

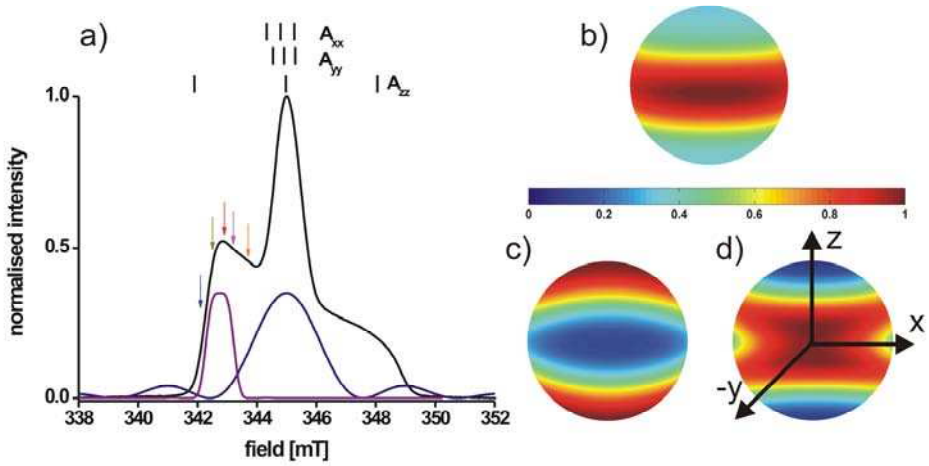

Figure 29: a) Field swept EPR spectrum of **I** at 40 K with the excitation profiles of the observer pulses (purple) and pump pulse (navy) and the corresponding ^{14}N stick spectrum. Arrows indicate observer pulse positions varying from $\Delta\nu_{AB}$ = 40 MHz (orange) to 80 MHz (blue). Excited orientations for b) the pump pulse and for the detection sequence with c) $\Delta\nu_{AB}$ = 80 MHz and d) $\Delta\nu_{AB}$= 40 MHz. The intensities are normalized and color coded, as indicated by the bar in b).

The deepest modulation in each case is achieved for $\Delta\nu_{AB}$ = 40 MHz, corresponding to a spectral position where all dipolar orientations are excited.

$$D[MHz] = \frac{\nu_{\perp} - \nu_{\parallel}}{3} \qquad \text{(eq. 62)}$$

$$J[MHz] = \frac{2\nu_{\perp} + \nu_{\parallel}}{3} \qquad \text{(eq. 63)}$$

Furthermore, the frequencies of the perpendicular and parallel singularities of the Pake pattern of **I** (see Figure 28b) can be read off as $\nu_{\perp}$ = 2.7 MHz and $\nu_{\parallel}$ = -5.4 MHz. Substituting both values into eq. 62 and 63, derived from eq. 50,[44] yields J = 0 MHz and D = 2.7 MHz, which corresponds to an r of 26.8 Å according to eq. 40 and 41. However, the frequency of $\nu_{\perp}$ and $\nu_{\parallel}$ could also be read off as -2.7 MHz and -5.4 MHz, respectively. With these values one derives J = -3.6 MHz and D = 0.9 MHz (r = 38.7 Å). Fitting the time traces with both solutions as initial guesses renders the former one clearly as the correct one (see Figure 30a and Table 1 for parameters). In this case it is easy to discriminate between both solutions since the latter pair with r = 38.7 Å and J = -3.6 MHz shifts the two halves of the Pake pattern far enough apart to create a hole in the spectral intensity around zero frequency which is clearly not present in the experiment. Also note the shift of the frequency in the simulated data due to the absence of the frequencies around zero MHz. The other two possibilities with $\nu_{\parallel}$ = +5.4 MHz and $\nu_{\perp}$ = ±2.7 MHz, can be ruled out on the basis that D has to be

positive. In the case of molecule **II**, the presence of a non-zero *J* can be readily deduced from the broad width of the tensor (see Figure 28d). But also here two pairs of values can be determined for $\nu_{\perp}$ and $\nu_{||}$, +4.6 MHz and -22.2 MHz or -4.6 MHz and -22.2 MHz, respectively.

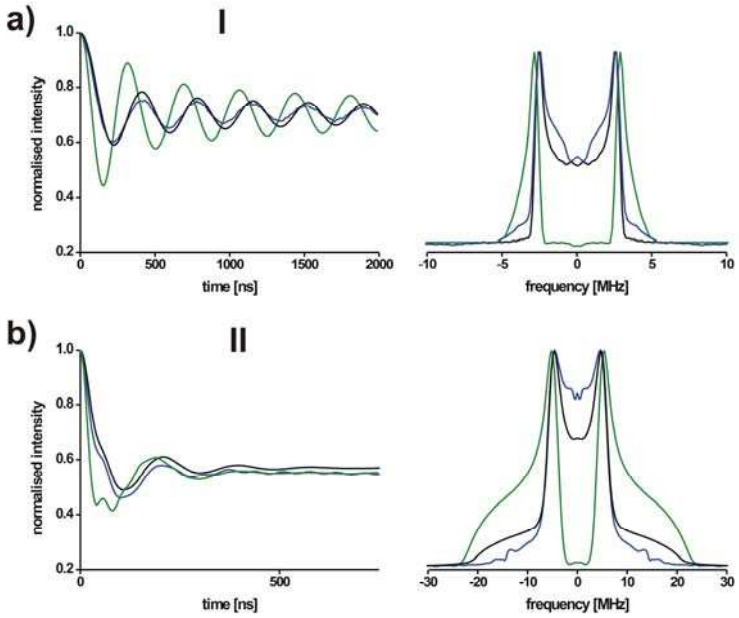

Figure 30: Simulated time traces (see Table 2 for parameters) and FFTs for the two J/r pairs of a) molecule **I** (blue line: experiment; green line, wrong J/r pair with J = -3.6 MHz and r = 38.7 Å; black line, correct J/r pair with J = 0 MHz and D = 2.7 MHz) and b) molecule **II** (blue line: experiment; green line, wrong J/r pair with J = -10.5 MHz and r = 20.7 Å; black line, correct J/r pair with J = -4.3 MHz and r = 18.0 Å). All for a frequency offset $\Delta\nu_{AB}$ = 80 MHz.

The former pair yields *J* = -4.3 MHz and *D* = 8.9 MHz (*r* = 18.0 Å) and the latter *J* = -10.5 MHz and *D* = 5.87 (*r* = 20.7Å). In this case it is already more difficult to select the correct solution, as the simulated time traces (parameters see Table 2) are not too far off the experiment for both pairs (see Figure 30b). Nevertheless, the pair without a hole between the two halves of the Pake pattern gives a better fit to the experiment (fitted values *J* = -3.2 MHz and *r* = 18.2Å). In addition, this value for *r* is closer to the one from the molecular modeling (see Table 2).

The spectrum of **III** (see Figure 28f) can be rationalized as $\nu_{\perp}$ = 8.3 MHz and $\nu_{||}$ = -8.3 MHz or as $\nu_{\perp} = \nu_{||}$. The latter corresponds to a *D* approaching 0 MHz, *r* being very large, and *J* = ±8.3 MHz, which is rather senseless. In the other case, realized in molecule **III**, *r* is 21.1 Å and *J* amounts to +2.8 MHz. Via simulations, it was not possible to differentiate between both solutions. The spectrum cannot be

explained by a complete suppression of $\nu_{||}$ caused by orientation selection, since the variation of $\Delta\nu_{AB}$ enables detecting all orientations as shown in Figure 29c, d.

Independently from the PELDOR data, the cw EPR experiments confirm the presence of a small exchange coupling in molecule **II**, a slightly smaller one in **III** and its absence in **I** (see above).

In a more general way, in one solution J has to be large enough compared to D so that the hole between the two halves of the Pake pattern is broad enough. This may vary from sample to sample since the observation of a hole in the Pake-like pattern requires also a good knowledge of the intermolecular background.

The analysis laid out here relies on the assumption that the electron-electron coupling is not much larger than the frequency difference between the detected and pumped spins, which is full-filled even for $\Delta\nu_{AB}$ = 40 MHz for all three molecules. If the couplings were much larger, the Pake pattern would not contain any information on J and $\nu_{\perp}$ would appear at 1.5 times D.[14]

Finally, the values obtained for r and J from reading-off the spectra were substituted as initial guesses into PESIM using the geometric models depicted in Figure 31. The flexibility yielded from the average bending, δ, of ±5° of the ring system mimics accessible non-planar structures of polycyclic aromatic hydrocarbons.[157] The influence of the consequential structural diversity might already be overestimated from a chemical point of view, and its influence on the simulated PELDOR time traces are indeed negligible compared to simulations neglecting any flexibility. However, different molecular structures with different orbital overlap are a requirement for a distribution in J for **II** and **III** and a distribution in J is needed to fit the modulation damping and to circumvent even larger bending angles.

These simulations yield the time traces in Figure 28 a, c, e and the data collected in Table 2, including the angle φ between A_{zz} and r for **I** and **II**, as well as distributions in r and J. The distributions are encoded in the modulation damping, the angle φ in the change of the orientation selection with $\Delta\nu_{AB}$, and J and r in the frequency of the modulation. The distribution in J, ΔJ, can be explained by the different molecular conformers, represented by the r-distribution, which will all give rise to slightly different orbital overlap. The values determined via the simulations are more precise than the ones determined from the Fourier Transformations, since it is easier to fit the simulation to a repetitive pattern than to read-off the frequencies from a peak or edge.

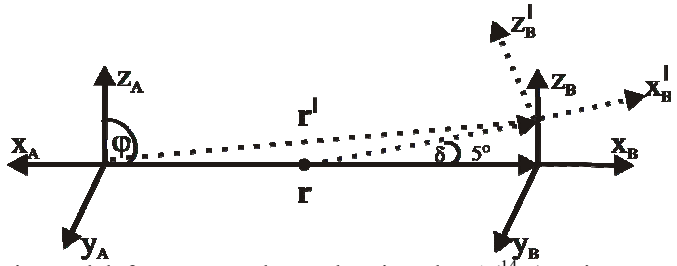

***Figure 31*:** Geometric model for **I**, **II** and **III** showing the A(^{14}N) axis system and the spin-spin distance vector and an average bending of the ring system in the *xz*-plane and around the center of the molecule of $\delta = \pm 5°$.

The error in *r* for **I** was deduced by a visual comparison of simulated PELDOR time traces with *r* = 26.8 and 27.0 Å, both leading to observable differences of the oscillation frequency as compared to the experiment. For **II** and **III**, the error in *r* was estimated from simulations varying *r* and *J* with a constant ΔJ in order to investigate a compensation of e.g. a large *r*-value with a decreased *J*-value. Small compensation effects were observed, but *r* and *J* can be independently yielded within the errors stated in Table 2. An analogous procedure was carried out for the analysis of the error of ΔJ, varying *J* and ΔJ at a constant *r*-value. The errors could be independently deduced. In contrast to Section 6.1 yielding insight towards the conformational flexibility of **1** and **2** the bending described by the angle δ for **I**, **II** and **III** is in such a small regime that it cannot be reliably gathered via PESIM.

6.4.4 Conclusions

Two new model systems that display exchange coupling constants on the order of the dipolar coupling were synthesized and their 4-pulse PELDOR spectra were recorded. The rigidity of the molecules leads to angular correlations which can partially be resolved at X-band and analyzed via the described simulation routine. In addition, the non-zero *J* yields two solutions for the *J*/*r*-couple and the correct one can be chosen based on simulations if the two pairs are different enough. For systems without conjugation in the interconnecting bridge this uncertainty is not critical, as the assumption of a negligible *J* is valid for the distance range accessible via PELDOR experiments. For molecule **II**, a ferromagnetic exchange coupling of *J* = -3.2 MHz was found, whereas an antiferromagnetic coupling of *J* = +2.5 MHz was determined for **III**. The change in the nature of the exchange coupling with respect to the substitution pattern may be rationalized by the exchange coupling pathways.

6.5 PELDOR "Spin Counting"

This chapter has been published in the *Journal of the American Chemical Society*, **129**, 6736, 2007. It is entitled. "Counting the Monomers in Nanometer-Sized Oligomers by PELDOR". The author contributed the synthesis of polyradical model compounds (see Section 2), extensive cw-EPR sample preparation of mixtures of radicals with a defined spin concentration and contributed to the simulations and data interpretation.

6.5.1 Abstract

In a lot of cases active biomolecules are complexes of higher order, thus methods capable of counting the number of building blocks and elucidating their geometric arrangement are needed. Here, PELDOR "Spin Counting" is experimentally validated on well-defined test samples. Two biradicals, a symmetric and an asymmetric triradical, and a tetraradical were synthesized in a convergent reaction scheme via palladium-catalyzed cross-coupling reactions. PELDOR was then used to obtain geometric information and the number of spin centers per molecule in a single experiment. The measurement yielded the expected distances (2.2 – 3.8 nm) and showed that different spin-spin-distances in one molecule can be resolved even if the difference amounts to only 5 Å. The number of spins *n* has been determined to be 2.1 in both biradicals, to 3.1 and 3.0 in the symmetric and asymmetric triradicals, respectively, and to 3.9 in the tetraradical. The overall error of PELDOR "Spin-Counting" was determined to be 5% for up to four spins. Thus, this method is a valuable tool to determine the number of constituting spin-bearing monomers in biologically relevant homo- and heterooligomers and how their oligomerization state and geometric arrangement changes during function.

6.5.2 PELDOR Distance Measurements

The PELDOR time traces of model systems **1** - **5** and the corresponding distances obtained from Tikhonov regularizations[143,144,158,159] are shown in Figure 32. The obtained distances agree well with the predicted ones and are summarized in Table 3.

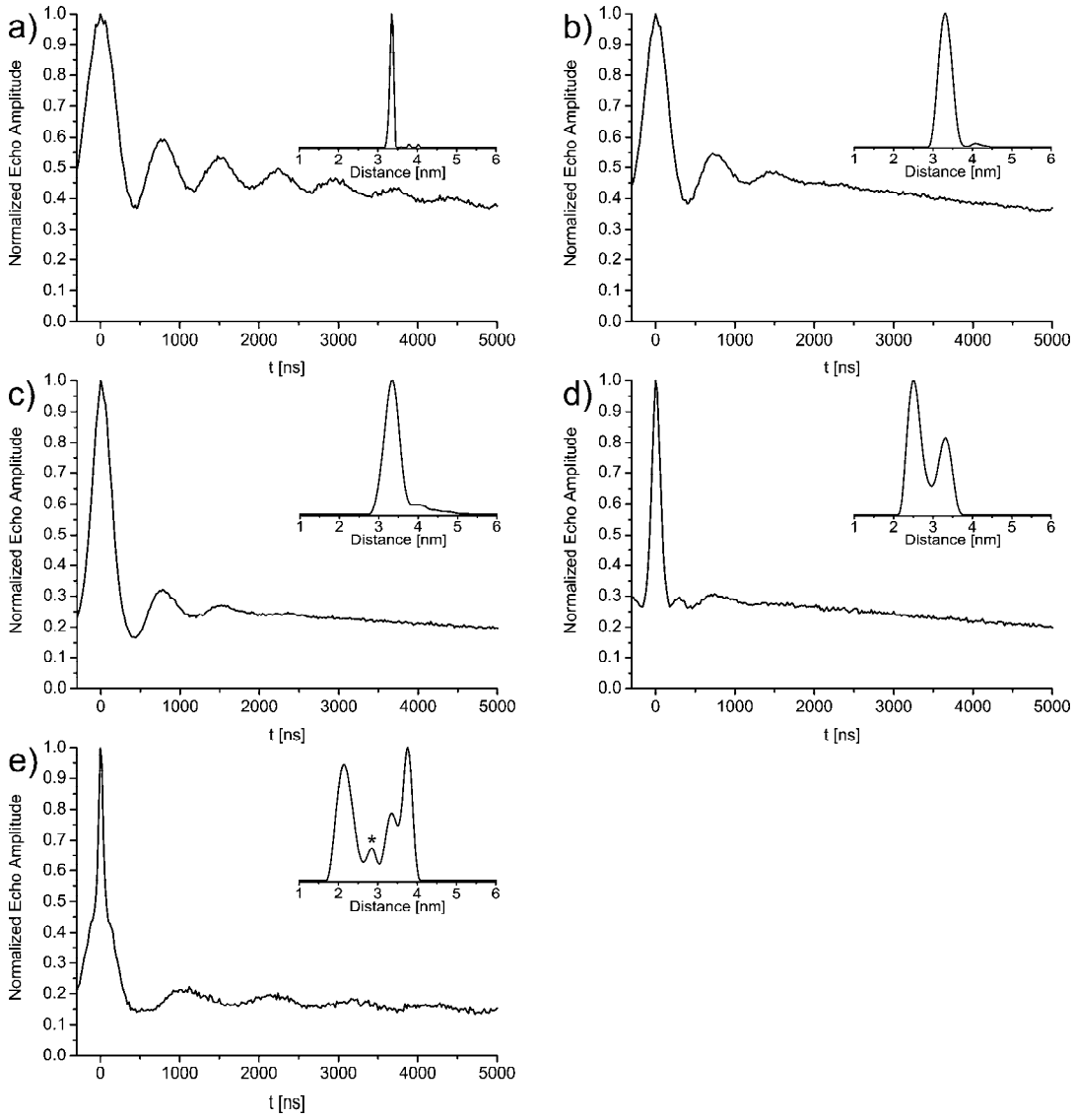

***Figure 32*:** PELDOR trace of model systems **1** - **5**; a) - e) respectively. Distance transformations from Tikhonov regularizations shown as inset. The peak marked with an asterisk in the distance domain of e) is an artifact from the regularization, that is not significant within the signal to noise ratio.

molecule [a]	r_{MM} [nm][b]	r_{exp} [nm][c]
1	3.4(0.1)	3.4(0.1)
2	3.4(0.4)	3.3(0.4)
3	3.4(0.4)	3.3(0.4)
4 [1,3/1,5]	2.5	2.5(0.4)
4 [3,5]	3.4	3.3(0.4)
5 [*ortho*]	2.0	2.2(0.5)
5 [*meta*]	3.4	3.3(0.4)
5 [*para*]	3.9	3.8(0.3)

[a]The numbers in square brackets give the positions at the benzene ring to which the nitroxide bearing moieties are linked to.
[b]The values are the distances between the centers of the N-O bonds. The number in brackets is the full width at half maximum of the structure ensembles used for simulations.
[c]The number in brackets is the full width at half maximum of the corresponding peak.

***Table 3*:** Distances *r* [nm] from modeling and Tikhonov regularization.

The linear biradical **1** (see Figure 32a) exhibits the largest number of visible oscillations leading to a narrow peak in the distance transformation. In contrast, the bent, *meta*-substituted molecules **2** and **3** (see Figure 32b, c) display faster damping of the oscillations, and consequently broader peaks in the distance domain. The different widths of the peaks in the distance domain can be qualitatively related to the molecular structure. In a linear, stretched structure as in **1**, the spin-spin distance can only be reduced by molecular bending motions. Whereas, in bent structures as in **2** and **3** bending motions can increase and decrease the end-to-end distance around the equilibrium structure. Furthermore, the same angular deviations lead to larger distance deviations in a bent structure than in a linear structure based on simple geometric considerations. Consequently, the asymmetric triradical **4** (see Figure 32d) shows peaks of approximately the same widths as for radicals **2** and **3** (see Figure 32b, c). The faster damping of the modulation of **4** (see Figure 32d) is due to the interfering dipolar frequencies. The approximately two-fold higher intensity of the peak at 2.5 nm in the distance domain of asymmetric triradical **4** (see Figure 32d) may also be rationalized by the molecular geometry, the shorter distance can be extracted two times, the longer distance only once. However, tetraradical **5** (see Figure 32e) does

not show this correlation. According to structural symmetry all three distances appear two times, but the intensities of the peaks differ. On the other hand the decreasing widths of the peaks at 2.2 (*ortho*), 3.4 (*meta*), and 3.8 (*para*) nm is in agreement with the above considerations about molecular structure and bending motions. Consequently, Tikhonov regularization nicely yields the mean distances, but a quantitative analysis of the distance distribution should be treated with care. The reason is that in current state-of-the-art software implementations the time domain data is only simulated as a sum of pairs and not as a sum of products of triples or quadruples. Therefore, cross-terms of higher order in λ_B arising from the simultaneous pumping of several B spins in tri- and tetraradicals are not properly treated.[143] Especially, in tetraradical **5** (see Figure 32 e) the probability of multiple, coherent B-spin flips is fairly high (~35 %), which might cause the observed regularization artifact and improper amplitudes in the distance distribution.

6.5.3 PELDOR "Spin Counting"

Molecules **1** – **6** were utilized to prove, that the number *n* of coupled nitroxides can be determined from the PELDOR time traces, using the analytical expressions derived for geometrically uncorrelated radical centers. Based on the considerations of Milov, Tsvetkov et al.,[33,46] the spectra in Figure 32 were corrected for the intermolecular contributions to the echo decay by division by a mono-exponential decay and normalized to $t = 0$ (see Figure 33).

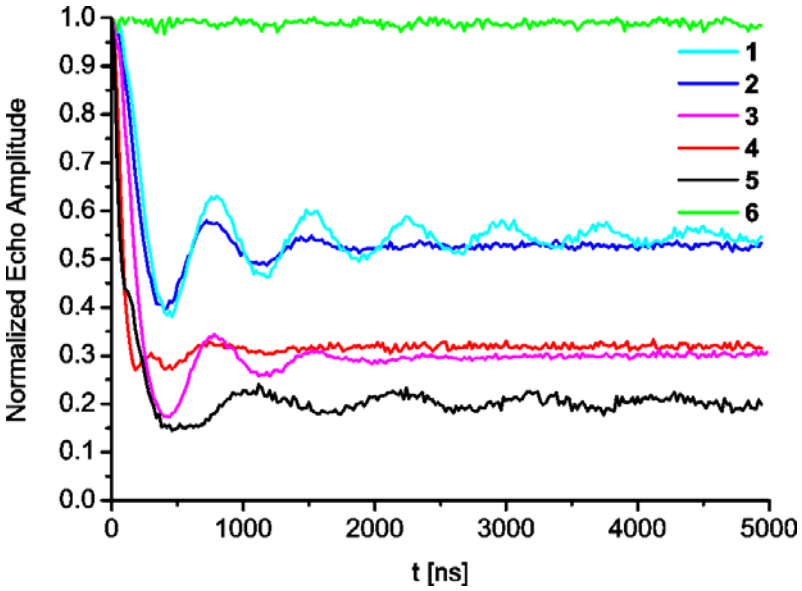

***Figure 33*:** Corrected time domain signals for determination of n in **1** – **6**. V_λ is read off as the echo amplitude at t = 5000 ns.

Figure 33 clearly demonstrates that the modulation depth increases from a mono- to a tetraradical. Reading off the modulation depth V_λ at the end of the respective time traces and substituting the value into eq. 48 allows direct determination of the number of spins *n*. The "Spin Counting" results are compared to the actual number of spins in the corresponding molecules in Table 4.

molecule	***n***	V_λ	n_{found}[a]
1	2	0.54	2.1(1)
2	2	0.53	2.1(1)
3	3	0.30	3.1(2)
4	3	0.32	3.0(2)
5	4	0.20	3.9(2)

[a]The number in brackets is the error in the last digit, determined from a ΔV_λ of 0.02.

Table 4: Number of spins *n* from processed time domain data.

Obviously, the experimental "Spin Counting" nicely reproduces the nominal number of spin centers in the model systems. The accuracy in *n* is determined by the error in the modulation depths V_λ. The observed experimental reproducibility of the individual V_λ-values is within 0.02 leading to an error in *n* of about 5%. Important for this accuracy is a high signal-to-noise ratio (here > 100:1) and a precise value for λ_B. In this study λ_B was calibrated with standard biradical **16**[44,91] (see Section 2). Phase

cycling of the π/2-pulse is mandatory to eliminate receiver offsets, because the applied deconvolution of intra- and intermolecular contributions to the echo decay implies that the experimental trace is zero at infinity. In addition, the measured number of spins was independent of the sample concentration and τ-modulation averaging. Under these conditions monomers, dimers, trimers and tetramers can be readily distinguished. Within these limits a pentamer can still be identified, but for $n > 5$ a strong decrease in accuracy is expected, since V_λ will come closer to zero, which lowers the signal-to-noise ratio and the differences in V_λ decrease with the potency of n. As mentioned earlier, V_λ is described as a product of the contributions of all coupled spins (eq. 47). Figure 34 shows the applicability of eq. 47. The cube root of tetraradical **5** and the square roots of triradicals **3** and **4** give within the error the same V_λ as biradicals **1** and **2**.

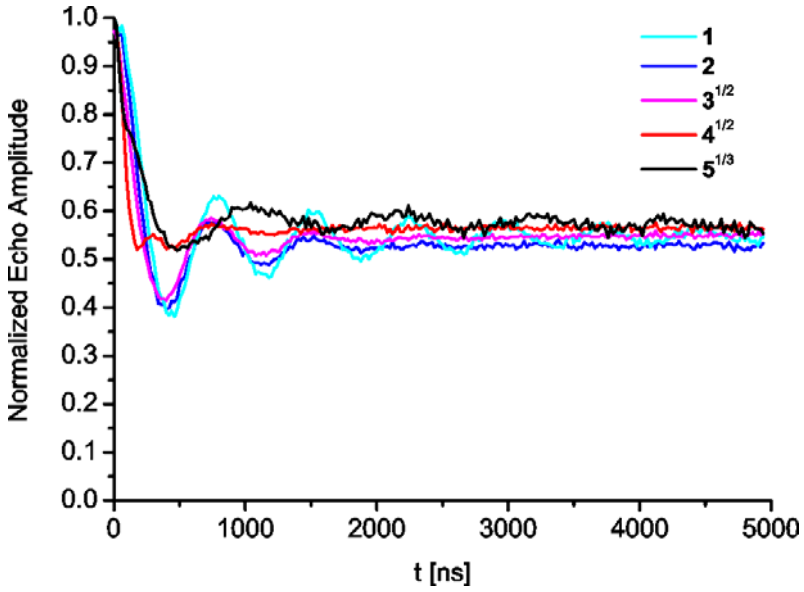

***Figure 34*:** Modulation depths can be described as factorized by the number of coupling spins.

In this work λ_B is approximated to be identical in radicals **1** - **6**, which will be valid if the orientations of the nitroxide labels within one molecule, and thus their respective hyperfine and *g*-tensor orientations, are not correlated with each other. If this assumption was not fulfilled, λ_B would depend on the relative orientation. To verify the assumption of negligible angular correlation, numerical simulations of the time domain signals of linear biradical **1** and bent triradical **3** exhibiting different geometries were performed using PESIM. Assuming some degree of backbone bending (±10°) and full rotational freedom about the acetylene linkers a set of 10,000

structures was generated (see Figure 10; Note that the bending in these preliminary simulations differs from the values derived in Section 6.1). The result depicted in Figure 35 shows that especially the modulation depth parameters λ_B of the experimental data are reproduced very well. Thus, estimating equal λ_B-values is feasible. However, weak angular correlations cannot be excluded, but they are not observed within the error of the experiment. Work by Jeschke et al.[28] on similar biradical model systems exhibited high flexibility and also weak correlations in label orientations. In biological systems spin labels are usually even more flexible than in this study, so their angular correlation will be even weaker. Thus, it is possible to count the number of monomers in samples of pure oligomeric states.

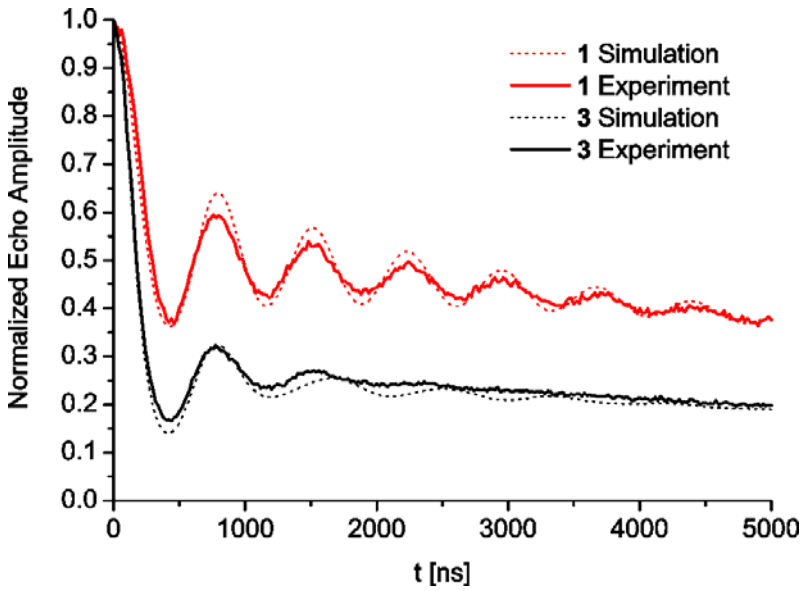

***Figure 35*:** Experimental PELDOR data and simulations for **1** and **3**.

6.5.4 Conclusion

It was shown on **1** - **5** that a single PELDOR data set yields not only distances, and thereby precise geometric information on the nanometer scale, but also the number of spins *n* in a molecule. The method has an overall error of ~5% in *n* for up to four spins, provided that the spin-labeling is complete and that the error of the excitation probability factor λ_B does not exceed 0.02, which can be readily achieved. In complexes with more than five spins or incomplete labeling or in presence of mixtures of oligomeric states this accuracy strongly decreases. Thus, PELDOR "Spin Counting" is a method by which the oligomeric state of biologically relevant complexes can be evaluated down to concentrations of ~50 µM at a volume of 80 µL, given that the monomers carry a spin center, and that the spin-spin distances are within the PELDOR limit (15 – 80 Å).

7. Conclusions and Outlook

This thesis demonstrates the advancement of PELDOR spectroscopy beyond its original design of distance measurements in order to disentangle a maximum amount of information additionally encoded in the PELDOR data. In particular, the successful synthesis of novel polynitroxide radicals is described as well as the extraction of the relative orientation of spin labels, conformational flexibility and the separation of dipolar and exchange coupling via orientation selective PELDOR measurements in combination with PESIM based simulations. Moreover, the method of PELDOR "Spin Counting" was experimentally validated.

7.1 Synthesis of Model Compounds

A convenient route to rigid, shape persistent polyradical systems, namely two biradicals, **1** and **2**, a symmetric, **3**, and an asymmetric triradical, **4**, and a tetraradical, **5**, has been established by means of Sonogashira couplings and a corresponding polar protective group strategy. Even though Sonogashira couplings involving 1,3-enynes such as the spin label employed in this thesis are lower in yield than those using non-conjugated terminal acetylenes the overall yields are comparable to other strategies discussed in literature. This route is easily extendable to a variety of iodo substituted arylic compounds. Nitroxides **1** – **5** were completely characterized, are chemically stable, bear well defined distances between the spin centers and mimic different geometries and aggregation states of biomolecules. Additionally, the crystal structures of **10** and **16** were solved.

7.2 Analysis of Orientation Selective PELDOR Data using Model Compounds

7.2.1 Analysis via PESIM

For **1** and **2** it was possible to show that the detection frequency offset dependency of the oscillation frequencies arises from orientation correlations between the nitroxides and the distance vector *r* even at 9 GHz. If the experiment is performed only with one fixed offset frequency and analyzed by assuming a random orientation distribution, a wrong *r* distribution could result. By a systematic variation of the detection frequency such effects can easily be detected and taken into account. Therefore, PELDOR time traces were recorded with different pump and detection frequencies (so called orientation selective PELDOR measurements) and a quantitative analysis of the frequency offset dependence with PESIM allowed to gather a detailed picture of the conformational distribution of **1** and **2**. It was described via a random orientation of the nitroxide *x*-axis (N-O) on a cone with an angle of 22° with respect to the linear acetylene linker. The nitroxide *z*-axis (out of plane) was assumed to be perpendicular to the linear linker, but otherwise also randomly oriented. The conformational flexibility of the interconnecting molecular bridge was modeled utilizing a simple bending motion, with a Gaussian half width angle $\delta\phi$ = 40° and 20° for **1** and **2**, respectively. The distances found for **1** and **2** are both 3.4 nm. The agreement between simulations and experiment is excellent.

7.2.2 Analysis via Tikhonov regularization

Employing Tikhonov regularization to PELDOR signals of **1** and **2** allowed obtaining both distance information and orientational information from the orientation selective experimental X-band PELDOR data. Adopting various polynomials as test orientation intensity functions, the internal consistency of this approach was proven, that is, recalculated and original PELDOR time traces are in good agreement. Furthermore, it was demonstrated that PELDOR signals, distance distributions, and orientational intensity functions gained from the experimental data of **1** and **2** as well as from MD simulations are in good agreement. The differences between the results yielded by both methods are surprisingly small. An analysis of the MD trajectories revealed that

the spin labels rotate freely around their connecting bond axes, the normal of the radical planes is on average perpendicular to the connecting dipolar vector, and the angle between the NO axis of the labels and the dipolar vector is on average ~ 140° for **1** whereas it is more or less uniformly distributed in the interval of 110° - 170° for the **2**.

7.3 Application of Orientation Selective PELDOR Measurements to DNA

It was shown that the parameter free extraction of distances and relative orientations of spin centers in twofold nitroxide labeled double helical DNAs (**DNA I**, **DNA II**) and an organic reference compound **I** can be achieved via orientation selective PELDOR spectroscopy at X-band frequencies in conjunction with PESIM. The angle between the *z*-component of the ^{14}N hyperfine coupling tensor and *r* was found to be 5 ± 15°, 45 ± 15°, 90 ± 10° and *r* equal to 3.8 ± 0.1 nm, 2.7 ± 0.1 nm and 2.6 ± 0.1 nm for **DNA I**, **DNA II** and **I**, respectively.

7.4 Disentangling Dipolar and Exchange Coupling

Two new conjugated aromatic model systems, **II** and **III**, displaying exchange coupling constants on the order of the dipolar coupling were subjected to PELDOR measurements. The rigidity of the molecules lead to angular correlations which were partially resolved at X-band frequency and analyzed via PESIM. In addition, the non-zero *J* yielded two solutions for the *J*/*r*-couple and the correct one was chosen based on PESIM simulations. This is possible, if the two *J*/*r* pairs are rather different. For systems without an extended conjugation in the interconnecting bridge this uncertainty is not critical, as the assumption of a negligible *J* is valid for the distance range accessible via PELDOR experiments. For molecule **II**, a ferromagnetic exchange coupling of J = -3.2 ± 0.6 MHz was found, whereas an antiferromagnetic coupling of J = +2.5 ± 0.5 MHz was determined for **III**. The damping of the oscillations is explained through a distribution in J, ΔJ, of ± 0.8 MHz and ± 1.7 MHz for **II** and **III**. Changes in the sign of J with respect to the substitution pattern may be rationalized by the different exchange coupling pathways.

7.5 PELDOR "Spin Counting"

PELDOR "Spin Counting" experiments on molecules **1** – **5** even at concentrations of approximately 50 µM at a volume of 80 µL demonstrate that not only distances**,** but also the number of spins *n* in a molecule are accessible with an error of ca. 5% in *n* for up to four spins. The measurement yielded the expected distances (2.2 – 3.8 nm) and showed that the different spin-spin-distances in **5** can be resolved even if the difference amounts to only 5 Å. Additionally*, n* has been determined to be 2.1 in **1** and **2**, to 3.1 and 3.0 in the **3** and **4**, respectively, and to 3.9 in **5**. Yet, it is required that the spin labeling is complete and that the error in λ_B is not larger than 0.02. In case of *n* exceeding five, incomplete labeling or in presence of mixed oligomeric states this accuracy decreases. Thus, PELDOR "Spin Counting" is a method by which the oligomeric state of biologically relevant complexes can be determined.

7.6 Outlook

In conclusion, this thesis clearly unraveled more than distance information from PELDOR data. Even at commercially available X-band EPR spectrometers conformational flexibility, the relative orientation of spin labels, exchange coupling and the number of spin bearing units are accessible performing orientation selective PELDOR measurements. Further calculations in order to deduce the conformational flexibility of biomolecules such as DNA employing a multi-frequency approach are extremely interesting and are currently in progress. First results regarding a radial "breathing motion" of double helical B-DNAs are to be published in due course and are sketched in Section 6.3.4. This section also briefly introduces a numerical approach to disentangle the angle between the *z*-component of the ^{14}N-hyperfine coupling tensor and the distance vector without *a priori* structural assumptions.

8. Appendix

8.1 Experimental Section

Samples with volumes of 100 µL and concentrations of 100 µM were prepared either as solutions in d_8-toulene or molten *ortho*-terphenyl for cw- and PELDOR measurements, respectively. cw-EPR samples were saturated with argon prior to use. The spin-labeled DNA duplexes 5´-d(GT**Ç**AGTGCGCGCGCGATC) 5´-d(GATCGCGCGCGCG**Ç**ACTGAC) (**DNA I**) and 5´-d(GT**Ç**AGTCGCGCGCGCATC) 5´-d(GATGCG**Ç**GCGCGCGACTGAC) (**DNA II**), were prepared by annealing the appropriate spin-labeled, single-stranded DNA oligomers (10 nmol each strand) in PNE buffer (100 µL, final conc. 100 µM of duplex). The water was evaporated in vacuo and the residue redissolved in 20% ethyleneglycol/H2O (100 µL, final conc. 100 µM of duplex). All samples were rapidly frozen in liquid nitrogen for low temperature measurements.

8.1.1 cw EPR

cw X-band EPR spectra were acquired on a Bruker ELEXSYS E500 cw X-band EPR spectrometer. The microwave frequency created with a Bruker microwave bridge ER041MR was measured by use of a Systron Donner (6054D) frequency counter. The magnetic field was measured with a Bruker gaussmeter (ER035M). All room temperature spectra were recorded using a standard rectangular Bruker EPR cavity (ER4102ST7934) at a quality factor *Q* of about 3000, with a sampling time of 40 ms, a microwave power of 1 mW and a modulation amplitude of 0.1 mT at a modulation frequency of 100 kHz.

8.1.2 PELDOR

All PELDOR spectra were recorded on a Bruker ELEXSYS E580 pulsed X-band EPR spectrometer with a standard flex line detection head housing a dielectric ring resonator (MD5 W1) equipped with a continuous flow helium cryostat (CF935) and temperature control system (ITC 502), both from Oxford instruments. The second microwave frequency was coupled into the microwave bridge by a commercially available setup (E580-400U) from Bruker. All pulses were amplified via a pulsed

travelling wave tube (TWT) amplifier (117X) from Applied Systems Engineering. The resonator was over-coupled to a quality factor Q of about 50. PELDOR experiments were performed with the pulse sequence $\pi/2(\nu_A)$-τ_1-$\pi(\nu_A)$-(τ_1+t)-$\pi(\nu_B)$-(τ_2-t)-$\pi(\nu_A)$-τ_2-echo. The detection pulses (ν_A) were set to 32 ns for both π and $\pi/2$ pulses and applied at a frequency 40 to 80 MHz higher than the resonance frequency of the resonator. The pulse amplitudes were chosen to optimize the refocused echo. The $\pi/2$-pulse was phase-cycled to eliminate receiver offsets. The pump pulse (ν_B) with a length of 12 ns was set at the resonance frequency of the resonator. The field was adjusted such that the pump pulse is applied to the maximum of the nitroxide spectrum, where it selects the central $m_I = 0$ transition of A_{zz} together with the $m_I = 0$, ±1 transitions of A_{xx} and A_{yy}. The pulse amplitude was optimized to maximize the inversion of a Hahn-echo at the pump frequency. All PELDOR spectra were recorded at 40 K with an experiment repetition time of 4.5 ms. Usually, a video amplifier bandwidth of 25 MHz and a video amplifier gain of 60 dB was used. The time window τ_1 was set to 136 ns, τ_2 to 2500 - 5000 ns and the time increment Δt for the dipolar evolution to 12 ns. In the case of **II**, the video bandwidth was increased to 50 MHz and the detection pulse length decreased to 16 ns. Furthermore, the time increment Δt was decreased to 4 ns and τ_2 was shortened to 1000 ns. In all cases proton modulation was suppressed by addition of 8 spectra of variable τ_1 with a $\Delta\tau_1$ of 8 ns. For comparison with simulations the time traces were divided by a mono-exponential decay and normalized to the point $t = 0$. Usually 1000 – 5000 scans were accumulated leading to approximate measuring times of 3 to 15 hours.

8.1.3 PELDOR Simulations

A typical conformational ensemble contains 1000 different structures each characterized via an interconnecting spin-spin distance vector r and polar angles in the axis system of spin A. Euler angles Ω were used to characterize the mutual orientation of spin centre B with respect to A. Hyperfine and g-tensor axes were considered to be collinear to the molecular axis system. For all orientations (typically 20000) of the magnetic field vector B_0 in the molecular axis frame of spin A, the resonance positions of spins A and B were calculated. Transforming the hyperfine and g-tensor of spin B in the coordinate system of spin A yields spin B resonance frequencies.

Final resonance frequencies of spin A and B were obtained taking a Gaussian distributed inhomogeneous line width into account. Pulse excitation profiles for detection and pump pulses were calculated based on the Bloch equations for uncoupled spins.[11] This gives rise to the excitation functions of spin A and B and the resulting dipolar distribution function for each conformer. The final PELDOR signal for a given frequency offset $\Delta\nu$ is the sum over all conformers and all magnetic field values. Full details of the simulation routine are described elsewhere.[104]

8.2 Constants

Avogadro number	$N_A = 6.022137 \cdot 10^{23}$	mol^{-1}
Bohr magneton	$\beta_e = 9.274015 \cdot 10^{-24}$	$A\ m^2$
Boltzmann constant	$k = 1.380568 \cdot 10^{-23}$	$J\ K^{-1}$
Electron rest mass	$m_e = 9.109390 \cdot 10^{-31}$	kg
Elementary charge	$e = 1.602177 \cdot 10^{-19}$	C
Free electron *g*-value	$g_e = 2.002319$	
Nuclear magneton	$\beta_I = 5.050787 \cdot 10^{-27}$	$A\ m^2$
Permeability of vacuum	$\mu_0 = 1.256637 \cdot 10^{-6}$	$V\ s\ A^{-1}\ m^{-1}$
Permittivity of vacuum	$\varepsilon_0 = 8.854188 \cdot 10^{-12}$	$A\ s\ V^{-1}\ m^{-1}$
Planck constant	$h = 6.626076 \cdot 10^{-34}$	J s
	$\hbar = 1.054589 \cdot 10^{-34}$	J s
Proton rest mass	$m_p = 1.672623 \cdot 10^{-27}$	kg
Speed of light in vacuum	$c = 2.997926 \cdot 10^{8}$	$m\ s^{-1}$

8.3 List of Figures

8.4. Curriculum Vitae

Klaus Dominik Margraf

Personal Data

Eduard-Bernstein-Weg 12
60439 Frankfurt am Main
069 74730660
0176 22776888
DominikMargraf@aol.com
born 12.06.1978 in Melle (German citizenship)

EDUCATION

Johann Wolfgang Goethe Universität
PhD Student in the Institute of Physical and Theoretical Chemistry **2009**
Beyond Distance Measurement - Advancing X-Band PELDOR spectroscopy
in the group of Prof. Dr. T. F. Prisner

Johann Wolfgang Goethe Universität
Academic degree of Diplom-Chemiker (grade: sehr gut) **2004**
Synthese und Charakterisierung von α-arylstabilisierten Vinylkationen
in the group of Prof. Dr. T. Müller

Johann Wolfgang Goethe Universität
Vordiplom in Chemistry (grade: sehr gut) **2000**

Gymnasium Melle
Allgemeine Hochschulreife **1997**

New Iberia Senior High School, LA/USA **1994 - 1995**

AWARDS

Travel grant of the German Chemical Society **2008**
Honorary Board Member of „Chemie in unserer Zeit" **2007**
Travel grant of the American Chemical Society **2007**
Travel grant of the German Chemical Society **2007**
Travel grant of the Friends and Supporters of the Young Chemical Society **2007**
PhD Scholarship of the Centre of Membrane Proteomics **2004**
Scholarship of the Louisiana State University **1995**

ACADEMIC TEACHERS

N. Auner, W. Aßmus, J. Bats, B. Brutschy, E. Egert, J. W. Engels, L. Fink, M. Göbel, C. Griesinger, S. Hashmi, K. Hensen, B. Kolbesen, E. Mohler, T. Müller, P. Pickel, T. F. Prisner, D. Rehm, E. A. Reinsch, H. Roskos, O. Schiemann, G. Stock, M. Wagner, V. Wittmann, E.-J. Zehnder

8.5 Deutsche Zusammenfassung

In dieser Arbeit wird die Weiterentwicklung der X-Band PELDOR-Spektroskopie über Abstandsmessungen hinaus, mit dem Ziel ein Maximum an zusätzlicher Information aus den erhaltenen PELDOR-Spektren zu gewinnen, beschrieben. Insbesondere wird die erfolgreiche Synthese neuartiger Polynitroxidradikale aufgezeigt sowie die Extraktion der relativen Orientierung von Spinsonden, die Bestimmung der konformationellen Flexibilität und die Trennung von dipolarer und Austauschwechselwirkung. Zusätzlich wird die Methode des PELDOR „Spinzählens" experimentell validiert.

8.5.1 Synthese von Modellverbindungen

Es wurde ein geeigneter synthetischer Zugang zu rigiden, formbeständigen Polyradikalsystemen gefunden. Zwei Biradikale, **1** und **2**, ein symmetrisches, **3**, und ein asymmetrisches Triradikal, **4**, und ein Tetraradikal, **5**, wurden mittels Sonogashirakupplungen und einer entsprechenden polaren Schutzgruppenstrategie dargestellt. Trotz der Tatsache, dass die Ausbeuten von Sonogashirakupplungen mit 1,3-Eninen wie dem verwendeten Spinmarker niedriger sind als für nicht konjugierte terminale Acetylene, ist die Gesamtausbeute der verfolgten Strategie mit anderen in der Literatur beschriebenen vergleichbar. Dieser Syntheseweg lässt sich leicht auf eine Vielzahl von iodsubstituierten aromatischen Verbindungen ausweiten. Nitroxide **1 - 5** sind chemisch stabil, besitzen definierte Abstände zwischen den Spinzentren und ahmen verschiedene Geometrien sowie Aggregationszustände von Biomolekülen nach. Darüber hinaus konnten die Kristallstrukturen von **10** und **16** gelöst werden.

8.5.2 Analyse der orientierungsselektiven PELDOR Daten an Modellverbindungen

8.5.2.1 Analyse mittels PESIM

An Verbindung **1** und **2** wurde gezeigt, dass selbst bei 9 GHz die Abhängigkeit der Osziallationsfrequenz von der Abfragefrequenzdifferenz in Bezug zur Anregefrequenz aus korrelierten Orientierungen zwischen Nitroxiden und dem Abstandsvektor *r* hervorgehen. Wird das Experiment mit nur einer festen

Abfragefrequenz durchgeführt und unter Annahme einer zufallsverteilten Orientierungsfunktion analysiert, könnten falsche Abstandsverteilungen resultieren. Durch eine systematische Variation der Abfragefrequenz sind solche Effekte leicht zu detektieren und können in die Datenanalyse einbezogen werden. Aufgrund dessen sind so genannte orientierungsselektive PELDOR Zeitdömanensignale mit verschiedenen Abfrage- und Anregefrequenzen aufgenommen worden. Eine quantitative Auswertung der erhaltenen Ergebnisse mittels PESIM ergab einen detaillierten Einblick in die Konformerenvielfalt von Molekül **1** und **2**. Diese wurde durch eine freie Rotation der Nitroxid *x*-Achse (N-O) um die Acetylenbindung auf einem Konus mit einem Öffnungswinkel von 22° beschrieben. Die Nitroxid *z*-Achse wurde hierbei als zufallsverteilt, aber dennoch senkrecht zum Acetylen angenommen. Die konformationelle Flexibilität des verbindenden Molekülgerüstes wurde durch einen einfachen gaussverteilten Biegungswinkel mit einer Halbwertsbreite $\delta\phi$ = 40° und 20° für **1** bzw. **2** modelliert. Die ermittelten Abstände für **1** und **2** betragen je 2.4 nm und die Übereinstimmung zwischen Experiment und Simulation ist hervorragend.

8.5.2.2 Analyse mittels Tikhonov Regularisierung

Eine Tikhonov Regularisierung der PELDOR Signale von **1** und **2** gestattete die direkte, modellfreie Ermittlung von Abstands- und Orientierungsverteilung aus dem orientierungsselektiven PELDOR Datensatz. Unter Vorgabe mehrerer Polynome als Orientierungsfunktion wurde die interne Konsistenz dieses numerischen Ansatzes überprüft: regularisierte und ursprüngliche PELDOR Zeitdomänensignale stimmen überein. Außerdem konnte gezeigt werden, dass die aus dem Experiment erhaltenen PELDOR Signale, Abstandsverteilungen und Orientierungsfunktion von **1** und **2** mit denen aus MD Rechnungen in Einklang stehen. Die Unterschiede, der aus beiden Methoden ermittelten Ergebnisse sind überraschend gering. Die Analyse der MD Trajektorien zeigte eine freie Rotation der Spinmarker um die verbindende Molekülachse und dass die Nitroxid *z*-Achse im Mittel senkrecht auf dem Abstandsvektor steht sowie einen mittleren Winkel zwischen der Nitroxid *x*-Achse und dem dipolaren Vektor von 140° für **1** und einem in einem Intervall von 110° - 170° fast gleichverteilten Winkel für **2**.

8.5.3 Orientierungsselektive PELDOR Messungen an DNS

An zwei doppelsträngigen, zweifach nitroxidmarkierten DNS (**DNS I** und **DNS II**) sowie einer organischen Referenzverbindung **I** wurde gezeigt, dass neben der parameterfreien Abstandsmessung auch die Bestimmung der relativen Orientierung der Spinsonden zueinander durch orientierungsselektive PELDOR Spektroskopie und anschließender PESIM Analyse möglich ist. Der Winkel zwischen der *z*-Komponente des ^{14}N-Hyperfeinkopplungstensors und *r* wurde als 5 ± 15°, 45 ± 15°, 90 ± 10° und *r* als 3.8 ± 0.1 nm, 2.7 ± 0.1 nm und 2.6 ± 0.1 nm für **DNS I**, **DNS II** und **I** ermittelt.

8.5.4 Trennung von dipolarer und Austauschwechselwirkung

Zwei neue, konjugierte aromatische Modellverbindungen, **II** und **III**, mit Austauschwechselwirkungen in der Größenordnung der dipolaren Kopplung wurden orientierungsselektiven PELDOR Messungen unterzogen. Die Steifigkeit von **II** und **III** führte zu im X-Band partiell aufgelösten Winkelkorrelationen, die mittels PESIM analysiert wurden. Zusätzlich führte ein von null verschiedenes *J* zu zwei möglichen Lösungen für das *J*/*r* Paar. Das korrekte kann unter der Vorraussetzung, dass die beiden *J*/*r* Paare sich stark voneinander unterscheiden durch PESIM bestimmt werden. Für Systeme ohne ausgedehnte Konjugation im verbindenden Molekülgerüst ist diese Bedingung als nicht kritisch zu bewerten, da die Annahme eines vernachlässigbaren *J* für den mit PELDOR messbaren Abstandsbereich weiterhin gültig ist. Für **II** wurde eine ferromagnetische Austauschwechselwirkung von J = -3.2 ± 0.6 MHz und für **III** eine antiferromagnetische Austauschwechselwirkung von J = +2.5 ± 0.5 MHz gefunden. Die Dämpfung der Oszillationen wird durch eine *J*-Verteilung, ΔJ, von ± 0.8 MHz und ± 1.7 MHz für **II** bzw. **III** erklärt. Die Unterschiede im Vorzeichen von *J* mit Hinblick auf das Substitutionsmuster lassen sich durch verschiedene Austauschwechselwirkungspfade rationalisieren.

8.5.5 PELDOR „Spinzählen“

PELDOR „Spinzähl“ Experimente an Molekülen **1** – **5** ergaben, dass selbst bei Konzentrationen von ca. 50 µM und einem Volumen von 80 µL nicht nur Abstände, sondern auch die Anzahl der Spinzentren, *n*, in einem Molekül ermittelbar sind. Der Fehler in *n* beträgt ungefähr 5% für bis zu vier Spins. Die Messungen zeigten die erwarteten Abstände (2.2 – 3.8 nm) und dass die verschiedenen Spin-Spin-Abstände in **5** selbst bei Unterschieden von lediglich 5 Å auflösbar sind. Außerdem wurde *n* zu 2.1 in **1** und **2**, zu 3.1 und 3.0 in **3** bzw. **4** und zu 3.9 in **5** bestimmt. Als Bedingung hierfür gilt eine vollständige Spinmarkierung und dass der Fehler in λ_B nicht größer als 0.02 ist. Für $n > 5$, unvollständiger Spinmarkierung oder einer Mischung von Oligomeren nimmt die Genauigkeit der Methode ab. Dessen ungeachtet ist das PELDOR „Spinzählen“ eine Methode, die den Oligomerisierungsgrad biologisch relevanter Systeme aufklären kann.

8.5.6 Ausblick

Abschließend zeigt diese Doktorarbeit deutlich, dass mehr als reine Abstandsinformation aus PELDOR Daten gewonnen werden kann. Selbst mit kommerziell erhältlichen X-Band ESR Spektrometern kann die relative Orientierung von Spinsonden, die konformationelle Flexibilität, die Austauschwechselwirkung sowie die Anzahl der Spinzentren bestimmt werden. Weitere Datenanalysen zur Untersuchung der Konformerenvielfalt von Biomolekülen wie DNS sind im höchsten Maße interessant und momentan in Arbeit. Erste Ergebnisse bezüglich einer radialen „Atmung“ doppelsträngiger B-DNS stehen kurz vor Veröffentlichung und sind in Kapitel 6.3.4 skizziert. Hier wird ebenfalls kurz ein numerischer Ansatz zur Berechnung des Winkels zwischen der *z*-Komponente des ^{14}N-Hyperfeinkopplungs-tensors und des Abstandsvektors ohne vorherige strukturelle Annahmen vorgestellt.

8.6 Acknowledgements

Firstly, I wish to express my gratitude to Prof. Dr. Thomas F. Prisner. He always encouraged me to work independently and supported my ideas and opinions even against exterior pressure. His in depth knowledge of EPR was always inspiring. I also took advantage of his laboratories and his PESIM simulation program which I used to simulate PELDOR spectra throughout my doctoral studies.

I am indebted to Dr. Olav Schiemann for introducing me to the experimental details of PELDOR spectroscopy and his guidance regarding my synthetic work. Without his assistance some publications would still remain manuscripts. His challenging style of questioning ideas and results lead to numerous unforgotten discussions far beyond the concepts of science.

I would like to thank Dr. Bela Ernest Bode not only for sharing an office, but also for answering questions about EPR, MATLAB® and Praktikum I never dared to ask anybody else. His comments and ideas greatly advanced my studies and sometimes even my personal life. His every now and then polarizing yet professional and honest style throughout many years made him a valuable friend.

If it had not been for my lab mate Dr. Jörn Plackmeyer many coupling steps and purifications would still be never ending stories. He completed the synthesis of the asymmetric triradical. His incredible understanding of chemistry and his great humor are priceless.

Prof. Dr. Snorri Th. Sigurdsson and Dr. Pavol Cekan, University of Iceland are acknowledged for providing samples of **DNA I** and **DNA II** as well as the organic reference compounds **I** – **III**.

Dr. Sevdalina Lyubenova introduced me to cw-EPR. She was always willing to help and I enjoyed many cigarettes and coffees with her. She also corrected this thesis.

Dr. Andriy Marko corrected the theoretical part of this thesis in every detail. His mathematical and physical knowledge are utmost fascinating. Without Dr. Burkhard Endeward who maintained the pulsed EPR spectrometer many experiments would never have been carried out and Dr. Vasyl Denysenkov recorded G-band data that will be presented in near future. Denise Schütz, B. Sc., is thanked for letting me know how supervisors feel. It was a marvelous experience to have a “Bachelorette”.

I also wish to thank all group members not mentioned before: Dr. Marina Bennati, Charlotte Börner, Adrian Cernescu, Reza Dastvan, Dr. Melanie Dornhaus (born

Hertel), Dr. Emiliano Feresin, Dr. Jörg Fritscher, Dr. Marat Gafurov, Dr. Stéphane Grimaldi, Sigrid Kämmerer, Bernhard Kinzer, Dr. Natalie Kisseleva, Jan Krummenacker, Ivan Krstic, Dr. Thorsten Maly, Dr. Fraser MacMillan, Hildegard Mathis, Astrid Noll, Dr. Marloes Penning de Vries, Volker Pfannebecker, Dr. Mark Prandolini, Dr. Deniz Sezer, Stephanie Steinbrenner, Kathrin Stroka and Bernhard Thiem for the splendid working atmosphere.
Financial support was provided by the Center of Membrane Proteomics, the Deutsche Forschungsgemeinschaft Sonderforschungsbereich 579 "RNA-Ligand Interactions" and the Center of Biomolecular Magnetic Resonance. Travel grants were generously given by the German Chemical Society, the American Chemical Society and the Friends and Supporters of the Young Chemical Society.

Thanks to Mirka Verhoefen the Praktikumsdienst was great fun. We had many discussions with respect to "Um die Ecke gedacht".

I wish to thank my "brother" Patrick T. Thibodeaux for teaching me that one does not need to complete college for a successful and blessed life. He helped to keep my feet on the ground.

My former longtime life companion Wiebke Galuba needs to be mentioned for putting up with a PhD student in chemistry. Even though things did not work out as originally planned we came a long way together.
I am indebted to Natalie Umierski, B. Sc., for her understanding and support when I needed it the most.

My parents, Ulrike Margraf and Andreas Busch constantly pointed out that also humanities do exist beside science and that there is more to read than scientific publications. Thanks to them I did not turn into to a complete nerd and big city freak.

Last, but not least I am extremely grateful to Dr. Franz Ralf Dornhaus, Dr. Thomas Theissmann and Dr. Deniz Akalay who helped to keep me on track. Whenever I needed counseling they provided whatever was necessary to relax. You are my homies!

8.7 Bibliography

[1] B. Loll, J. Kern, W. Saenger, A. Zouni, J. Biesiadaka *Nature*, **438***,* 1040, 2005.
[2] P. Cramer, D. A. Bushnell, R. D. Kornberg *Science,* **292***,* 1863*,* 2001.
[3] N. Ban, P. Nissen, J. Hansen, P. B. Moore, T. A. Seitz *Science*, **289**, 905, 2000.
[4] J. A. Nelson, O. C. Uhlenbeck *Molecular Cell,* **23***,* 447*,* 2006.
[5] A. M. J. J. Bonvin, R. Boelens, R. Kaptein *Cur. Opin. Chem. Biol.*, **9**, 783, 2005.
[6] R. R. Ernst *Angew. Chem*., **104**, 817, 1992.
[7] K. Wüthrich, *NMR of Protein and Nucleic Acids*, John Wiley and Sons, New York, 1986.
[8] D. D. Laws, H.-M. L. Bitter, and A. Jerschow, *Angew. Chem.*, **41**, 3096, 2002.
[9] J. R. Lakowicz, *Principles of Fluorescence Spectroscopy*, 3rd Edn., Springer: New York, 2006.
[10] A. J. Hoff, *Advanced EPR. Applications in Biology and Biochemistry*, Elsevier: Amsterdam, 1989.
[11] A. Schweiger, G. Jeschke, *Principles of Pulse Electron Paramagnetic Resonance*, Oxford University Press: Oxford, 2001.
[12] O. Schiemann, T. F. Prisner, *Quart. Rev. Biophys.*, **40**, 1, 2007.
[13] K. Möbius, A. Savitsky, *High-Field EPR Spectroscopy on Proteins and their Model Systems*, RSC Publishing: London, 2008.
[14] G. Jeschke. *Macromol. Rapid Commun.*, **23**, 227, 2002.
[15] P. P. Borbat, H. S. Mchaourab, J. H. Freed, J. H. *J. Am. Chem. Soc.*, **124**, 5304, 2002.
[16] P. P. Borbat, J. H. Davis, S. E. Butcher, J. H. Freed, *J. Am. Chem. Soc.*, **126**, 7746, 2004.
[17] B. G. Dzikovski, P. P Borbat, J. H. Freed, *Biophys. J.* **2004**, *87*, 3504.
[18] K. Sale, J.-L. Faulton, G. A. Gray, J. S. Schoeinger, M. M. Young, *Protein Science*, **13**, 2613, 2004.
[19] N. Barhate, P. Cekan, A. P. Massey, S. Th. Sigurdsson, *Angew. Chem.,* **119**, 2709, 2007.
[20] C. Altenbach, T. Marti, H. G. Khorana, W. L. Hubell, *Science*, **248**, 1088, 1990.
[21] L. J. Berliner, *Biological Magnetic Resonance, Vol. 14*, Plenum Press: New York and London, 1998.
[22] L. J. Berliner, *Molecular Biology*, Academic Press: New York, 1976.
[23] K. Möbius, A. Savitsky, A. Schnegg, M. Plato, *Phys. Chem. Chem. Phys.*, **7**, 19, 2005.
[24] M. Bennati, T. F. Prisner, *Rep. Prog. Phys.*, **68**, 411, 2005.
[25] T. F. Prisner, M. Rohrer, F. MacMillan, *Ann. Rev. Phys. Chem.,* **52**, 279, 2001.
[26] C. Calle, A. Sreekanth, M. V. Fedin, J. Forrer, I. Garcia-Rubio, I. A. Gromov, D. Hinderberger, B. Kasumaj, P. Léger, B. Mancosu, G. Mitrikas, M. G.Satangelo, S. Stoll, A. Schweiger, Helv. Chim. Acta, **89**, 2495, 2006
[27] A. D. Milov, K. M. Salikhov, M. D. Shirov, *Fiz. Tverd. Tela*, 23, 975, 1981.
[28] A. Godt, M. Schulte, H. Zimmermann, G. Jeschke, *Angew. Chem. Int. Ed.*, **45**, 7560, 2006.
[29] G. Jeschke, A. Bender, H. Paulsen, H. Zimmermann, A. Godt, *J. Magn. Reson.*, **169**, 1, 2004.
[30] P. P. Borbat, J. H. Freed, *Biological Magnetic Resonance*, *Vol. 19*, Kluwer: New York, 2000.
[31] Y. D. Tsvetkov, A. D. Milov, A. G. Maryasov, *Russ. Chem. Rev.,* **77**, 487, 2008.

[32] G. Jeschke, *ChemPhysChem*, **3**, 927, 2002.
[33] A. D. Milov, A. G. Maryasov, Y. D. Tsvetkov, *Appl. Magn. Reson.*, **15**, 107, 1998.
[34] G. Jeschke, Y. Polyhach, *Phys. Chem. Chem. Phys*., **9**, 1895,2007.
[35] O. Schiemann, A. Weber, T. E. Edwards, T. F. Prisner, S. Th. Sigurdsson, *J. Am. Chem. Soc.*, **125**, 3434, 2003.
[36] Z. Zhou, S. C. DeSensi, R. A. Stein, S. Brandon, M. Dixit, E. J. McArdle, E. M. Warren, H. K. Kroh, L. Song, C. E. Cobb, E. J. Hustedt, A. E. Beth, *Biochemistry*, **44**, 15115, 2005
[37] M. Bennati, J. H. Robblee, V. Mugnaini, J. Stubbe, J. H. Freed, P. Borbat, *J. Am. Chem. Soc.*, **127**, 15014, 2005.
[38] C. W. M. Kay, C. Elsässer, R. Bittl, S. R. Farell, C. Thorpe, *J. Am. Chem. Soc.*, **128**, 76, 2006
[39] C. Elsässer, M. Brecht, R. Bittl, *J. Am. Chem. Soc.*, **124**, 12606, 2002.
[40] H. Hara, A. Kawamori, A. V. Astashkin, T.-A. Ono, *Biochim. Biophys. Acta* , **1276**, 140, 1996.
[41] T. Gullion, J. Schaefer, *J. Magn. Reson.*, **81**, 196, 1989.
[42] R. G. Larsen, D. J. Singel. *J. Chem. Phys.,* **98**, 5134, 1993.
[43] V. P. Denysenkov, T. F. Prisner, J. Stubbe, M. Bennati, *Proc. Natl. Acad. Sci. U.S.A.*, **103**, 13386 ,2006.
[44] A. Weber, O. Schiemann, B. E. Bode, T. F. Prisner., *J. Magn. Reson.*, **157**, 277, 2002.
[45] Y. Polyhach, A. Godt, C. Bauer, G. Jeschke, *J. Magn. Reson.*, **185**, 118**,** 2007.
[46] A. D. Milov, A. B. Ponomarev, Y. D. Tsvetkov. *Chem. Phys. Lett.*, **110**, 67, 1984.
[47] A. D. Milov, Y. D. Tsvetkov, F. Formaggio, M. Crisma, C. Toniolo, J. Raap, *J. Am. Chem. Soc.* **2000**, *122*, 3843.
[48] D. Hilger, Y. Polyhach, E. Padan, H. Jung, G. Jeschke, *Biophys. J.*, **93**, 3675, 2007.
[49] A.G. Maryasov, Y. D. Tsvetkov, J. Raap, *Appl. Magn. Reson.*, **14**, 101, 1998.
[50] B. E. Bode, J. Plackmeyer, T. F. Prisner and O. Schiemann, *J. Phys. Chem. A*, **112**, 5064, 2008.
[51] B. E. Bode, J. Plackmeyer, M. Bolte, T. F. Prisner and O. Schiemann, *J. Organomet. Chem.*, **694**, 1172, 2009.
[52] B. E. Bode, D. Margraf, J. Plackmeyer, G. Dürner, T. F. Prisner, O. Schiemann, *J. Am .Chem. Soc*., **129**, 6736, 2007.
[53] O. Schiemann, N. Piton, J. Plackmeyer, B. E. Bode, T. F. Prisner, J. W. Engels, *Nat. Protoc.*, **2**, 904, 2007.
[54] O. Schiemann, N. Piton, Y. Mu, G. Stock, J. W. Engels, T. F. Prisner, *J. Am. Chem. Soc.*, **126**, 5722,2004
[55] A. Spaltenstein, B. H. Robinson, P. B. Hopkins, *J. Am. Chem. Soc.*, **110**, 1299, 1998.
[56] N. Piton, O. Schiemann, Y. Mu, G. Stock, T. F. Prisner, J. W. Engels, *Nucleos. Nucleot. Nucl.*, **24**, 771, 2005.
[57] H. Pauly, *Justus Liebigs Ann. Chem.*, **322**, 77, 1902.
[58] E. G. Rozantsev, *Free Nitroxyl Radicals*; H. Ulrich, Ed.; Plenum Press: New York, 1970.
[59] T. Kálai, M. Balog, J. Jekö, K. Hideg, *Synthesis*, 973, 1999.
[60] M. A. Schwartz, J. W. Parce, H. M. McConnell, *J. Am. Chem. Soc.*, **101**, 3592, 1979.
[61] W. Brackmann, C. J. Gaazbeek, *Rec. Trav. Chim.*, **85**, 221, 1966.

[62] H. Ito, K. Arimoto, H.-O. Senusui, A.Rosomi, *Tetrahedron Lett.*, **38**, 3977, 1997.
[63] K. D. Ley, Y. Li, J. V. Johnson, D. H. Powell, K. Schanze, *Chem. Commun*., 1749, 1999.
[64] N. A. Bumagin, A. B. Ponomaryov, I. P. Beletskaya, *Synthesis*, 728, 1984.
[65] H. Kukula, S. Veit, A. Godt, *Eur. J. Org. Chem*., 277, 1999.
[66] S. I. Khan, M. W. Grinstaff, *J. Am. Chem. Soc.*, **121**, 4704, 1999.
[67] S. Takahashi, Y. Kuroyama, K. Sonogashira, N. Hagihara, *Synthesis*, 627, 1980.
[68] T. Kálai, M. Balog, J. Jekö, W. L. Hubbell, K. Hideg, *Synthesis*, 2365, 2002.
[69] J. J. Kirchner, E. J. Hustedt, B. H. Robinson, P. B. Hopkins, *Tetrahedron Lett.*, **31**, 593, 1990.
[70] F. M. Romero, R. Ziessel,*Tetrahedron Lett.*, **40**, 1895, 1999.
[71] K. Sonogashira, *Handbook of organopalladium chemistry for organic synthesis*; *E.* Nigishi, A. de Meijere, Eds.; Wiley: New York, Vol. 1, 2002.
[72] M. W. Miller, C. R. Johnson, *J. Org. Chem.*, **62***,* 1582, 1997.
[73] J. Fritscher, M. Beyer, O. Schiemann, *Chem. Phys. Lett.*, **364**, 393, 2002.
[74] S. J. Harris, D. R. M. Walton, *Tetrahedron*, **34**, 1037, 1978.
[75] S. J. Havens, P. M. Mergenrother, *J. Org. Chem.*, **50**, 1763, 1985.
[76] C. S. Swindell, W. Fan, P. G. Klimko, *Tetrahedron Lett.*, **35**, 4959, 1994.
[77] J. G. Rodriquez, R. Martin-Villamil, F. H. Cano, I. Fonesca, *J. Chem. Soc., Perkin Trans. I* , 709,1997.
[78] K. D. Ley, Y. Li, J. V. Johnson, D. H. Powell, K. Schanze, *Chem. Commun*., 1749, 1999.
[79] D. Margraf, J. W. Bats, *Acta Cryst.*, **E62**, 502, 2006.
[80] U. Schöberl, T. F. Magnera, R. M. Harrison, F. Fleischer, J. L. Pflug, P. F. H. Schwab, X. Meng, D. Lipiak, B. C. Noll, V. S. Allured, T. Rudalevige, S. Lee, J. Michl, *J. Am. Chem. Soc.*, **119**, 3907, 1997.
[81] D. L. Mattern, *J. Org. Chem*., **49**, 3051, 1984.
[82] C. S. Jones, M. J. O´Connor, M. M. Haley, *Acetylene Chemistry*; F. Diederich, P. J. Stang, R. R. Tykwinski, Eds.; Wiley: Weinberg, 2005..
[83] T. X. Neenan, G. M. Whitesides, *J. Org. Chem.*, **53**, 2489, 1988.
[84] B. C. Berris, G. H. Hovakeemian, Y.-H. Lai, H. Mestdagh, K. P. C. Vollhardt, *J. Am. Chem. Soc.*, **107**, 5670, 1985.
[85] A. Godt, C. Franzen, C. S. Veit, V. Enkelmann, M. Pannier, G. Jeschke, *J. Org. Chem.*, **65**, 7575, 2000.
[86] A. P . Davies, A. ; Morrison, M. D. Barratt, M. *Org. Mass. Spectrom.*, **8**, 43, 1974.
[87] H. M. Swartz, *J. Org. Chem.*, **54**, 3667, 1989.
[88] H. J. Milledge, L. M. Pant, *Acta Cryst.*, **13**, 285, 1960.
[89] R. K. R. Jetti, A. Nangia, F. Xue, T. C. W. Mak, *Chem. Commun.,* **10**, 919, 2001.
[90] H. D. Flack, *Acta Cryst.*, **A39**, 876, 1983.
[91] D. Margraf, D. Schütz, T. F. Prisner, J. W. Bats, *Acta Cryst.*, E65, o1784, 2009.
[92] D. Papoutsakis, J. P. Kirby, J. E. Jackson, D.G. Nocera, *Chem. Europ. J.*, **5**, 1474, 1999.
[93] J. C. A. Boeyens, G. J. Kruger, *Acta Cryst.*, **B26**, 668, 1970.
[94] M. Bolte, *Acta Cryst.*, **E62**, m1609, 2006.
[95] D. W. Wiley, J. C. Calabrese, R. L. Harlow, J. S. Miller, *Angew. Chem. Int. Ed.*, 30, 450, 1991.
[96] D. W. Wiley, J. C. Calabrese, J. S: Miller, *Chem. Commun.*, 1523, 1989.
[97] J. C. P. Poole, *Electron Spin Resonance*, Wiley: New York, 1967.

[98] K. Scheffler, H. B. Stegmann, *Elektronenspinresonanz, Grundlagen und Anwendungen in der organischen Chemie*, Springer: Berlin, 1970.
[99] J. A. Weil, J. R. Bolton, J. E. Wertz, *Electron Paramagnetic Resonance: Elementary Theory and Practical Applications*, Wiley: New York, 1994.
[100] O. Stern, W. Gerlach, *Zeitschrift f. Physik*, **8**, 100, 1921.
[101] O. Stern, W. Gerlach, *Zeitschrift f. Physik*, **9**, 349, 1922.
[102] M. H. L. Pryce, *Proc. Phys. Soc. (Lond.),* **A63**, 25, 1950.
[103] A. Abragam, M. H. L. Pryce, *Proc. Roy. Soc. (Lond.)*, **A205**, 135, 1951.
[104] D. Margraf, B. E. Bode, A. Marko, O. Schiemann, T. F. Prisner, *Mol. Phys*., **105**, 2153, 2007.
[105] C. P. Slichter, *Principles of Magnetic Resonance*, Berlin: Springer Verlag, 1980.
[106] P. J. Hore, *Nuclear Magnetic Resonance*, Oxford: Oxford Chemistry Primers, 1995.
[107] Valid in case the distance between the electrons is much larger than their spatial distribution.
[108] K. Yoshizawa, R. Hoffmann, *J. Am. Chem. Soc*., **117**, 6921, 1995.
[109] R. Hoffmann, W. N. J. Lipscomb, *J. Chem. Phys.*, **36**, 2179, 1962.
[110] A. Rajca, *Chem. Rev.*, **94**, 871, 1994.
[111] R. E. Martin, M. Pannier, F. Diederich, V. Gramlich, M. Hubrich, H. W. Spieß, *Angew. Chem. Int. Ed.,* **37,** 2833, 1998.
[112] M. Pannier, S. Veit, A. Godt, G. Jeschke, H. W. Spieß, *J. Magn. Reson.,* **142**, 331, 2000.
[113] R. MacKinnon, *Angew. Chem. Int. Ed.*, **43**, 4265, 2004.
[114] E. Gouaux, R. MacKinnon, *Science*, **310**, 1461, 2005.
[115] D. Langosch, L. Thomas, H. Betz, *Proc. Natl. Acad. Sci.*, **85**, 7394, 1988.
[116] T. Páli, M. E. Finbow, A. Holzenburg, J. B. C. Findlay, D. Marsh, *Biochemistry*, **34**, 9211, 1995.
[117] H. Iwamoto, D. M. Czajkowsky, T. L. Cover, G. Szabo, Z. Shao, *FEBS Lett.*, **450**, 101, 1999.
[118] D. M. Czajkowsky, H. Iwamoto, T. Coverdagger, Z. Shao, *Proc. Natl. Acad. Sci.* U.S.A., **96**, 2001, 1999.
[119] A. O. O'Reilly, B. A. Wallace, *J. Peptide Sci.*, **9**, 769, 2003.
[120] I. G. Janausch, I. Garcia-Moreno, G. Unden, *J. Biol. Chem.*, *277*, 39809, 2002.
[121] H. Schägger, *Biochim. Biophys. Acta*, **1555**, 154, 2002.
[122] A. Stroh, O. Anderka, K. Pfeiffer, T. Yagi, M. Finel, B. Ludwig, H. Schägger, *J. Biol. Chem.*, **279**, 5000, 2004.
[123] C. L. Will, R. Lührmann, *RNA World*; 3rd ed.; R. F. Gesteland, T. R. Cech, J. F. Atkins, Eds.; Cold Spring Harbor: New York, 2006.
[124] P. Dube, F. Herzog, C. Gieffers, B. Sander, D. Riedel, S. A. Müller, A. Engel, J.-M. Peters, H. Stark, *Mol. Cell*, **20**, 867, 2005.
[125] A. A. Rostom, C. V. Robinson, *Curr. Opin. Struct. Biol.*, **9**, 135, 1999.
[126] J. M. Daniel, S. D. Friess, S. Rajagopalan, S. Wendt, R. Zenobi, *Int. J. Mass Spectrom.*, **216**, 1, 2002.
[127] K. G. Heinze, M. Jahnz, P. Schwille, *Biophys. J.*, **86**, 506, 2004.
[128] C. F. W. Becker, R. Seidel, M. Jahnz, K. Bacia, T. Niederhausen, K. Alexandrov, P. Schwille, R. S. Goody, M. Engelhard, *ChemBioChem*, **7**, 891, 2006.
[129] J. Liu, Y. Lu, *J. Am. Chem. Soc.*, **124**, 15208, 2002.
[130] H. M. Watrob, C.-P. Pan, M. D. Barkley, *J. Am. Chem. Soc.*, **125**, 7336, 2003.

[131] N. Nag, G. Krishnamoorthy, B. J. Rao, *FEBS J.*, **272**, 6228, 2005.
[132] J. Chugh, A. Chatterjee, A. Kumar, R. K. Mishra, R. Mittal, R. V. Hosur, *FEBS J.*, **273**, 388, 2006.
[133] J. Cramer, J. Jaeger, T. Restle, *Biochemistry*, **45**, 3610, 2006.
[134] V. V. Krishnan, *J. Magn. Reson.*, **124**, 468, 1997.
[135] W. Luo, M. J. Hong, *J. Am. Chem. Soc.* **2006**, *128*, 7242.
[136] K. E. Vostrikova, *Cood. Chem. Rev.*, 252, 1409, 2008,
[137] D. M. Low, G. Rajaraman, M. Helliwell, G. Timko, J. van Slageren, R. Sessoli, S. T. Ochsenbein, R. Bircher, C. Dobe, O. Waldmann, H.-U. Güdel, M. A. Adams, E. Ruiz, S. Alvarez, E. J. L. McInnes, *Chem. Eur. J.*, **12**, 1385, 2006
[138] S. J. Blundel, *Contemp. Phys.*, **48**, 275, 2007.
[139] C. Elschenbroich, M. Wolf, O. Schiemann, K. Harms, O. Burghaus, J. Pebler, *Organometallics*, **21**, 5810, 2002.
[140] C. Elschenbroich, O. Schiemann, O. Burghaus, K. Harms, *Chem. Commun.*, 2149, 2005.
[141] B. L. Farmer, B. R. Chapman, D. S. Dudis, W.W. Adams, *Polymer*, **34**, 1588, 1993.
[142] A. Marko, D. Margraf, H. Yu, Y. Mu, G. Stock, T. F. Prisner, *J. Chem. Phys.*, **130**, 064102, 2009, DOI:10.1063/1.3073040.
[143] G. Jeschke, A. Koch, U. Jonas, A. Godt, *J. Magn. Reson.*, **155**, 72, 2002.
[144] The program used for data inversion was obtained from: http://www.mpip-mainz.mpg.de/~jeschke/distance.html.
[145] Y.-W. Chiang, P. P. Borbat, J. H. Freed, *J. Magn. Reson.*, **172**, 279, 2005.
[146] Y.-W. Chiang, P. P. Borbat, J. H. Freed, *J. Magn. Reson.*, **177**, 184, 2005.
[147] O. Schiemann, P. Cekan, D. Margraf, T. F. Prisner, S. Th. Sigurdsson, *Angewandte Chemie,* **121**, 3342, 2009.
[148] E. J. Hustedt, A. Smirnov, C. F. Laub, C. E. Cobb, A. H. Beth, *Biophys. J.*, **72**, 1861, 1997.
[149] A. Savitsky, A. A. Dubinskii, M. Flores, W. Lubitz, K. Möbius, *J. Phys. Chem. B*, 111, 6245, 2007.
[150] P. Cekan, A. L. Smith, N. Barhate, B. H. Robinson, S. Th. Sigurdsson, *Nucleic Acids Res.*, **36,** 5946, 2008
[151] G. Jeschke, V. Chechik, P. Ionita, A. Godt, H. Zimmermann, J. Banham, C. R. Timmel, D. Hilger, H. Jung, *Appl. Mag. Reson.*, **30**, 473, 2006.
[152] S. B. Smith, Y. Cui, C. Bustamante, *Science,* **271**, 795, 1996.
[153] P. Cluzel, A. Lebrun, C. Heller, R. Lavery, J.-L. Viovy, D. Chatenay, F. Caron, *Science*, **271**, 792, 1996.
[154] J. Gore, Z. Bryant, M. Nöllmann, M. U. Le, N. R. Cozzarelli, C. Bustamante, Nature, **442**, 836, 2006.
[155] R. Mathew-Fenn, R. Das, P. Harbury, *Science* **322**, 446, 2008.
[156] D. Margraf, P. Cekan, T. F. Prisner, S. Th. Sigurdsson, O. Schiemann, *Phys. Chem. Chem. Phys*, DOI:10.1039/ B905524J, 2009.
[157] S. Pogodin, I. Agranat, *J. Org. Chem.*, **67**, 265, 2002.
[158] Y.-W. Chiang, P. P. Borbat, J. H. Freed, *J. Magn. Reson.*, **172**, 279, 2005.
[159] http://www.mpip-mainz.mpg.de/~jeschke/distance.html